Full-Waveform Inversion for Breast Ultrasound

Taskin, U.

DOI
10.4233/uuid:a8c89eb8-b60f-4904-8425-f38fcb956a15

Publication date
2021

Document Version
Final published version

Citation (APA)
Taskin, U. (2021). *Full-Waveform Inversion for Breast Ultrasound*. [Dissertation (TU Delft), Delft University of Technology]. https://doi.org/10.4233/uuid:a8c89eb8-b60f-4904-8425-f38fcb956a15

FULL-WAVEFORM INVERSION FOR BREAST ULTRASOUND

Full-Waveform Inversion for Breast Ultrasound

Proefschrift

ter verkrijging van de graad van doctor
aan de Technische Universiteit Delft,
op gezag van de Rector Magnificus Prof.dr.ir. T.H.J.J. van der Hagen,
voorzitter van het College voor Promoties,
in het openbaar te verdedigen op
maandag 26 april 2021 om 10:00 uur

door

Ulaş TAŞKIN

Master of Science in Telecommunication Engineering
Istanbul Technical University, Turkije
geboren te Elazig, Turkije.

Dit proefschrift is goedgekeurd door de promotoren.

Samenstelling promotiecommissie bestaat uit:

Rector magnificus,	voorzitter
Prof.dr.ir. N. de Jong	Technische Universiteit Delft, promotor
Dr.ir. D.J. Verschuur	Technische Universiteit Delft, promotor
Dr. K.W.A. van Dongen	Technische Universiteit Delft, copromotor
Onafhankelijke leden:	
Prof.dr.ir. C.P.A. Wapenaar	Technische Universiteit Delft
Prof.dr. H.P. Urbach	Technische Universiteit Delft
Prof.dr. S. Manohar	University of Twente
Dr. Ö. Özdemir	Istanbul Technical University

The work in this dissertation was conducted at the department Imaging Physics, Faculty of Applied Sciences, Delft University of Technology.

Printed by: : Ridderprint | www.ridderprint.nl

ISBN 978-94-6384-211-2

An electronic version of this dissertation is available at
http://repository.tudelft.nl/.

Yaşamak bir agaç gibi tek ve hür
ve bir orman gibi kardeşçesine,

To live like a tree alone and free
and like a forest in brotherhood,

Nazım Hikmet Ran

CONTENTS

SUMMARY

Breast cancer is the most common type of cancer for women and in developed countries it forms one of their largest threats. Many studies have shown that early detection by screening is important for achieving a successful treatment and reducing the mortality rate. Nowadays mammography is the gold standard for breast cancer screening. However, mammography has several drawbacks including the use of ionizing radiation, a painful procedure, and poor performance with dense breasts. Magnetic resonance imaging (MRI) could form an alternative as it has some powerful features. However, the high examination and equipment costs as well as the use of contrast agents limits its applicability. Another potential alternative for breast cancer screening is ultrasound. Ultrasound has the advantage over mammography or MRI that it is safe, cheap and patient-friendly. With ultrasound, a tumor can be detected since healthy breast tissues and cancerous tissues have different acoustic properties. All these features make ultrasound a promising candidate as a screening modality for breast cancer.

Hand-held ultrasound scans are frequently used for breast imaging in hospitals. With these scanners reflectivity images are generated. These images typically show the boundaries between different tissues. Even when these exams are conducted by trained radiologists operator-dependency occurs. To eliminate this, automated full-breast ultrasound scanners have been developed where the transducer slides over the breast. However, as the imaging principle remains the same, only reflectivity images are generated. To avoid significant breast deformation as well as to scan the breast from as many sides as possible water-bath scanning systems have been developed. These systems have the additional advantage that both reflection and transmission measurements are obtained. This mixture of different measurement types make it feasible to obtain better images by employing advanced processing techniques.

One promising imaging method is full-waveform inversion (FWI). FWI aims to match a modeled wavefield to a measured wavefield by adjusting the acoustic medium parameters. A minimization problem is constructed and solved to this aim. As a result, images showing quantitative information about the different tissues are obtained. This quantitative information aids to the characterization and identification of the different tissues. However, there are some challenges when applying FWI. One of the biggest challenges is its computational complexity. By the inclusion of wave phenomena such as diffraction, refraction, scattering and dispersion - needed to explain the measured data in great detail - the computational complexity of FWI has become significantly larger than conventional - mainly ray based - imaging methods.

In this work, we investigate the applicability of contrast source inversion (CSI) as an FWI method for breast ultrasound. To this end, we first introduce our full-waveform forward modeling method which is based on solving an integral equation. With a synthetic example, we investigate how each medium parameter (compressibility, density, and attenuation) affects the scattered pressure field. The obtained results show that attenuation, in contrast to compressibility and density, has only little effect on the wavefield for frequencies below 1 MHz. From that we conclude, that for these frequencies only attenuation can be neglected in our inversion. We also compare the results from our full-waveform modeling method with results obtained after commonly made approximations such as Born, ray-based and paraxial approximations. We observe from the presented numerical results that with each approximation important phenomena normally present in the full-wave data are absent. For this reason, we recommend to use a full-wave modeling method to compute synthetic measurement data.

Next, we analyze a commonly faced problem with CSI, which is that the phase of the signal can shift more than half wavelength due to the contrast. This is referred to as cycle-skipping and usually occurs when high-frequency components of the measured data are used for the inversion. We show with a synthetic example that by using a frequency-hopping technique the cycle-skipping problem with CSI can be overcome.

Furthermore, we propose a redatuming method that is suitable for a water-bath scanning system. With redatuming, we backpropagate the measured pressure field closer to the target to make the computational domain smaller and consequently reduce the computation time for FWI. For our measurement setup, the total computation time with FWI is reduced by a factor four by using redatuming. Moreover, redatuming brings other advantages. In particular, redatuming may be used to remove part of the noise in the data or to compensate for a misalignment of the receivers with respect to the computational grid.

Finally, we investigate the applicability of multi-parameter inversion for breast ultrasound. To this end, we compute the particle velocity field from pressure field measurements with the aid of our presented redatuming method. Using both the pressure field and the particle velocity field leads to accurate multi-parameter inversion. Those accurate multi-parameter inversion results improve the characterization and identification of the various breast tissues. We show with a synthetic example that single-parameter inversion can fail due to leakage between different acoustic medium parameters. Multi-parameter inversion helps to avoid that problem.

In conclusion, the presented novel signal processing techniques will lead to an improved breast cancer detection using ultrasound.

SAMENVATTING

Borstkanker is de meest voorkomende vorm van kanker bij vrouwen, en vormt voor vrouwen in ontwikkelde landen een van de grootste bedreigingen. Meerdere onderzoeken hebben aangetoond dat vroegtijdige diagnose door middel van screening belangrijk is voor het succesvol behandelen van borstkanker en om de kans op overleving te vergroten. Vandaag de dag is mammografie de gouden standaard als het gaat om borstkankerscreening. Mammografie heeft echter meerdere nadelen, zoals het gebruik van ioniserende straling, een pijnlijke procedure en onbetrouwbare resultaten bij borsten met een hoge dichtheid. Magnetic resonance imaging (MRI) kan een alternatief vormen vanwege een aantal veelbelovende eigenschappen. Toch is de toepasbaarheid van MRI gelimiteerd vanwege de hoge kosten van de onderzoeken en de scanners, en het gebruik van contrastmiddelen. Een mogelijk ander alternatief voor de borstkankerscreening is echografie. Echografie heeft het voordeel ten opzichte van mammografie dat het veilig, goedkoop en patiëntvriendelijk is. Met echografie kan een tumor worden ontdekt door gebruik te maken van het verschil in akoestische eigenschappen tussen de tumor en het gezonde borstweefsel. Dit maakt echografie een veelbelovende alternatieve screening modaliteit voor borstkanker.

In ziekenhuizen wordt vaak echoapparatuur gebruikt waarbij de borst handmatig wordt gescand. Met deze systemen worden reflectiviteitsafbeeldingen gegenereerd. Deze afbeeldingen laten doorgaans de grenzen tussen de verschillende type weefsels zien. Zelfs als deze scans worden uitgevoerd door getrainde radiologen, is er sprake van afhankelijkheid van de onderzoeker die de apparatuur bedient. Om dit te elimineren is echoapparatuur ontwikkeld die de hele borst kan scannen door de transducer geautomatiseerd over de borst te bewegen. Echter, de beeldvormende techniek is nog steeds hetzelfde waarbij alleen de reflectiviteit wordt afgebeeld. Om aanzienlijke borstvervormingen te voorkomen en om de borst van zoveel mogelijk kanten te scannen, zijn waterbadscanners ontwikkeld. Deze systemen hebben als voordeel dat zowel reflectie- als transmissiemetingen kunnen worden gedaan. De combinatie van deze verschillende metingen maakt het mogelijk om betere afbeeldingen te maken door gebruik te maken van geavanceerde beeldvormende technieken.

Een veelbelovende beeldvormende techniek is 'full-waveform inversion' (FWI) ofwel volledige golfinversie. Het doel van FWI is om een gemodelleerd golfveld te matchen aan een gemeten golfveld door aanpassing van de akoestische medium parameters. Om dit te kunnen doen wordt een minimalisatie probleem geformuleerd en opgelost. Dit resulteert in de vorming van beelden met kwantitatieve informatie over de verschillende weefsels. Deze kwantitatieve informatie helpt bij het karakteriseren en identificeren van de verschillende type weefsels. Er zijn echter verschillende uitdagingen bij het toepassen van FWI. Een van de grootste uitdagingen is de complexiteit van de berekening. Door het meenemen van golfverschijnselen als buiging, breking, verstrooiing en dispersie (nodig om het gemodelleerde veld tot in detail te kunnen matchen aan de gemeten data), is de numerieke complexiteit van FWI aanzienlijk groter dan bij conventionele beeldvormende technieken.

In deze studie onderzoeken we de toepasbaarheid van 'contrast source inversion' (CSI) ofwel contrastbron inversie als een FWI methode voor borstechografie. Hiertoe introduceren we eerst onze voorwaartse full-waveform modelleringsmethode, welke is gebaseerd op het oplossen van een integraalvergelijking. Met een synthetisch voorbeeld onderzoeken we hoe elke medium parameter (compressibiliteit, dichtheid en verzwakking) het verstrooide drukveld beïnvloedt. De verkregen resultaten laten zien dat verzwakking, in tegenstelling tot compressibiliteit en dichtheid, maar een klein effect heeft op het golfveld voor frequenties lager dan 1 MHz. Daaruit concluderen we dat we alleen de verzwakking kunnen verwaarlozen bij inversie met deze lage frequenties. Daarnaast hebben we de resultaten van onze full-waveform modelleringsmethode vergeleken met resultaten verkregen via de veelvoorkomende Born, ray-based en paraxiale benaderingen. We zien dat in de gepresenteerde numerieke resultaten bij elke benadering belangrijke verschijnselen in de data ontbreken die wel aanwezig zijn in de full-wave data. Daarom bevelen we het gebruik van een full-wave methode aan om synthetische meetdata te genereren.

Vervolgens analyseren we een veelvoorkomend probleem bij CSI, namelijk dat de fase van het signaal meer dan halve golflengte kan verdraaien als gevolg van het contrast. Dit zogenaamde cycle-skipping komt meestal voor wanneer hoogfrequente componenten van de gemeten data worden gebruikt voor de inversie. Met een synthetisch voorbeeld laten we zien dat het gebruik van een frequency-hopping techniek het cycle-skipping probleem in CSI verhelpt.

Daarnaast stellen we een redatuming methode voor die geschikt is voor een waterbad scansysteem. Door het gebruik van redatuming back-propageren we ons gemeten drukveld dichter bij de bron zodat het computationele domein kleiner wordt. Hierdoor reduceren we de rekentijd voor FWI. Voor onze meetopstelling heeft het gebruik van redatuming de totale rekentijd van FWI gereduceerd met een factor vier. Redatuming heeft nog meer voordelen, in het bijzonder dat het kan worden gebruikt om een deel van de ruis in de data te verwijderen, en om te compenseren voor een verkeerde uitlijning van de ontvangers ten opzichte van het computationele raster.

Ten slotte onderzoeken we de toepasbaarheid van multiparameter inversie voor borstechografie. Daartoe berekenen we een deeltjessnelheidsveld van drukveldmetingen met behulp van de gepresenteerde redatuming methode. Gebruik van het drukveld in combinatie met het deeltjessnelheidsveld leidt tot een accurate multiparameter inversie. De accurate multiparameter inversie resultaten verbeteren het karakteriseren en identificeren van de verschillende borstweefsels. Met een synthetisch voorbeeld laten we zien dat single-parameter inversie kan falen door interferentie tussen verschillende akoestische medium parameters. Multiparameter inversie helpt in het voorkomen van dat probleem.

Dit proefschrift laat zien dat onze nieuwe signaal verwerkingstechnieken bijdragen aan een verbetering van borstkankerdetectie op basis van ultrageluid.

1

Introduction

1.1. Overview of breast imaging

Cancer is currently one of the largest threats for human life. It was the second leading cause of death after hearth disease in the United States in 2017, where 21.3 % of the deaths were caused by cancer. Moreover, between the age of 45 and 64 cancer is the leading cause of death [1]. Breast cancer in particular is one of the largest threats for women worldwide. For European women in the range 30-49, it was the main cause of death in 2016 [2], see Fig. 1.1. In addition, breast cancer has the highest incidence (24.2 %) and mortality (15 %) rates among all other types of cancer for women [3]. In the Netherlands, each year around 14000 women are diagnosed with breast cancer and 3000 women die because of breast cancer. To reduce the mortality rate, a national breast screening programme has been introduced to screen women between 50 and 75 years old once every two year. [4].

Recent data indicates that the mortality rate due to breast cancer shows a decreasing trend in well-developed countries [6]. This is mainly due to early detection and improved treatment [7]. Fig. 1.2 shows the ten year survival rate by stage of diagnosis. For early stage diagnosis, the cancer is only localized and the survival rate after ten years is 95 %. Unfortunately, after the cancer is already spread, the survival rate decreases to 74 % and 13 % for advanced and metastatic stages, respectively [8].

The stage of the cancer depends amongst others on the tumor size (T), and whether or not the cancer has spread to lymph nodes (N) or to the other organs (M). Table 1.1 shows TNM classification of breast tumors from the Union for International Cancer Control (UICC) [9]. Here, the TNM classification is combined with a stage I to IV characterization, where stage I and II refer to an early stage, III advanced stage and IV metastatic stage.

To reduce the mortality rate by early detection, various breast cancer screening systems are being developed. X-ray mammography, magnetic resonance imaging (MRI), and ultrasound are the three most common scanning systems that are used for breast cancer detection. These systems are not only helpful for early detection but also used during the treatment.

1

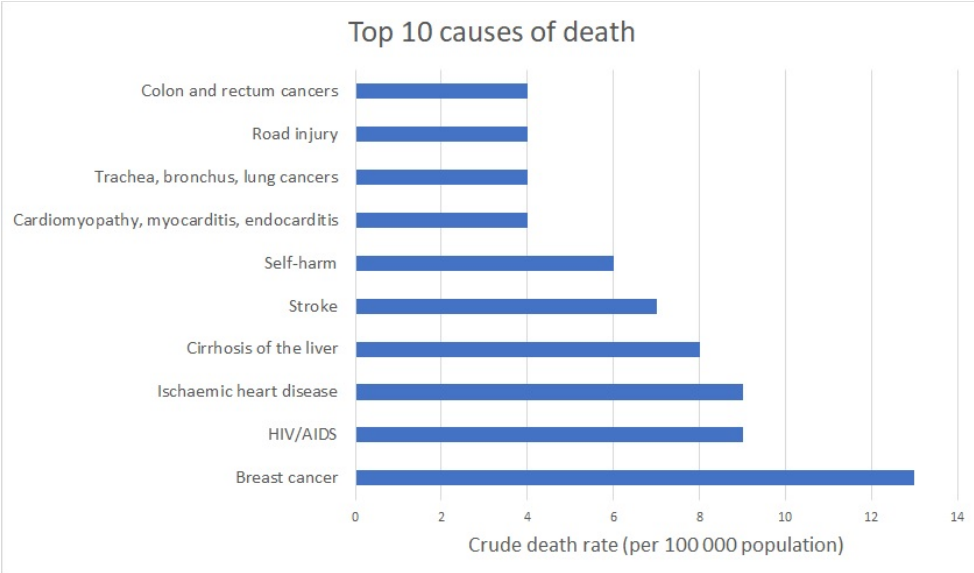

Figure 1.1: Top 10 causes of death for women between ages 30 and 49 in Europe in 2016 [5].

1.1.1. X-RAY MAMMOGRAPHY

Mammography is the primary screening modality for breast cancer. Research shows that routine screening with mammogram helps to detect breast cancer at an early stage. This early detection leads to a decrease in mortality rate by 30 % [10]. However, mammography is not the ideal screening modality. Its main drawback is its low sensitivity with dense breasts. This is especially a problem as 74 % of the women at their 40s have dense breasts [11]. For women with extremely dense breasts, the sensitivity of mammography decreases to 30 % [12]. In addition, breast density is an independent risk factor which means that women with dense breasts have more probability to get breast cancer as compared to women with fatty breast [13]. Other well-known drawbacks of mammography are that the exams are painful for women, and the radiation may be harmful.

1.1.2. MRI

MRI is one of the alternative screening modalities for breast cancer detection. MRI has a sensitivity of more than 90 % and has a similar specificity as mammography. MRI is mainly used in addition to mammography for women with a high risk for breast cancer [10]. Despite its accuracy in screening, MRI is less preferrable than mammography because of practical reasons. According to a survey under 1215 patients, 42 % refused to have an MRI scan. The top three reasons for not having an MRI scan is claustrophobia, time constraints and financial constraints [14].

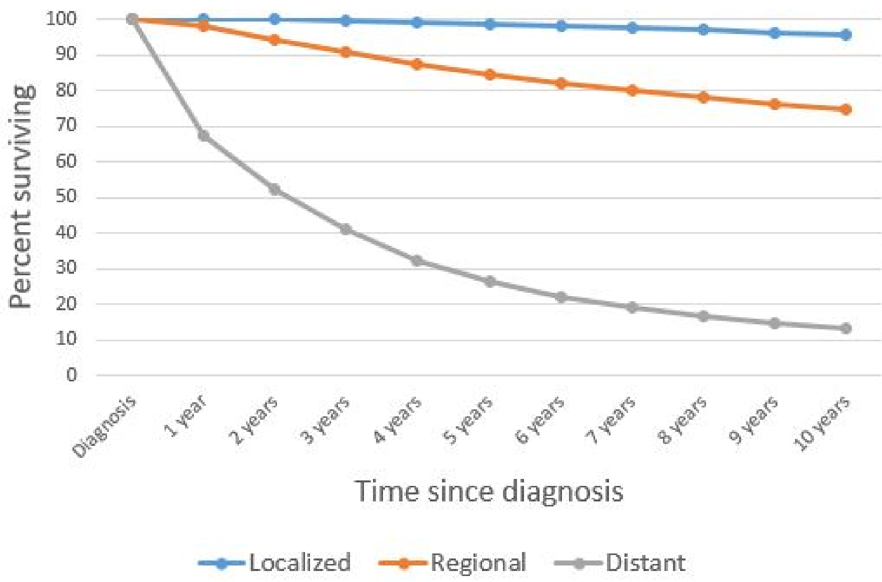

Figure 1.2: Ten year survival rate by stage of diagnosis [8].

1.1.3. ULTRASOUND

Ultrasound is a promising alternative for breast cancer detection. Ultrasound has the potential to overcome many of the problems encountered with mammography. First of all, the acoustic properties of a breast tumor deviates significantly from the surrounding healthy dense breast tissue. That's why, with ultrasound it is possible to detect a tumour in a dense breast. In addition, ultrasound is cheap, safe and patient-friendly [10], [15].

1.2. SCANNING METHODOLOGIES FOR BREAST ULTRASOUND

The potential of ultrasound for breast cancer screening has resulted in a large amount of research projects. In this section, three scanning methodologies are presented briefly.

1.2.1. HANDHELD SCANNING

Handheld ultrasound scanners are the most common scanning modalities for breast ultrasound. These scanners are frequently used supplementary to mammography. With a conventional handheld ultrasound scanner, a reflectivity image is generated using a delay-and-sum based beamforming method. An example of an image obtained with a handheld ultrasound scanner is shown in Fig. 1.3. Unfortunately, the resulting images are highly operator-dependent and have a low reproduciblity.

1.2.2. AUTOMATED FULL-BREAST SCANNING

Automated full-breast scanners are developed to overcome some of the problems faced with handheld scanners. These scanners are less operator-dependent and have a high image reproducibility. The imaging principle is similar to handheld scanners. They have

Table 1.1: Staging breast tumours according to the TNM classification [9].

Primary tumour (T)	Regional lymph node status (L)	Distant metastasis (M)	Stage
Tis	N0	M0	**0**
T1	N0	M0	**I**
T0	N1	M0	
T1	N1	M0	**II A**
T2	N0	M0	
T2	N1	M0	**II B**
T3	N0	M0	
T0	N2	M0	**III A**
T1	N2	M0	
T2	N2	M0	
T3	N1/N2	M0	
T4	Any N	M0	**III C**
Any T	N3	M0	**III C**
Any T	Any N	M1	**IV**

T-Tumour
T1 Tumour <2 cm
T2 2 cm <Tumour <5 cm
T3 Tumour >5 cm
T4 Tumour of any size with direct extension to chest wall or skin
N-Nymph node
N0 No cancer in regional node
N1 Regional movable metastasis
N2 Non-movable regional metastases
N3 Cancer in the internal mammary nymph nodes
M-Metastasis
M0 No distant metasteses
M1 Distant metasteses

the advantage over handheld systems that they can generate a three-dimensional (3-D) volumetric image of a part of the breast within a single scan. Typical images obtained with automated full-breast scanners are shown in Fig. 1.3.

1.2.3. WATER-BATH SCANNING SYSTEMS

Currently, there is an increasing interest in water-bath scanning systems. The first water-bath scanning systems were developed in the late 70s and early 80s [17]–[22]. With these first scanners, speed-of-sound and attenuation profiles of the breast were acquired by using basic tomographic reconstruction methods. The initial in-vivo images obtained with these early systems were quite promising. However, due to the limited resources on the hardware available at that time, research on the water-bath scanners did not continue. Thanks to the recent developments on both the acoustic hardware and general computer technology, research on water-bath scanners has revived. An example of a water-bath scanner is shown in Fig. 1.4 [23]. Images obtained from an in-vivo scan using this setup as well as an MRI image of the same breast are given in Fig. 1.5 [24].

Most water-bath scanners are made for breast imaging [25]–[27]. The breast has the advantages that it contains only soft tissue that can easily be probed using acoustic waves as well as that it can be probed from all sides. These properties make it possible to get through-transmission measurements in addition to reflection measurements. Recent advances in breast imaging with water-bath scanners resulted in attempts to use the same principles and scanners to image other organs such as brains [28] and bones [29].

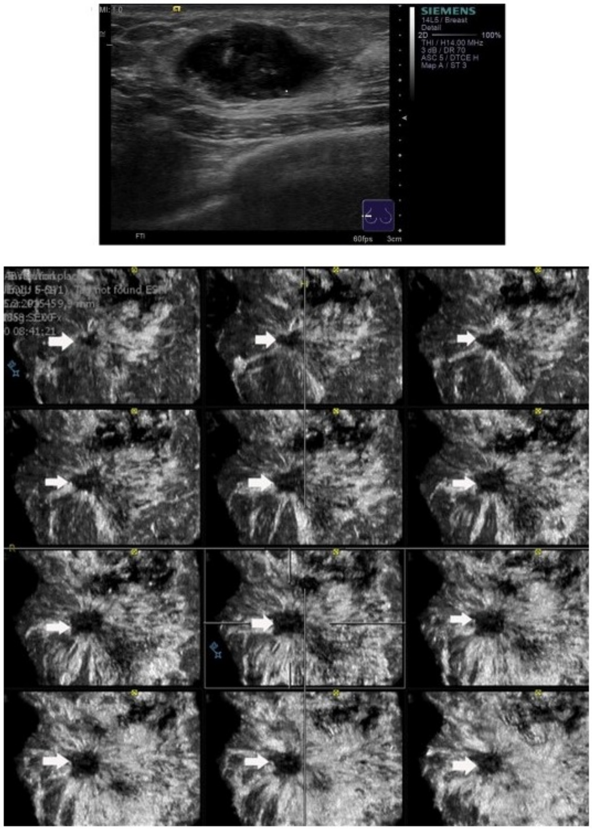

Figure 1.3: Ultrasound scans of a cancerous breast: handheld B-mode ultrasound (top), automated full-breast scanner images of an invasive ductal carcinoma of the breast in a multislice viewfrom (the slices are 0.5 mm) (bottom) [16].

1.3. IMAGING AND INVERSION METHODS

In this section, a summary of imaging and inversion methods used with water-bath scanners is given.

1.3.1. REFLECTIVITY IMAGING

Synthetic aperture focusing technique (SAFT) is used as a reflectivity imaging method in most water-bath scanning systems [30], [31]. It is a delay-and-sum (DAS) based algorithm. The main advantages of SAFT are that it is a fast and robust imaging method. Unfortunately, with SAFT only structural information about the breast is obtained. In addition, it is difficult to reconstruct speed-of-sound profiles by using only reflection measurements. Transmission measurements are needed to reconstruct accurate speed-of-sound profiles. A detailed analysis of reflection and transmission measurements are given in Appendix B.

1

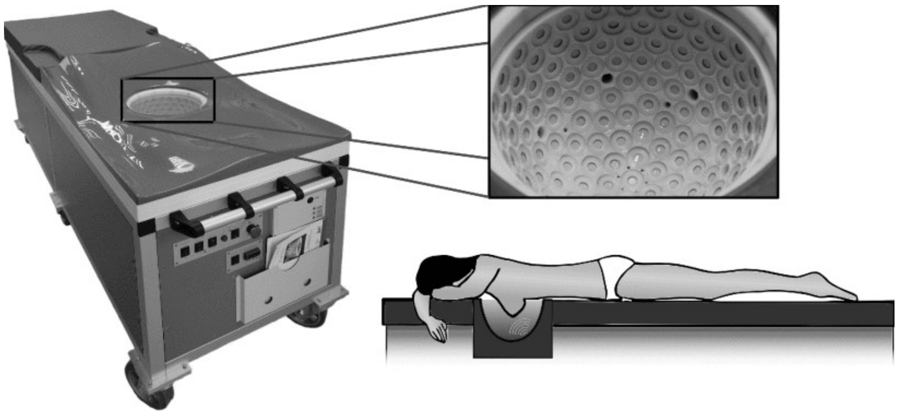

Figure 1.4: KIT 3D USCT with patient bed (left), transducer aperture (top right) and patient position (bottom right) [23].

1.3.2. RAY-BASED TOMOGRAPHIC RECONSTRUCTION

The through-transmission measurements can be processed using tomographic reconstruction algorithms similar to the ones used for CT scans. In general, these algorithms are derived within the ray approximation. A frequently used algorithm that is computationally efficient is filtered backprojection [32]. Others use methods based on linear system solvers such as algebraic reconstruction technique (ART). Some advanced methods also account for refraction [33], [34].

1.3.3. WAVE-BASED TOMOGRAPHIC RECONSTRUCTION AND FULL-WAVEFORM INVERSION (FWI)

Wave-based tomographic reconstruction methods can be divided into two main groups. The first group includes methods that use the first-order Born or Rytov approximation to linearize the non-linear inverse problem. Due to the applied linearization, they are computationally efficient. However, these methods are less suitable for breast imaging as the breast represents a relatively large acoustic contrast that limits the applicability of the Born approximation. The second group of methods are reffered to as full-waveform inversion (FWI) methods. FWI methods account for most wave phenomena during the reconstruction. FWI methods in general have a high computational complexity required to solve the non-linear inverse problem. FWI methods have the advantage that they reconstruct high-resolution images containing quantitative information abouth the tissue parameters, see Fig. 1.6 [35]. In addition, a classified image is generated by using images obtained with FWI in a classification algorithm. In this thesis, we use contrast source in-

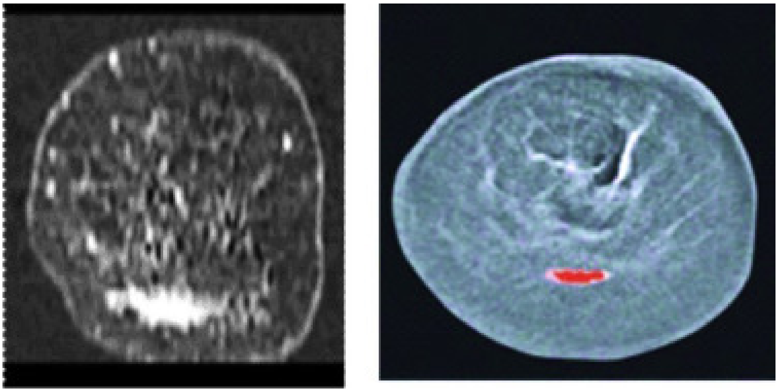

Figure 1.5: 74 year old patient with large breast tumor (left breast). Left: Frontal MRI subtraction slice. Right: USCT slices at approximately the same position as tresholded-overlay [24].

version (CSI) as an example FWI method.

FEASIBILITY OF 3-D INVERSION

In practice, the application of FWI for breast ultrasound represents a 3-D inverse problem due to the shape and internal structure of the breast as well as the employed measurement setup. Consequently, it is desired to use a 3-D inversion method to obtain an accurate reconstruction. Moreover, using a 2-D approximation of an essentially 3-D problem will give rise to inaccurate or erroneous reconstructions. However, the computational complexity involved with 3-D inversion limits its applicability.

This numerical challenge can easily be explained for a measurement setup as shown in Fig. 1.4. Let's assume that the object of interest, a sphere with a diameter of 0.2 m, is scanned using a wave field that has a central frequency of 1.5 MHz. Assuming that a spatial sampling of at least five points per wavelength is used, the spatial domain will be discretised into at least $1000 \times 1000 \times 1000$ elements. Considering the number of sources and frequencies required for FWI as well as the fact that the frequency-domain inversion uses double-precision complex numbers, array sizes required for the inversion will be in the order of TB of memories.

Due to the high computational requirements for 3-D inversion, we have chosen to limit ourselves to 2-D inversion. Since the synthetic examples and lab measurements that are used in this work are designed to represent a 2-D environment, application of 2-D inversion will not cause a significant problem. Fortunately, application of the ideas presented in the thesis to a 3-D environment is straightforward; moreover, a 3-D inversion example of a small spatial domain is presented in Appendix A.

TIME VERSUS FREQUENCY DOMAIN INVERSION

The FWI method used in this thesis – CSI – is based on solving the scattering integral equation and works in the frequency domain. Most other FWI methods are based on time-domain finite-difference modeling methods. These time-domain methods usually

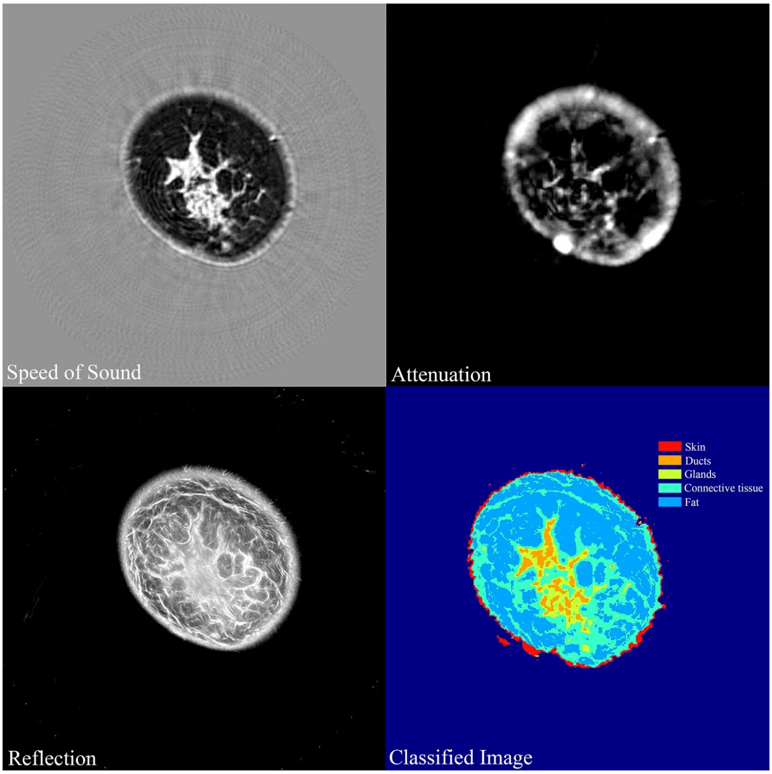

Figure 1.6: Image classification using the SVM classifier. The speed of sound, attenuation and reflection images are used together by the classifier to generate a tissue-color-coded classified image [35].

require a denser spatial sampling as compared to the scattering integral based methods in order to satisfy the Courant condition and to avoid effects such as numerical dispersion. In addition, for the frequency-domain methods only a few frequency components are usually sufficient to conduct the inversion, which makes CSI computationally attractive [36], [37]. Based on these arguments, we believe that frequency-domain methods are preferable over time-domain methods.

1.4. FROM SINGLE-PARAMTER TO MULTI-PARAMETER INVERSION

FWI has already been applied succesfully for breast cancer detection using water bath scanning systems [31], [38]. In this thesis, we aim to overcome some common problems encountered when FWI is applied for these systems.

To begin with, we examined the effect of commonly made approximations when modeling the acoustic waves propagating through the breast. It is shown that attenuation has a limited effect on the scattering for frequencies below 1 MHz. In addition, it is shown that full-wave modeling is far more accurate than ray, Born, and paraxial approximation based methods.

Finally, we propose a multi-parameter FWI method. This method takes advantage of a novel redatuming method that also works for non-planar scanning geometries. Moreover, with the aid of this new redatuming method, the efficiency of FWI can be increased significantly. In addition, redatuming may be used to filter noise out of the data or to correct for the misalignment of the receivers with respect to the grid.

1.5. THESIS OUTLINE

In this thesis the following outline is used.

- Chapter 2 describes the theoretical framework of acoustic wave propagation.
- Chapter 3 introduces the forward model used in this thesis. The presented model allows for a heterogeneous medium with contrasts in compressibility, mass density and attenuation. The effects of these contrasts (separately and combined) on the wave field are analyzed using a numerical breast phantom. In addition, the applicability of commonly made approximations to model the acoustic wave propagation is investigated.
- Chapter 4 introduces CSI and proposes a solution to the cycle-skipping problem by implementing a frequency-hopping technique.
- Chapter 5 introduces a redatuming method that is optimized for water-bath scanners. The redatuming method is based on Hankel function decomposition. With the proposed method the pressure field measured at an arbitrary closed curve can be backpropagated in the homogeneous embedding towards the object of interest. Using a numerical example, the general preformance of the proposed redatuming method is analyzed. Finally, an example using real measurement data is presented to test the applicability of redatuming in combination with FWI.
- Chapter 6 investigates the feasibility of multi-parameter inversion for breast ultrasound. First, we introduce a method to compute the particle velocity field from pressure field measurements. Next, we present a single-parameter and a multi-parameter inversion scheme. With a synthetic example we compare the results obtained with single-parameter and multi-parameter inversion.
- Chapter 7 describes the main conclusions derived from this thesis, followed by recommendations for future research.

2

ACOUSTIC WAVE THEORY

2.1. ACOUSTIC WAVE EQUATIONS FOR LOSSY MEDIUM

Starting point for the derivation of the acoustic wave equations used throughout this thesis is the equation of motion and equation of deformation, which equal

$$\nabla p(\boldsymbol{x},t) + \dot{\boldsymbol{\Phi}}(\boldsymbol{x},t) = \boldsymbol{f}(\boldsymbol{x},t), \tag{2.1}$$

$$\nabla \cdot \boldsymbol{v}(\boldsymbol{x},t) - \dot{\Theta}(\boldsymbol{x},t) = q(\boldsymbol{x},t), \tag{2.2}$$

where $p(\boldsymbol{x},t)$ is the acoustic pressure wave field, $\boldsymbol{v}(\boldsymbol{x},t)$ is the particle velocity wave field, $\dot{\boldsymbol{\Phi}}(\boldsymbol{x},t)$ is the mass-flow density rate, $\dot{\Theta}(\boldsymbol{x},t)$ is the induced part of the cubic dilatation rate, $\boldsymbol{f}(\boldsymbol{x},t)$ is the volume source density of volume force and $q(\boldsymbol{x},t)$ is the volume source density of injection rate. Spatial Cartesian coordinates (x,y,z) are represented by the vector $\boldsymbol{x}$ and time is denoted by the parameter t. Finally, $\nabla = \left(\frac{\partial}{\partial x}, \frac{\partial}{\partial y}, \frac{\partial}{\partial z}\right)$ is the nabla operator and is used to denote spatial derivatives in Cartesian coordinates.

The mass-flow density rate $\dot{\boldsymbol{\Phi}}(\boldsymbol{x},t)$ and the induced part of the cubic dilatation rate $\dot{\Theta}(\boldsymbol{x},t)$ depend on the acoustic medium parameters and are given by

$$\dot{\boldsymbol{\Phi}}(\boldsymbol{x},t) = \rho(\boldsymbol{x}) D_t \boldsymbol{v}(\boldsymbol{x},t), \tag{2.3}$$

$$\dot{\Theta}(\boldsymbol{x},t) = -\kappa(\boldsymbol{x}) D_t [m(\boldsymbol{x},t) *_t p(\boldsymbol{x},t)], \tag{2.4}$$

where $\rho(\boldsymbol{x})$ is the volume density of mass, $\kappa(\boldsymbol{x})$ is the compressibility and $m(\boldsymbol{x},t)$ is a causal compliance relaxation function that models absorption. A convolution with respect to time is denoted as $*_t$ and the material time derivative D_t is given as

$$D_t = \frac{\partial}{\partial t} + \boldsymbol{v} \cdot \nabla. \tag{2.5}$$

Under the low-velocity approximation that states that for low amplitude acoustic signals the particle velocity is small, the material time derivative D_t reduces to $\frac{\partial}{\partial t}$. Employing this approximation and inserting equations (2.3) and (2.4) into (2.1) and (2.2) yields the following set of field equations

$$\nabla p(\boldsymbol{x},t) + \rho(\boldsymbol{x})\frac{\partial}{\partial t}\boldsymbol{v}(\boldsymbol{x},t) = \boldsymbol{f}(\boldsymbol{x},t), \tag{2.6}$$

$$\nabla\cdot \boldsymbol{v}(\boldsymbol{x},t) + \kappa(\boldsymbol{x})\frac{\partial}{\partial t}[m(\boldsymbol{x},t) *_t p(\boldsymbol{x},t)] = q(\boldsymbol{x},t). \tag{2.7}$$

After applying a temporal Fourier transform to equations (2.6) and (2.7), they can be written in the frequency domain as

$$\nabla \hat{p}(\boldsymbol{x}) + i\omega\rho(\boldsymbol{x})\hat{\boldsymbol{v}}(\boldsymbol{x}) = \hat{\boldsymbol{f}}(\boldsymbol{x}), \tag{2.8}$$

$$\nabla\cdot \hat{\boldsymbol{v}}(\boldsymbol{x}) + i\omega\kappa(\boldsymbol{x})\hat{m}(\boldsymbol{x})\hat{p}(\boldsymbol{x}) = \hat{q}(\boldsymbol{x}), \tag{2.9}$$

where ω is the angular frequency. The caret symbol ^ is used to express that a quantity is defined in the temporal Fourier domain where the temporal Fourier transformation is defined as

$$\hat{u}(\omega) = \mathscr{F}\{u(t)\} = \int_{-\infty}^{\infty} u(t)\exp(-i\omega t)dt. \tag{2.10}$$

Note that including the background medium parameters in equations (2.8) and (2.9) yield the following set of field equations

$$\nabla \hat{p}(\boldsymbol{x}) + i\omega\rho_0\hat{\boldsymbol{v}}(\boldsymbol{x}) = \hat{\boldsymbol{f}}(\boldsymbol{x}) - i\omega(\rho(\boldsymbol{x})-\rho_0)\hat{\boldsymbol{v}}(\boldsymbol{x}), \tag{2.11}$$

$$\nabla\cdot \hat{\boldsymbol{v}}(\boldsymbol{x}) + i\omega\kappa_0\hat{m}_0\hat{p}(\boldsymbol{x}) = \hat{q}(\boldsymbol{x}) - i\omega[\kappa(\boldsymbol{x})\hat{m}(\boldsymbol{x}) - \kappa_0\hat{m}_0]\hat{p}(\boldsymbol{x}), \tag{2.12}$$

where ρ_0, κ_0 and $\hat{m}_0$ are the acoustic medium properties of the homogeneous background medium.

2.1.1. PRESSURE FIELD

The inhomogeneous Helmholtz equation for lossy heterogeneous media is obtained by combining equations (2.11) and (2.12). The resulting equation reads

$$\begin{aligned}\nabla^2\hat{p}(\boldsymbol{x}) + \omega^2\rho_0\kappa_0\hat{m}_0\hat{p}(\boldsymbol{x}) = &-i\omega\rho_0\hat{q}(\boldsymbol{x}) + \nabla\cdot\hat{\boldsymbol{f}}(\boldsymbol{x})\\ &-\nabla\cdot[i\omega(\rho(\boldsymbol{x})-\rho_0)\hat{\boldsymbol{v}}(\boldsymbol{x})]\\ &-\omega^2\rho_0[\kappa(\boldsymbol{x})\hat{m}(\boldsymbol{x}) - \kappa_0\hat{m}_0]\hat{p}(\boldsymbol{x}),\end{aligned} \tag{2.13}$$

where $\nabla^2 = \nabla\cdot\nabla$ is the Laplace operator.

Introducing the wave number $\hat{k}_0 = \omega\sqrt{\rho_0\kappa_0 m_0}$, equation (2.13) can be rewritten in compact form as

$$\nabla^2 \hat{p}(\boldsymbol{x}) + \hat{k}_0^2 \hat{p}(\boldsymbol{x}) = -\hat{S}_{\text{pr}}(\boldsymbol{x}) - \hat{S}_{\text{cs}}(\boldsymbol{x}), \tag{2.14}$$

with primary source term

$$\hat{S}_{\text{pr}}(\boldsymbol{x}) = i\omega\rho_0 \hat{q}(\boldsymbol{x}) - \nabla\cdot \hat{\boldsymbol{f}}(\boldsymbol{x}), \tag{2.15}$$

2

and contrast source term

$$\hat{S}_{\text{cs}}(\boldsymbol{x}) = i\omega\rho_0 \nabla\cdot [\chi^{\rho}(\boldsymbol{x})\hat{\boldsymbol{v}}(\boldsymbol{x})] + \hat{k}_0^2 \hat{\chi}^{\kappa}(\boldsymbol{x})\hat{p}(\boldsymbol{x}), \tag{2.16}$$

where the contrast functions $\chi^{\rho}(\boldsymbol{x})$ and $\hat{\chi}^{\kappa}(\boldsymbol{x})$ are equal to

$$\chi^{\rho}(\boldsymbol{x}) = \frac{\rho(\boldsymbol{x}) - \rho_0}{\rho_0}, \tag{2.17}$$

$$\hat{\chi}^{\kappa}(\boldsymbol{x}) = \frac{\kappa(\boldsymbol{x})\hat{m}(\boldsymbol{x}) - \kappa_0 \hat{m}_0}{\kappa_0 \hat{m}_0}. \tag{2.18}$$

Note that, in the absence of absorption $\hat{m}(\boldsymbol{x}) = 1$ and contrast function $\hat{\chi}^{\kappa}(\boldsymbol{x})$ in equation (2.18) reduces to

$$\chi^{\kappa}(\boldsymbol{x}) = \frac{\kappa(\boldsymbol{x}) - \kappa_0}{\kappa_0}. \tag{2.19}$$

2.1.2. PARTICLE VELOCITY FIELD

To obtain the wave equation for the particle velocity field, equations (2.11) and (2.12) are combined to yield

$$\begin{aligned} \nabla[\nabla\cdot \hat{\boldsymbol{v}}(\boldsymbol{x})] + \hat{k}_0^2 \hat{\boldsymbol{v}}(\boldsymbol{x}) =& \nabla \hat{q}(\boldsymbol{x}) - i\omega\kappa_0 \hat{m}_0 \hat{\boldsymbol{f}}(\boldsymbol{x}) \\ &+ i\omega\nabla[\{\kappa_0 \hat{m}_0 - \kappa(\boldsymbol{x})\hat{m}(\boldsymbol{x})\}\hat{p}(\boldsymbol{x})] \\ &+ \omega^2 \kappa_0 \hat{m}_0 [\rho_0 - \rho(\boldsymbol{x})]\hat{\boldsymbol{v}}(\boldsymbol{x}). \end{aligned} \tag{2.20}$$

Using the vector calculus identity $\nabla(\nabla\cdot \boldsymbol{A}) = \nabla^2 \boldsymbol{A} + \nabla\times\nabla\times \boldsymbol{A}$ and reorganizing the right-hand side of equation (2.20) yields

$$\begin{aligned} \nabla^2 \hat{\boldsymbol{v}}(\boldsymbol{x}) + \nabla\times\nabla\times \hat{\boldsymbol{v}}(\boldsymbol{x}) + \hat{k}_0^2 \hat{\boldsymbol{v}}(\boldsymbol{x}) =& \nabla \hat{q}(\boldsymbol{x}) - i\omega\kappa_0 \hat{m}_0 \hat{\boldsymbol{f}}(\boldsymbol{x}) \\ &- i\omega\kappa_0 \hat{m}_0 \nabla[\hat{\chi}^{\kappa}(\boldsymbol{x})\hat{p}(\boldsymbol{x})] \\ &- \hat{k}_0^2 \chi^{\rho}(\boldsymbol{x})\hat{\boldsymbol{v}}(\boldsymbol{x}). \end{aligned} \tag{2.21}$$

To compute the term $\nabla\times\nabla\times \hat{\boldsymbol{v}}(\boldsymbol{x})$ we use equation (2.11) as starting point, hence

$$\nabla\times\nabla\times \hat{\boldsymbol{v}}(\boldsymbol{x}) = \nabla\left(\nabla\cdot \frac{\hat{\boldsymbol{f}}(\boldsymbol{x})}{i\omega\rho_0}\right) - \nabla^2 \frac{\hat{\boldsymbol{f}}(\boldsymbol{x})}{i\omega\rho_0} - \nabla\left(\nabla\cdot[\chi^{\rho}(\boldsymbol{x})\hat{\boldsymbol{v}}(\boldsymbol{x})]\right) + \nabla^2[\chi^{\rho}(\boldsymbol{x})\hat{\boldsymbol{v}}(\boldsymbol{x})]. \tag{2.22}$$

Combining equation (2.21) and (2.22) leads to

$$\begin{aligned} \nabla^2 \hat{\boldsymbol{v}}(\boldsymbol{x}) + \nabla\left(\nabla\cdot \frac{\hat{\boldsymbol{f}}(\boldsymbol{x})}{i\omega\rho_0}\right) - \nabla^2 \frac{\hat{\boldsymbol{f}}(\boldsymbol{x})}{i\omega\rho_0} - \nabla\left(\nabla\cdot[\chi^{\rho}(\boldsymbol{x})\hat{\boldsymbol{v}}(\boldsymbol{x})]\right) + \nabla^2[\chi^{\rho}(\boldsymbol{x})\hat{\boldsymbol{v}}(\boldsymbol{x})] \\ + \hat{k}_0^2 \hat{\boldsymbol{v}}(\boldsymbol{x}) =& \nabla \hat{q}(\boldsymbol{x}) + \hat{k}_0^2 \frac{\hat{\boldsymbol{f}}(\boldsymbol{x})}{i\omega\rho_0} \\ &- i\omega\kappa_0 \hat{m}_0 \nabla[\hat{\chi}^{\kappa}(\boldsymbol{x})\hat{p}(\boldsymbol{x})] \\ &- \hat{k}_0^2 \chi^{\rho}(\boldsymbol{x})\hat{\boldsymbol{v}}(\boldsymbol{x}). \end{aligned} \tag{2.23}$$

Reorganizing equation (2.23) leads to

$$\begin{aligned}\nabla^2\left(\hat{\boldsymbol{v}}(\boldsymbol{x})+\chi^\rho(\boldsymbol{x})\hat{\boldsymbol{v}}(\boldsymbol{x})-\frac{\hat{\boldsymbol{f}}(\boldsymbol{x})}{i\omega\rho_0}\right)+\hat{k}_0^2\left(\hat{\boldsymbol{v}}(\boldsymbol{x})+\chi^\rho(\boldsymbol{x})\hat{\boldsymbol{v}}(\boldsymbol{x})-\frac{\hat{\boldsymbol{f}}(\boldsymbol{x})}{i\omega\rho_0}\right)&\\ =\nabla\hat{q}(\boldsymbol{x})-\nabla\nabla\cdot\frac{\hat{\boldsymbol{f}}(\boldsymbol{x})}{i\omega\rho_0}&\\ -i\omega\kappa_0\hat{m}_0\nabla[\hat{\chi}^\kappa(\boldsymbol{x})\hat{p}(\boldsymbol{x})]&\\ +\nabla\nabla\cdot[\chi^\rho(\boldsymbol{x})\hat{\boldsymbol{v}}(\boldsymbol{x})].&\end{aligned} \tag{2.24}$$

2.2. INTEGRAL EQUATION FORMULATION

Equation (2.14) is known as the inhomogenous Helmholtz equation for heterogenous media and can be solved by using Green‘s functions. Here, the Green‘s function $\hat{G}(\boldsymbol{x})$ is defined as the impulse response of the homogeneous background medium. Consequently, $\hat{G}(\boldsymbol{x})$ satisfies the following inhomogeneous Helmholtz equation

$$\nabla^2\hat{G}(\boldsymbol{x})+\hat{k}_0^2\,\hat{G}(\boldsymbol{x})=-\delta(\boldsymbol{x}), \tag{2.25}$$

where $\delta(\boldsymbol{x})$ is the Dirac delta function. For the three-dimesional (3-D) case the resulting Green’s function equals

$$\hat{G}(\boldsymbol{x})=\frac{e^{-i\hat{k}_0|\boldsymbol{x}|}}{4\pi|\boldsymbol{x}|}. \tag{2.26}$$

In view of the above, a solution for the inhomogeneous Helmholtz equation for lossy heterogeneous media, see equation (2.14), can be obtained by convolving the Green‘s function $\hat{G}(\boldsymbol{x})$ with the source term, hence

$$\hat{p}(\boldsymbol{x})=\hat{G}(\boldsymbol{x})*_{\boldsymbol{x}}\{\hat{S}_{\rm pr}(\boldsymbol{x})+\hat{S}_{\rm cs}(\boldsymbol{x})\}, \tag{2.27}$$

where $*_{\boldsymbol{x}}$ represents a spatial convolution. Equation (2.27) shows that the pressure field may be seen as the summation of an incident field $\hat{p}^{\rm inc}(\boldsymbol{x})$ generated by the primary source $\hat{S}_{\rm pr}(\boldsymbol{x})$, viz.

$$\hat{p}^{\rm inc}(\boldsymbol{x})=\hat{G}(\boldsymbol{x})*_{\boldsymbol{x}}\hat{S}_{\rm pr}(\boldsymbol{x}), \tag{2.28}$$

and a scattered field $\hat{p}^{\rm sct}(\boldsymbol{x})$ generated by the contrast sources, viz.

$$\hat{p}^{\rm sct}(\boldsymbol{x})=\hat{G}(\boldsymbol{x})*_{\boldsymbol{x}}\hat{S}_{\rm cs}(\boldsymbol{x}). \tag{2.29}$$

Consequently, the pressure field may be described as a Fredholm integral equation of the second kind that equals

$$\begin{aligned}\hat{p}(\boldsymbol{x})=\hat{p}^{\rm inc}(\boldsymbol{x})+\hat{k}_0^2\int_{\boldsymbol{x}'\in\mathbb{D}}\hat{G}(\boldsymbol{x}-\boldsymbol{x}')\hat{\chi}^\kappa(\boldsymbol{x}')\hat{p}(\boldsymbol{x}')dV&\\ +i\omega\rho_0\int_{\boldsymbol{x}'\in\mathbb{D}}\hat{G}(\boldsymbol{x}-\boldsymbol{x}')\nabla\cdot[\chi^\rho(\boldsymbol{x}')\hat{\boldsymbol{v}}(\boldsymbol{x}')]dV.&\end{aligned} \tag{2.30}$$

where $\mathbb{D}$ is the spatial domain where the contrast functions $\chi^\rho(\boldsymbol{x})$ and $\hat{\chi}^\kappa(\boldsymbol{x})$ are non-zero. Note that, equation (2.30) includes the particle velocity field and it is this form that is used in Chapter 6. Equation (2.30) can also be written with presure field only, and this form is used in Chapter 3. With the pressure field only equation (2.30) becomes

$$\begin{aligned}\hat{p}(\boldsymbol{x}) = \hat{p}^{\text{inc}}(\boldsymbol{x}) + \hat{k}_0^2 \int_{\boldsymbol{x}' \in \mathbb{D}} \hat{G}(\boldsymbol{x}-\boldsymbol{x}^{'})\hat{\chi}^{\kappa}(\boldsymbol{x}^{'})\hat{p}(\boldsymbol{x}^{'})dV \\ - \int_{\boldsymbol{x}' \in \mathbb{D}} \hat{G}(\boldsymbol{x}-\boldsymbol{x}^{'})\nabla\cdot\left[\frac{\rho_0}{\rho(\boldsymbol{x}^{'})}\chi^{\rho}(\boldsymbol{x}^{'})\nabla\hat{p}(\boldsymbol{x}^{'})\right]dV,\end{aligned} \tag{2.31}$$

where it assumed that the sources are in the homogeneous background medium.

Note that, if density is assumed to be constant, the second integral term on the right-hand side of equation 2.31 drops. It is this form that is used in Chapters 4 and 5. Equation 2.31 describes full-wave solution acoustical wave propagation in heterogeneous medium.

The Born approximation can be easily applied here by replacing the total pressure field $\hat{p}(\boldsymbol{x})$ inside the integrals with the incident pressure field $\hat{p}^{\text{inc}}(\boldsymbol{x})$. The Born approximation as well as some other modeling methods are described in detail in Chapter 3.

In a similar way as in equation 2.31, the particle velocity field can be written in integral representation as

$$\begin{aligned}\hat{\boldsymbol{v}}(\boldsymbol{x}) = \hat{\boldsymbol{v}}^{\text{inc}}(\boldsymbol{x}) + i\omega\kappa_0\hat{m}_0\nabla \int_{\boldsymbol{x}' \in \mathbb{D}} \hat{G}(\boldsymbol{x}-\boldsymbol{x}^{'})\hat{\chi}^{\kappa}(\boldsymbol{x}^{'})\hat{p}(\boldsymbol{x}^{'})\mathrm{d}V(\boldsymbol{x}^{'}) \\ -\nabla\nabla\cdot\int_{\boldsymbol{x}' \in \mathbb{D}} \hat{G}(\boldsymbol{x}-\boldsymbol{x}^{'})\chi^{\rho}(\boldsymbol{x}^{'})\hat{\boldsymbol{v}}(\boldsymbol{x}^{'})\mathrm{d}V(\boldsymbol{x}^{'}) - \chi^{\rho}(\boldsymbol{x})\hat{\boldsymbol{v}}(\boldsymbol{x}),\end{aligned} \tag{2.32}$$

where the incident particle velocity field is defined as

$$\begin{aligned}\hat{\boldsymbol{v}}^{\text{inc}}(\boldsymbol{x}) = -\nabla \int_{\boldsymbol{x}' \in \mathbb{D}} \hat{G}(\boldsymbol{x}-\boldsymbol{x}^{'})\hat{q}(\boldsymbol{x}^{'})\mathrm{d}V(\boldsymbol{x}^{'}) \\ +\nabla\nabla\cdot\int_{\boldsymbol{x}' \in \mathbb{D}} \hat{G}(\boldsymbol{x}-\boldsymbol{x}^{'})\frac{\hat{\boldsymbol{f}}(\boldsymbol{x}^{'})}{i\omega\rho_0}\mathrm{d}V(\boldsymbol{x}^{'}) + \frac{\hat{\boldsymbol{f}}(\boldsymbol{x})}{i\omega\rho_0}.\end{aligned} \tag{2.33}$$

3

MODELING BREAST ULTRASOUND; ON THE APPLICABILITY OF COMMONLY MADE APPROXIMATIONS[1]

To design breast ultrasound scanning systems or to test new imaging methods, various computer models are used to simulate the acoustic wave field propagation through a breast. The computer models vary in complexity depending on the applied approximations. The objective of this chapter is to investigate how the applied approximations affect the resulting wave field. In particular, we investigate the importance of taking three-dimensional (3-D) spatial variations in the compressibility, volume density of mass, and attenuation into account. In addition, we compare four 3-D solution methods: a full-wave method, a Born approximation method, a parabolic approximation method, and a ray-based method. Results show that, for frequencies below 1 MHz, the amplitude of the fields scattering off the compressibility or density contrasts are at least 24 dB higher than the amplitude of the fields scattering off the attenuation contrasts. The results also show that considering only speed of sound as a contrast is a valid approximation. In addition, it is shown that the pressure field modeled with the full-wave method is more accurate than the fields modeled using the other three methods. Finally, the accuracy of the full-wave method is location independent whereas the accuracy of the other methods strongly depends on the point of observation.

[1] This chapter has been published as:
Taskin et al., "Modeling breast ultrasound; on the applicability of commonly made approximations," Arch. Acoust. 43(3), 2018.
The text and notation used in this chapter may differ on minor details from the actual publication. This is done to achieve consistency between chapters and will especially be the case for the section Theory.

3.1. INTRODUCTION

Breast cancer is the most frequently diagnosed type of cancer and among the leading causes of death for women worldwide. Several studies show that detecting the tumor at an early stage significantly increases the survival rate [39]. Currently, X-ray mammography is generally used in screening programs since it is the "golden standard" for breast cancer examination. However, it can miss tumors in young women with dense breasts as the healthy fibrous and glandular tissues, as well as cancerous lumps, show up white on mammograms [40]. Fortunately, ultrasound has the capability to differentiate between these tissues and therefore it has the potential to detect cancer in dense breasts. In addition, it is patient-friendly, safe, fast, cost-effective and avoids the use of ionizing radiation. To improve breast cancer diagnosis, automated whole-breast ultrasound scanning systems [26], [41], [42] and ultrasound imaging algorithms [31], [43]–[45] are being developed.

To optimize the design of a breast scanner, it is essential to model the acoustic wave field generated by the system. In addition, to test new imaging methods, computer models can be used as an appropriate, inexpensive, and flexible approach for generating synthetic measurement data. However, for these models to be useful, it is important to know (i) what the relevant medium parameters are and (ii) the applicability of approximations commonly made to reduce the computational costs involved in solving the forward problem. It is the objective of this chapter to investigate those two aspects.

To investigate what the relevant medium parameters are, we model the pressure field using a three-dimensional (3-D) full-wave method. The applied method uses a frequency-domain integral equation formulation to describe the wave propagation in media with spatially varying compressibility, volume density of mass and attenuation [46], [47]. The applied numerical breast model is built from an MRI scan of cancerous breast [48]. Time-domain results are obtained by applying Fourier transformations. The method accounts for refraction, diffraction, multiple reflections, and/or dispersion effects.

The same full-wave method is used to examine the performance of commonly used approximations to solve the forward problem in biomedical ultrasound. In particular, we will evaluate the Born approximation [43], paraxial approximation [49] and ray based method [50]. The effects of these approximations are studied by comparing the resulting wave fields with the solutions obtained with the full-wave method. We used the basic form of each approximation instead of recent methods based on these approximations that can give more accurate results. The main reason behind this selection is to point out possible problems each approximation may bring.

The integral equation formulation [51] has the advantage that it allows the problem to be solved at a predefined accuracy using an iterative solution method [52]. In this work a conjugate gradient iterative solution method is used [53]. An additional advantage of the frequency-domain formulation is that it leads to a reduction of computational complexity. This is especially the case, if one is only interested in the dominant spectral component of the temporal signal. Since each frequency component may be considered as an independent problem, parallelization techniques can be used to reduce the computational time.

To investigate the aforementioned aspects, we start Section 3.2 with introducing the integral equation formulation for the acoustic wave field. Section 3.3 provides details about four different solution methods: full-wave method, Born approximation, paraxial approximation and ray based method. Section 3.4 first validates the accuracy of the full-wave method using the analytical solution for a plane wave scattering off a spherical contrast. Next, it evaluates how the different medium properties affect the pressure wave field and ends with comparing the time-domain results obtained with the four solution methods. Finally, Section 3.5 contains a discussion of the obtained results and a final conclusion.

3.2. THEORY

The propagation of acoustic pressure wave fields in heterogeneous media is governed by the wave equation. Derivation of this wave equation starts with the equations of motion and deformation. As shown in Chapter 2, in the frequency domain these equations equal

$$\nabla \hat{p}(\boldsymbol{x}) + i\omega\rho(\boldsymbol{x})\hat{\boldsymbol{v}}(\boldsymbol{x}) = \hat{\boldsymbol{f}}(\boldsymbol{x}), \tag{3.1}$$

$$\nabla \cdot \hat{\boldsymbol{v}}(\boldsymbol{x}) + i\omega\kappa(\boldsymbol{x})\hat{m}(\boldsymbol{x})\hat{p}(\boldsymbol{x}) = \hat{q}(\boldsymbol{x}), \tag{3.2}$$

where $\hat{p}(\boldsymbol{x})$ is the acoustic pressure wave field, $\hat{\boldsymbol{v}}(\boldsymbol{x})$ is the particle velocity wave field, $\rho(\boldsymbol{x})$ is the volume density of mass, $\kappa(\boldsymbol{x})$ is the compressibility, $\hat{m}(\boldsymbol{x})$ is the causal compliance relaxation function to account for attenuation, $\hat{\boldsymbol{f}}(\boldsymbol{x})$ is the volume source density of volume force, and $\hat{q}(\boldsymbol{x})$ is the volume source density of injection rate, ∇ is the nabla operator, ω is the angular frequency, and $\boldsymbol{x}$ is the spatial coordinate in the 3-D spatial domain $\mathbb{D}$ [54]–[57]. The caret symbol ˆ is used to express that a quantity is defined in the temporal Fourier domain. Combining equations (3.1) and (3.2) results in the inhomogeneous Helmholtz equation for heterogeneous media, i.e.

$$\begin{aligned}\nabla^2 \hat{p}(\boldsymbol{x}) - \hat{\gamma}_0^2\hat{p}(\boldsymbol{x}) = &- i\omega\rho_0\hat{q}(\boldsymbol{x}) \\ &+ \nabla\cdot[\frac{\rho_0}{\rho(\boldsymbol{x})}\chi_\rho(\boldsymbol{x})\nabla\hat{p}(\boldsymbol{x})] \\ &+ \hat{\chi}_\gamma(\boldsymbol{x})\hat{p}(\boldsymbol{x}),\end{aligned} \tag{3.3}$$

where $\nabla^2 = \nabla\cdot\nabla$ is the Laplace operator, $\hat{\gamma}_0 = i\omega\sqrt{\rho_0\kappa_0 m_0}$ is the propagation coefficient of the embedding (note that $\hat{\gamma}_0 = i\hat{k}_0$), and $\chi_\rho(\boldsymbol{x})$ and $\hat{\chi}_\gamma(\boldsymbol{x})$ are contrast functions. These contrast functions depend on the spatially varying medium properties compressibility, density and attenuation, and are equal to

$$\chi_\rho(\boldsymbol{x}) = \frac{\rho(\boldsymbol{x}) - \rho_0}{\rho_0} \tag{3.4}$$

and

$$\hat{\chi}_\gamma(\boldsymbol{x}) = \frac{\rho_0}{\rho(\boldsymbol{x})}\hat{\gamma}^2(\boldsymbol{x}) - \hat{\gamma}_0^2. \tag{3.5}$$

In equations (3.3) to (3.5) it is assumed that the wave fields are solely generated by a volume source density of injection rate source $\hat{q}(\boldsymbol{x})$, hence $\hat{\boldsymbol{f}}(\boldsymbol{x}) = 0$.

To account for the power law attenuation commonly observed in biomedical tissue, the complex propagation coefficient $\hat{\gamma}(\boldsymbol{x})$ is expressed as

$$\hat{\gamma}(\boldsymbol{x}) = \hat{\alpha}(\boldsymbol{x}) + i\hat{\beta}(\boldsymbol{x}), \tag{3.6}$$

where the attenuation coefficient $\hat{\alpha}(\boldsymbol{x})$ and phase coefficient $\hat{\beta}(\boldsymbol{x})$ equal [58]

$$\hat{\alpha}(\boldsymbol{x}) = \alpha_1(\boldsymbol{x})\,|\omega|^{b(\boldsymbol{x})}, \tag{3.7}$$

$$\hat{\beta}(\boldsymbol{x}) = \frac{\omega}{c_{\text{ref}}} + \alpha_1(\boldsymbol{x})\tan\left[\frac{\pi}{2}b(\boldsymbol{x})\right]\omega(|\omega|^{b(\boldsymbol{x})-1} - |\omega_{\text{ref}}|^{b(\boldsymbol{x})-1}), \tag{3.8}$$

3

with

$$\alpha_1(\boldsymbol{x}) = a(\boldsymbol{x})(2\pi)^{-b(\boldsymbol{x})}, \tag{3.9}$$

where ω_{ref} is the angular reference frequency at which the speed of sound and attenuation coefficients have been measured and the medium parameters $a(\boldsymbol{x})$ and $b(\boldsymbol{x})$ reflect the attenuation.

Equation (3.3) can be recasted into an integral equation which equals

$$\hat{p}(\boldsymbol{x}) = \hat{p}^{\text{inc}}(\boldsymbol{x}) - \int_{\boldsymbol{x}'\in\mathbb{D}} \hat{G}(\boldsymbol{x}-\boldsymbol{x}')\nabla\cdot\left[\frac{\rho_0}{\rho(\boldsymbol{x}')}\chi_\rho(\boldsymbol{x}')\nabla\hat{p}(\boldsymbol{x})\right]\mathrm{d}V - \int_{\boldsymbol{x}'\in\mathbb{D}} \hat{G}(\boldsymbol{x}-\boldsymbol{x}')\hat{\chi}_\gamma(\boldsymbol{x}')\hat{p}(\boldsymbol{x}')\mathrm{d}V, \tag{3.10}$$

where $\hat{p}^{\text{inc}}(\boldsymbol{x})$ is referred to as the incident field, i.e., the pressure wave field generated by the primary sources and propagating in the homogeneous embedding and where $\hat{G}(\boldsymbol{x}-\boldsymbol{x}')$ is the free-space Green's function of the homogeneous embedding. This function satisfies the Sommerfeld radiation condition and the application of the absorbing boundary conditions or perfectly matched layers are not needed as long as the contrast is embedded in the background medium [59]. For the 3-D case the free-space Green's function of homogeneous background equals

$$\hat{G}(\boldsymbol{x}-\boldsymbol{x}') = \frac{e^{-\gamma_0|\boldsymbol{x}-\boldsymbol{x}'|}}{4\pi|\boldsymbol{x}-\boldsymbol{x}'|}. \tag{3.11}$$

In the remaining of the chapter, when it is mentioned that there is only a compressibility contrast it means that both the density and attenuation are constant and set to values corresponding to the embedding, hence, $\rho(\boldsymbol{x}) = \rho_0$, $a(\boldsymbol{x}) = a_0$ and $b(\boldsymbol{x}) = b_0$. The same procedure is followed in case that there is only a density or an attenuation contrast. For the case that all inhomogeneities are combined, every parameter has its actual value. The speed of sound case is an approximation that is commonly made. In this case attenuation is set to the embedding, and the contrast function χ_ρ given in equation (3.4) is set to zero. Only the contrast function χ_γ is non-zero where the speed of sound is based on the actual values of the compressibility and density.

3.3. SOLUTION METHODS

The forward problem refers to the situation where the unknown total pressure field $\hat{p}(\boldsymbol{x})$ is obtained for a known incident pressure field $\hat{p}^{\text{inc}}(\boldsymbol{x})$ and known contrast functions $\chi_\rho(\boldsymbol{x}')$ and $\hat{\chi}_\gamma(\boldsymbol{x}')$. Solving the forward problem via equation (3.10) requires the use of iterative schemes in situations when arbitrary shaped contrasts are considered; exact analytical solutions only exist for a limited number of configurations. In addition to the full-wave method, we also derive solution methods for the Born approximation, the paraxial approximation, and the ray based method.

3.3.1. FULL-WAVE METHOD

The presented full-wave method is based on the frequency-domain integral equation formulation as presented in equation (3.10) [46], [47]. This equation can be rewritten as

$$\begin{aligned}\hat{p}^{\mathrm{inc}}(\boldsymbol{x}) = \hat{p}(\boldsymbol{x}) &+ \int_{\boldsymbol{x}'\in\mathbb{D}} \hat{G}(\boldsymbol{x}-\boldsymbol{x}')\nabla\cdot\left[\frac{\rho_0}{\rho(\boldsymbol{x}')}\chi_\rho(\boldsymbol{x}')\nabla\hat{p}(\boldsymbol{x})\right]\mathrm{d}V \\ &+ \int_{\boldsymbol{x}'\in\mathbb{D}} \hat{G}(\boldsymbol{x}-\boldsymbol{x}')\hat{\chi}_\gamma(\boldsymbol{x}')\hat{p}(\boldsymbol{x}')\mathrm{d}V.\end{aligned} \tag{3.12}$$

In operator notation equation (3.12) equals

$$\mathsf{f} = \mathsf{L}[\mathsf{u}], \tag{3.13}$$

where f is the known incident pressure field $\hat{p}^{\mathrm{inc}}(\boldsymbol{x})$, u is the unknown total pressure field $\hat{p}(\boldsymbol{x})$, and L is the integral operator containing the Green's function $\hat{G}(\boldsymbol{x}-\boldsymbol{x}')$, and the known contrast functions $\chi_\rho(\boldsymbol{x}')$ and $\hat{\chi}_\gamma(\boldsymbol{x}')$. In our study, the linear system is solved iteratively by using the conjugate gradient method applied on the normal equation. The convergence of this method is known to be good [60]. With this method the unknown field at the n^{th} iteration step, i.e. u_n, is obtained by minimizing a cost functional. Hence, the approximate solution at the n^{th} iteration step equals

$$\mathsf{u}_\mathsf{n} = \mathsf{u}_{\mathsf{n}-1} + \alpha_\mathsf{n}\mathsf{d}_\mathsf{n}, \quad \mathsf{n} \geq 1, \tag{3.14}$$

where α_n is the step size and d_n is the update direction. The step size is determined according to the Fletcher-Reeves formula [61]. For any updated solution u_n the residual r_n is defined as

$$\mathsf{r}_\mathsf{n} = \mathsf{f} - \mathsf{L}[\mathsf{u}_\mathsf{n}], \tag{3.15}$$

and the normalized error Err_n is defined as

$$\mathsf{Err}_\mathsf{n} = \|\mathsf{r}_\mathsf{n}\| \,/\, \|\mathsf{f}\|, \tag{3.16}$$

with the properties $\mathsf{Err}_\mathsf{n} = 0$ if $\mathsf{u}_\mathsf{n} = \mathsf{u}$, and $\mathsf{Err}_\mathsf{n} = 1$ if $\mathsf{u}_\mathsf{n} = 0$, and where $\|\ldots\|^2$ represents the L_2-norm of a vector. The error is used as a measure for the accuracy attained in the iterative scheme. All detailed steps of the conjugate gradient method are given in Table 3.1. Note that problems associated with the singularity of the Green's function are solved by using its weak form [62].

3.3.2. BORN APPROXIMATION

In situations where the contrasts are small and the scattering is weak, the unknown total field $\hat{p}(\boldsymbol{x})$, inside the integrand of Equation (3.10) may be approximated by the known

Table 3.1: The conjugate gradient scheme. ($\mathsf{L}^\dagger$ is the adjoint operator.)

CG
$\mathsf{u}_0 = 0$
$\mathsf{r}_0 = \mathsf{f} - \mathsf{L}[\mathsf{u}_0]$
$\mathsf{d}_0 = \mathsf{r}_0$
$\mathsf{g}_0 = \mathsf{L}^\dagger[\mathsf{r}_0]$
for n = 1,2,...
$\quad \mathsf{g}_\mathsf{n} = \mathsf{L}^\dagger[\mathsf{r}_{\mathsf{n}-1}]$
$\quad \eta_\mathsf{n} = \Vert\mathsf{g}_\mathsf{n}\Vert^2 / \Vert\mathsf{g}_{\mathsf{n}-1}\Vert^2$
$\quad \mathsf{d}_\mathsf{n} = \mathsf{g}_\mathsf{n} + \eta_\mathsf{n}\mathsf{d}_{\mathsf{n}-1}$
$\quad \alpha_\mathsf{n} = \Vert\mathsf{g}_\mathsf{n}\Vert^2 / \Vert\mathsf{L}\mathsf{d}_\mathsf{n}\Vert^2$
$\quad \mathsf{u}_\mathsf{n} = \mathsf{u}_{\mathsf{n}-1} + \alpha_\mathsf{n}\mathsf{d}_\mathsf{n}$
$\quad \mathsf{r}_\mathsf{n} = \mathsf{f} - \mathsf{L}[\mathsf{u}_\mathsf{n}]$
$\quad \mathsf{Err}_\mathsf{n} = \Vert\mathsf{r}_\mathsf{n}\Vert / \Vert\mathsf{f}\Vert$
$\quad$ if $\mathsf{Err}_\mathsf{n} < \epsilon$ stop
$\quad$ if $\mathsf{n} > \mathsf{n}_{\mathsf{max}}$ stop
end

incident field $\hat{p}^{\text{inc}}(\boldsymbol{x})$, yielding the following equation

$$\begin{aligned}\hat{p}(\boldsymbol{x}) = \hat{p}^{\text{inc}}(\boldsymbol{x}) \\ &- \int_{\boldsymbol{x}'\in\mathbb{D}} \hat{G}(\boldsymbol{x}-\boldsymbol{x}')\nabla\cdot\left[\frac{\rho_0}{\rho(\boldsymbol{x}')}\chi_\rho(\boldsymbol{x}')\nabla\hat{p}^{\text{inc}}(\boldsymbol{x}')\right]\mathrm{d}V \\ &- \int_{\boldsymbol{x}'\in\mathbb{D}} \hat{G}(\boldsymbol{x}-\boldsymbol{x}')\hat{\chi}_\gamma(\boldsymbol{x}')\hat{p}^{\text{inc}}(\boldsymbol{x}')\mathrm{d}V.\end{aligned} \tag{3.17}$$

The unknown total field can now be computed directly and is similar to the field obtained after the first iteration step of the conjugate gradient solution method. Although this approximation neglects multiple scattering and possible phase shifts in the resulting field, it is highly efficient with respect to computational time.

3.3.3. PARAXIAL APPROXIMATION

To solve the wave equation within the paraxial approximation, the parabolic wave equation is used as a starting point [63]. Under the assumption that spatial variations depend on speed of sound, the Helmholtz equation reads

$$\nabla^2\hat{p}(\boldsymbol{x}) + \hat{k}^2(\boldsymbol{x})\hat{p}(\boldsymbol{x}) = 0, \tag{3.18}$$

where the wave number $\hat{k}(\boldsymbol{x})$ equals

$$\hat{k}(\boldsymbol{x}) = \frac{\omega}{c(\boldsymbol{x})}, \tag{3.19}$$

and where $c(\boldsymbol{x})$ is the speed of sound of the medium. After applying a spatial Fourier transform with respect to x and y equation (3.18) equals

$$\frac{\partial \tilde{p}}{\partial z^2} + (\tilde{k^2} *_{k_x,k_y} - k_x^2 - k_y^2)\tilde{p} = 0, \tag{3.20}$$

where the tilde symbol˜is used to express that a quantity is defined in the spatial Fourier domain (k_x, k_y) with Cartesian coordinate z, and where the symbol $*_{k_x,k_y}$ denotes a convolution with respect to the spatial frequency components (k_x, k_y). Equation (3.20) can be factorized into two parts, i.e.

$$\left[\frac{\partial}{\partial z} - i\tilde{k}_z\right]\left[\frac{\partial}{\partial z} + i\tilde{k}_z\right]\tilde{p} = 0, \tag{3.21}$$

with

$$\tilde{k}_z = \sqrt{\tilde{k^2} *_{k_x,k_y} - k_x^2 - k_y^2}. \tag{3.22}$$

To compute the wave propagating in the $+z$-direction, only the second part of the left-hand side of equation (3.21) is considered, hence

$$\left[\frac{\partial}{\partial z} + i\tilde{k}_z\right]\tilde{p} = 0. \tag{3.23}$$

A solution for the one-way wave equation (3.23) is obtained using the split-step method [64]. Using the known field in the plane $z = z_0$, the field at $z = z_o + \Delta$ can be computed in following way

$$\tilde{p}(k_x, k_y, z_0 + \Delta) = \tilde{p}(k_x, k_y, z_0)e^{-i\tilde{k}_z\Delta}, \tag{3.24}$$

where $\tilde{k}_z$ is approximated as

$$\tilde{k}_z = \hat{k}_{\text{mean}} + \frac{k_x^2 + k_y^2}{2\hat{k}_{\text{mean}}}, \tag{3.25}$$

with

$$\hat{k}_{\text{mean}} = \frac{\int \hat{k}(x, y, z)\mathrm{d}x\mathrm{d}y}{\int \mathrm{d}x\mathrm{d}y}. \tag{3.26}$$

This approximation is only valid when the angle between the z-axis and the direction of propagation is small. Note that that there are several methods to approximate $\tilde{k}_z$, all leading to similar results.

3.3.4. RAY BASED METHOD

The ray based method assumes that the pressure field travels along a straight path and spatial variations in the speed of sound only lead to phase shifts. Solutions for the forward problem are constructed by calculating the phase shifts for every point in the domain of interest [50]. Note that this is very simple form of ray-based modeling. In literature, there are advanced ray-based modeling methods that can account for reflection, multiple scattering, etc [65].

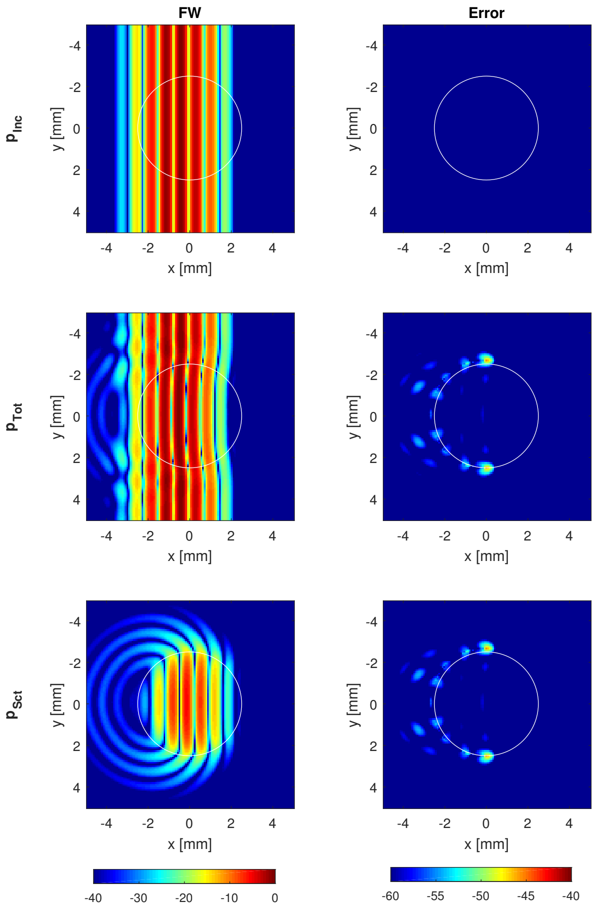

Figure 3.1: Snapshots of the incident (top row), total (middle row) and scattered (bottom row) pressure fields in dB *at time* $t = 4.75$ μs, *and in the plane* $z = 0$ m. *The first column shows the full-wave method, and the second column shows the error between the analytical and the full-wave solution. The white circle shows the contour of the sphere which is located in the middle of the domain.*

3.4. RESULTS

Numerical results are provided in this section in the following order. First, the full-wave method is validated using an analytical solution for a plane wave scattering off a spherical object. Next, several simulations are presented using a breast model with inhomogeneities in all four medium properties separately and combined. Finally, a comparison is made of the results obtained with different solution methods in case only inhomogeneities in the speed of sound are considered. All fields are on a dB scale and normalized with respect to the maximum absolute value of the incident field unless noted otherwise.

Table 3.2: Acoustic medium parameters for the breast [67]–[71].
* *assumed values*
** *at a temperature of 32°C*

	c [m/s]	ρ [kg/m^3]	κ [1/Pa]	a [dB/mMHz^b]	b [-]
Water**	1510	995	4.41e-10	0.2	2.00
Muscle	1580	1041	3.85e-10	57.0	1.01*
Fat	1430	928	5.27e-10	15.8	1.70
Skin	1537	1200	3.53e-10	104.0	1.01*
Gland	1510	1020	4.30e-10	75.0	1.50
Tumor	1550	1000	4.16e-10	57.0	1.30

3.4.1. VALIDATION WITH AN ANALYTICAL SOLUTION

To test the accuracy of the full-wave method, a configuration is used for which the analytical solution is known: a plane wave scattering off a spherical object. A derivation of the analytical solution can be found in the literature [66]. The acoustically penetrable sphere with radius $r = 2.5$ mm is positioned in the center of a volume of 10 mm × 10 mm × 10 mm. The spatial domain is discretized with a grid size $\Delta x = 0.078$ mm in each direction. The acoustic medium parameters of the sphere and the embedding are chosen similar to those typically encountered in biomedical applications. It is considered that the sphere represents fat and the embedding represents water, see Table 3.2. The sphere is illuminated with a plane wave propagating in the $+x$-direction. The Gaussian modulated wave has a center frequency $f_0 = 1$ MHz, and a bandwidth of 50 %. The time span of the simulation is set to 16 μs with a step size $\Delta t = 0.25$ μs. The iterative scheme is stopped when the normalized error is $\mathsf{Err_n} \leq 10^{-6}$. Time-domain results are obtained by applying inverse Fourier transforms.

Snapshots of the incident, total and scattered fields at time $t = 4.75$ μs in the plane $z = 0$ m are presented in Fig. 3.1. The normalized error between the analytical solution $\mathsf{P}_{\mathrm{AS}}(\boldsymbol{x}, t)$ and full-wave method $\mathsf{P}_{\mathrm{FW}}(\boldsymbol{x}, t)$ is calculated for the incident, total and scattered field, as

$$\mathsf{Error}(\boldsymbol{x}, t) = 20\log_{10}\left(\frac{|\mathsf{P}_{\mathrm{FW}}(\boldsymbol{x}, t) - \mathsf{P}_{\mathrm{AS}}(\boldsymbol{x}, t)|}{|\mathsf{P}_{\mathrm{AS}}(\boldsymbol{x}, t)|}\right), \tag{3.27}$$

where $|\ldots|$ indicates that the absolute value is taken. As can be seen in Fig. 3.1, the differences between both solutions are small, i.e. everywhere below −40 dB. For instance, the normalized error in the total field near the border of the sphere is around −45 dB and is mainly due to the spatial discretization of the sphere.

3.4.2. INVESTIGATING THE EFFECT OF DIFFERENT INHOMOGENEITIES

The presented full-wave method is used to investigate the effect of the different acoustic medium properties. For this study, a breast model built from an MRI scan of a real cancerous breast is used (see Fig. 3.2) [48]. The breast model is submerged in water and has acoustic medium parameters as shown in Table 3.2.

For the simulations, the time span considered equals 128 μs, and is discretized with a time step $\Delta t = 1$ μs. A point source, located in the point $(x_s, y_s, z_s) = (0\text{ m}, -0.05\text{ m}, 0\text{ m})$, generates a Gaussian modulated field with center frequency $f_0 = 0.25$ MHz and 50 % band-

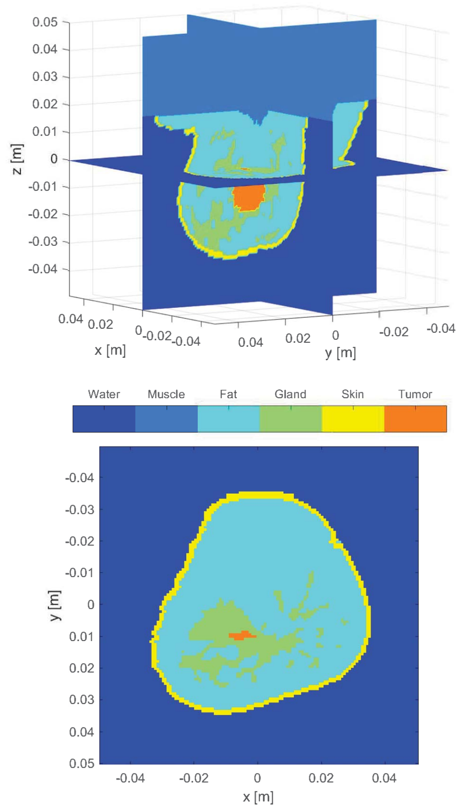

Figure 3.2: Tissue types for the 3-D breast model built from an MRI scan of a cancerous breast [48]. The bottom image displays a cross-section of the breast at $z = 0$ m. *The wave fields presented in Fig. 3.3 to 3.6 are taken in this cross-sectional plane.*

width. The spatial domain equals 0.1 m × 0.1 m × 0.1 m and is discretized with a uniform grid size $\Delta x = 0.78$ mm. The stopping criterion is set to $\mathrm{Err}_n \leq 10^{-6}$.

To investigate the effect of each acoustic medium property separately, the forward problem is solved five times; one simulation where all medium properties are set to their appropriate values, and four simulations where only one of the four medium properties has its appropriate value and where the remaining properties are set to values corresponding to the embedding (i.e. water). Fig. 3.3 shows the scattered pressure fields in the plane $z = 0$ m evaluated at four different frequencies (0.125 MHz, 0.25 MHz, 0.5 MHz and 1 MHz) and for the four medium properties separately and combined. The scattering caused by the different inhomogeneities are clearly visible. The images show that the amount of scattering increases for increasing frequency. In addition, it is shown that for these frequencies the amount of scattering caused by inhomogeneities in the compressibility and density is significantly larger than the scattering caused by inhomogeneities in the attenuation. The maximum values of the fields displayed in Fig. 3.3 are given in the Table 3.3. The

Table 3.3: Maximum values of the fields given in Fig. 3.3

	0.125 MHz [dB]	0.25 MHz [dB]	0.5 MHz [dB]	1 MHz [dB]
Compressibility	-21.1	-18.6	-16.7	-14.6
Density	-31.1	-25.8	-20.4	-15.2
Attenuation	-58.1	-52.1	-46.1	-39.7
Speed of Sound	-24.4	-21.5	-18.5	-14.9
All Inhomogeneities	-23.4	-20.8	-17.8	-15.2

amount of scattering with inhomogeneities in attenuation is 24 dB less for 1 MHz and for other frequencies nearly 30 dB. Moreover, the results obtained with speed of sound case shows strong similarities with the all inhomogeneities combined case. Finally, the ripples visible inside the breast are spaced roughly one wavelength apart. They are caused by interference of the field inside the breast, and can only be modeled via a full-wave method which allows for multiple scattering.

Next, time-domain wave fields are compared. Snapshots of the corresponding total wave fields for the five cases considered in Fig. 3.3 are displayed in Fig. 3.4. These time-domain results clearly show again that for low frequencies (e.g 0.25 MHz), variations in attenuation become so small that there is almost no effect on the wave field. There is even no visible scattering, focusing or phase shift caused by attenuation at these frequencies. Finally, similarities in the results for the speed of sound and all inhomogeneities combined cases are again clearly visible.

3.4.3. COMPARING THE SOLUTION METHODS

Finally, results obtained with different solution methods are compared. The same breast model is used for every method; it only considers inhomogeneities in the speed of sound. For the remaining results, the wave field has a center frequency of $f_0 = 0.5$ MHz and is discretised using a time step $\Delta t = 0.5$ μs and a grid size $\Delta x = 0.39$ mm. Snapshots of the total field in the plane $z = 0$ m and at time $t = 65$ μs for one emitter are presented in Fig. 3.5.

With Born approximation, first order scattering is included in the model but phase shifts and multiple scattering are neglected. The total amount of scattering is clearly less than for the full-wave method which includes multiple scattering. The wavefront of the field propagates at the same speed as the incident field because of the lacking of additional phase shifts (caused by a spatially varying speed of sound) in the model.

The paraxial approximation provides more accurate results than the Born approximation; phase shifts, refraction and diffraction effects are clearly visible in the resulting wave field. The multiple scattering inside the breast shows similarities with the scattering modeled with the full-wave method. However, they are very different in the backward direction due to the approximation applied.

The ray based method clearly only considers phase shifts. Scattering, refraction, diffraction and attenuation effects are not taken into account with this method.

A-scans of the transmission and reflection measurements are shown in Fig. 3.6 and Fig. 3.7 respectively. All A-scans are normalized with respect to the maximum of the incident field and interpolated by zero padding in the frequency domain.

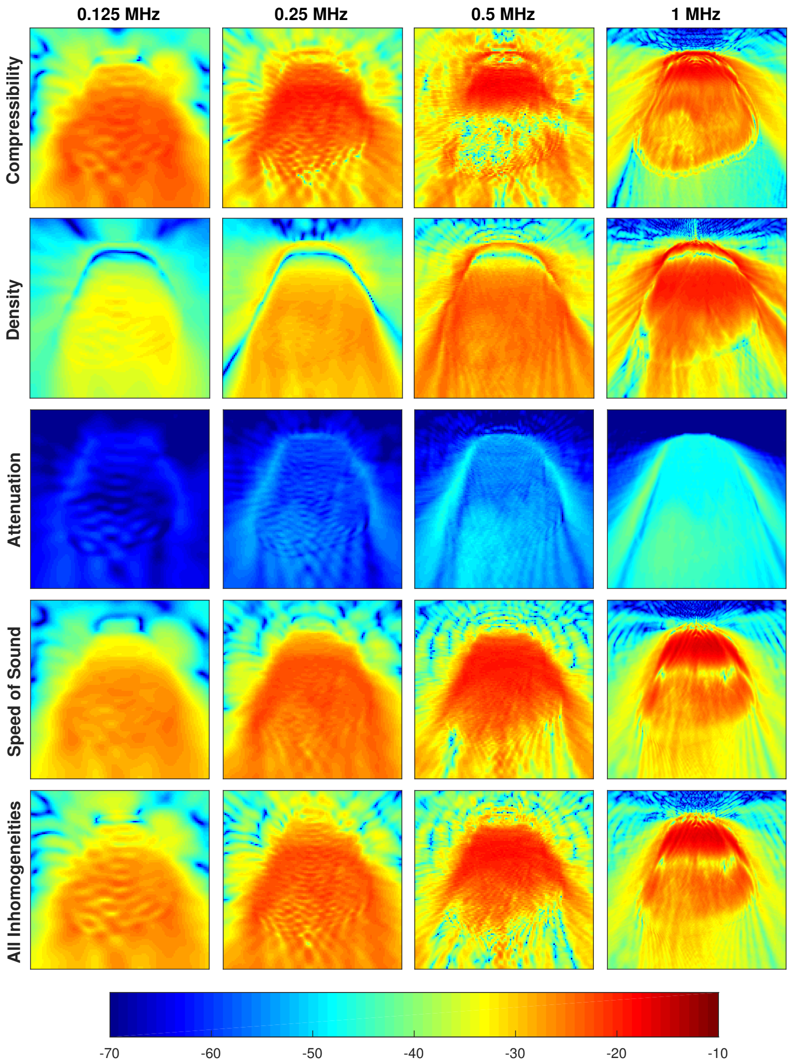

Figure 3.3: Frequency-domain results for the scattered pressure field in the plane $z = 0$ m *for different contrasts. The columns show results for different frequencies (from left to right* 0.125 MHz, 0.25 MHz, 0.5 MHz *and* 1 MHz*); the rows for different contrasts (from top to bottom compressibility, density, attenuation, speed of sound and all inhomogeneities combined).*

The A-scan retrieved from the full-wave solution and measured below the breast deviates significantly from the remaining three solutions, see Fig. 3.6 left column. The A-scan obtained within the Born approximation shows an incorrect arrival time of the wavefront and absence of scattering. For the paraxial solution the phase of the signal, especially for the waves arriving at a later time is erroneous. Although the arrival of the wavefront is

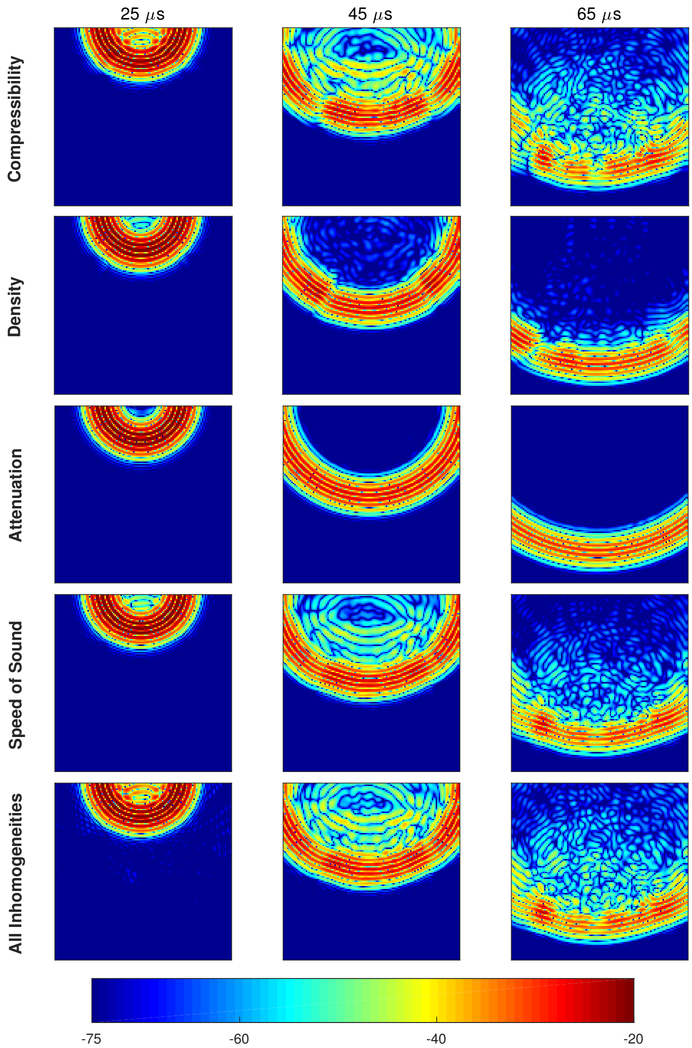

Figure 3.4: Snapshots of the total wave field obtained within the full-wave method in the plane $z = 0$ m *and at times* $t = 25\ \mu$s, $45\ \mu$s, $65\ \mu$s. *The rows show the total fields obtained for different contrast functions (from top to bottom compressibility, density, attenuation, speed of sound and all inhomogeneities combined).*

modeled reasonably well with the ray based method, significant phase shifts do occur in the tail of the main wave field and multiple scattering is completely absent. Only the spectral profile of paraxial approximation shows small similarity with the spectral profile of the full-wave method.

The A-scans measured on the right-hand side of the breast are also shown in Fig. 3.6. The most noticeable artifacts for the A-scan obtained using the Born approximation are

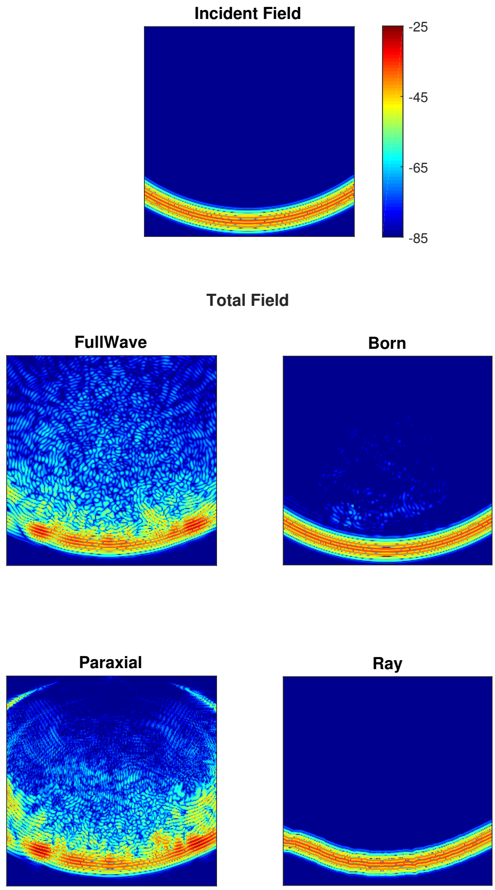

Figure 3.5: Snapshots of the total wave field in the plane $z = 0$ m *and at time* $t = 65$ μs. *Incident field placed at top and under that the total fields obtained for different methods (full-wave, parabolic, Born, and ray).*

the incorrect amplitude of the wavefront and the absence of multiple scattering. Next, as expected due to its approximation, errors in the phase and amplitude of the field are visible in the results corresponding to the paraxial approximation, especially for the scattered waves arriving after the main wave field. This confirms that the paraxial approximation is only valid within a limited opening angle. Finally, the ray based method shows many similarities with the Born approximation, in particular the absence of multiple scattering and an incorrect amplitude of the wave field. The three measured spectral profiles corresponding to the three approximations deviate significantly from the full-wave result.

The A-scan measured for the case when the receiver is placed close to the source for retrieving the reflections is shown in Fig. 3.7. Straight ray and paraxial approximation in their basic form, which is used in this work, neglect backscattering. Since a comparison is not valid, the result of full-wave method is given only. Strong reflections at the beginning

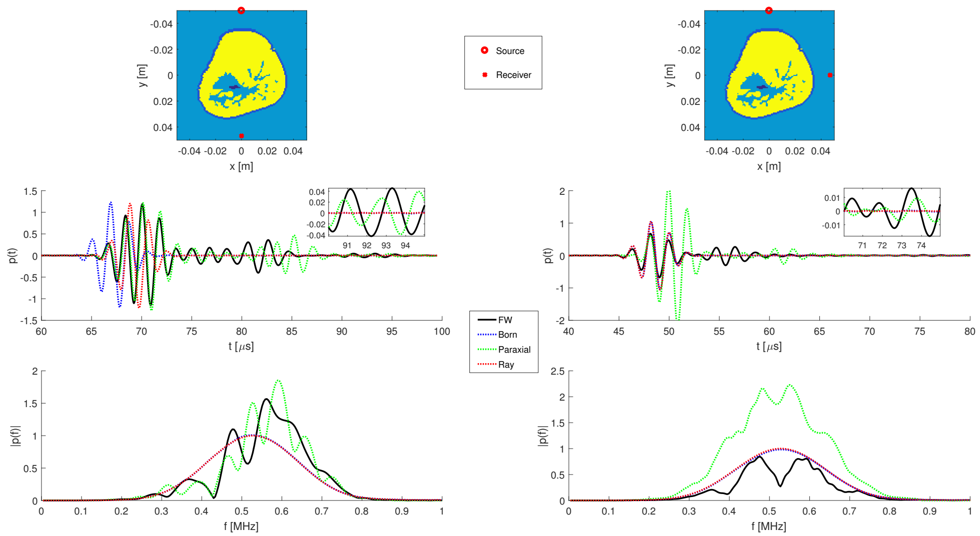

Figure 3.6: A-scans for the transmission measurements. The A-scans are normalized with respect to the incident field. The top row shows the position of the source and the receiver, the middle row shows the time-domain results, and the bottom row shows the frequency-domain results.

comes from the skin. Reflections that arrive later are mainly due to the inhomogeneities inside the breast.

3.5. CONCLUSION

A full-wave method based on a frequency-domain integral equation formulation is used to investigate to which extend spatial variations in the acoustic medium properties affect the acoustic pressure field in breasts. The same method is also used to validate the applicability of three solution methods commonly used to solve the forward problem for breast ultrasound.

The accuracy of the full-wave method, which is based on a frequency-domain integral-equation formulation, is confirmed using the analytical expression for a plane wave scattering off a soft spherical object. For the presented test with representative medium parameters, the error in the wave field is below -40 dB.

The effect of the heterogeneities belonging to the different medium properties are investigated separately and combined for the following frequencies: 0.125, 0.25, 0.5 and 1 MHz. The applied breast model is based on an MRI scan of cancerous breast and includes a spatially varying compressibility, density and attenuation. It is shown that the presented attenuation contrast causes significant less scattering (−24 dB) than the compressibility or density contrasts for frequencies below 1 MHz, suggesting that attenuation can be neglected for both the forward and inverse problem. The field scattering off the compressibility contrasts have a slightly higher amplitude than the field scattering off the density contrasts. Finally, the variations in the maximum amplitudes of the scattered

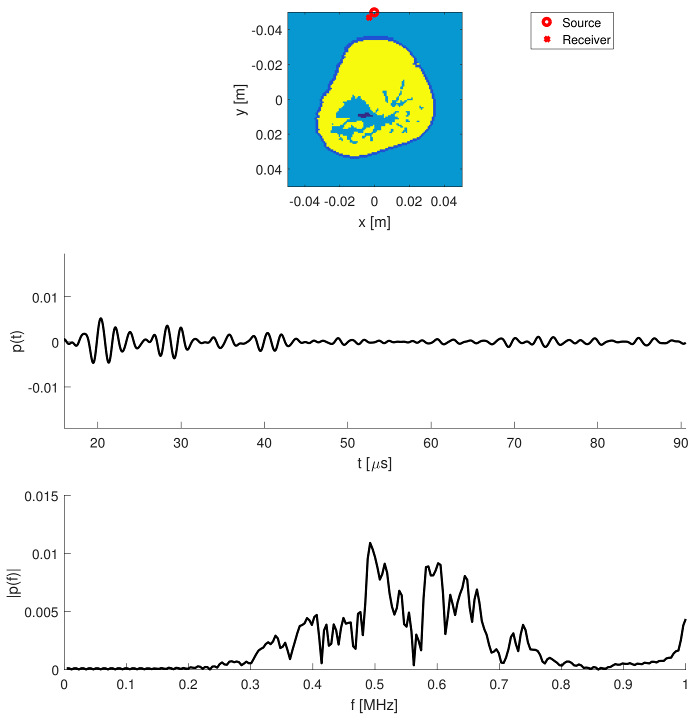

Figure 3.7: A-scan for the reflection measurements using full-wave method. The A-scan is normalized with respect to the incident field. The top figure shows the position of the source and the receiver, the middle figure shows the time-domain result, and the bottom figure shows the frequency-domain result.

fields corresponding to the speed of sound and all inhomogeneities included cases are 1 dB or less.

When comparing the excellent full-wave results with the results obtained using the Born approximation, paraxial approximation and ray based method, it is shown that the latter approximations have serious shortcomings. In general, the main problem with the Born approximation is that it is lacking phase shifts and multiple scattering. The paraxial approximation is more accurate than the Born approximation as phase shifts and focusing effects are modeled. Unfortunately, the paraxial method is only valid within a limited opening angle and backscattering is not included. Therefore the paraxial approximation could only be used with good results for transmission tomography, and has in this regime an order of magnitude lower complexity than full-wave approximation. The ray based method only considers phase shifts and neglects (back)scattering, refraction and diffraction effects. Consequently, the results from all three approximation methods are not accurate. This strongly limits its applicability for modeling breast ultrasound.

In conclusion, for frequencies below 1 MHz, scattering caused by attenuation can be neglected while both compressibility and density contrasts should be included in the model. In addition, considering only speed of sound variations in the medium is a valid approximation for these frequencies. Only the full-wave method yields accurate results, irrespective of the point of observation. The paraxial approximation may be considered as an alternative when the point of observation is located on the opposite side of the breast, as is the case for transmission tomography.

4

A Frequency-Hopping Technique for Solving the Cycle-Skipping Problem Encountered with Acoustic Full-Waveform Inversion[1]

Full-waveform inversion (FWI) methods are widely used for breast imaging to provide quantitative information about the tissues such as the speed of sound. FWI faces a cycle-skipping problem when applied to large contrasts or large spatial domains. This problem leads to erroneous image reconstructions. To overcome this problem, low frequency measurements or good starting models are needed. In this chapter, a frequency-hopping technique is proposed and tested for our FWI method (Contrast Source Inversion) to avoid the cycle-skipping problem. For a synthetic example, first, the effect of cycle skipping in the reconstructed image is shown. Next, it is shown for the same example that the implementation of the proposed frequency-hopping method solves this problem.

[1] This chapter has been published as:
Taskin and van Dongen, "A Frequency-Hopping Technique for Solving the Cycle-Skipping Problem Encountered with Acoustic Full-Waveform Inversion," IUS, IEEE, 2020.
The text and notation used in this chapter may differ on minor details from the actual publication. This is done to achieve consistency between chapters and will especially be the case for the section Theory.

4.1. INTRODUCTION

Ultrasound water-bath scanners are developed for breast cancer detection by various research groups [24], [27], [72]. With these systems tomographic scans of the breast are made. To obtain accurate quantitative information about the acoustic properties of the different breast lesions the measurements may be processed using full-waveform inversion (FWI) methods [31]. To reduce the computational costs for FWI, the inversion is performed in the frequency domain using a limited number of frequency components. However, high frequency components must be included during the inversion to obtain images with sufficient spatial resolution. Unfortunately, this may lead to a well-known problem referred to as cycle skipping [37]. Cycle skipping occurs when the time shift between the measured and modeled data is larger than half a wavelength divided by the speed of sound. This causes FWI to get locked into a local minima leading to the reconstruction of erroneous images. These large time shifts typically occur when large contrasts are present.

One solution to the cycle-skipping problem is to use low and high frequency components simultaneously during the inversion. Unfortunately, in practice this leads to an enormous computational load. Another solution is to use a good starting model (i.e. an initial speed-of-sound profile) for the FWI. With a good starting model, the differences in travel times between the modeled and measured wave fields are reduced. In this way, the cycle-skipping problem is avoided. However, it is not straightforward to generate a good starting model.

In this chapter, a frequency-hopping technique is proposed and tested for the FWI method Contrast Source Inversion (CSI) that reduces the cycle-skipping problems. The idea of the proposed technique is to start the inversion for the low frequency components only and use the resulting reconstruction (speed-of-sound profile) as a starting model when inverting for the higher frequency components. This procedure is repeated while increasing the frequency. In this way, the entire available bandwidth is used and high resolution speed-of-sound profiles are reconstructed without encountering the cycle-skipping problem.

4.2. THEORY

In this work CSI is used as a frequency domain FWI method [73]. The inversion procedure consist of minimizing the object and data equations which read

$$\hat{p}(\boldsymbol{x}) = \hat{p}^{\text{inc}}(\boldsymbol{x}) + \omega^2 \int_{\mathbb{D}} \hat{G}(|\boldsymbol{x}-\boldsymbol{x}'|)\,\hat{w}(\boldsymbol{x}')\,dA(\boldsymbol{x}'), \quad \boldsymbol{x} \in \mathbb{D}, \tag{4.1}$$

and

$$\hat{p}^{\text{sct}}(\boldsymbol{x}) = \omega^2 \int_{\mathbb{D}} \hat{G}(|\boldsymbol{x}-\boldsymbol{x}'|)\,\hat{w}(\boldsymbol{x}')\,dA(\boldsymbol{x}'), \quad \boldsymbol{x} \in \mathbb{S}, \tag{4.2}$$

where $\hat{p}(\boldsymbol{x})$, $\hat{p}^{\text{inc}}(\boldsymbol{x})$, and $\hat{p}^{\text{sct}}(\boldsymbol{x})$ are the total, incident and scattered pressure fields respectively. The vector $\boldsymbol{x}$ denotes a position in $\mathbb{R}^2$. $\mathbb{D}$ is the spatial domain that includes the object and that is enclosed by the boundary $\mathbb{S}$. ω is the angular frequency. $\hat{G}(|\boldsymbol{x}-\boldsymbol{x}'|)$ is the Green's function for the homogeneous embedding. $\hat{w}(\boldsymbol{x}')$ is the contrast source that is defined as

$$\hat{w}(\boldsymbol{x}') = \chi(\boldsymbol{x}')\,\hat{p}(\boldsymbol{x}'), \tag{4.3}$$

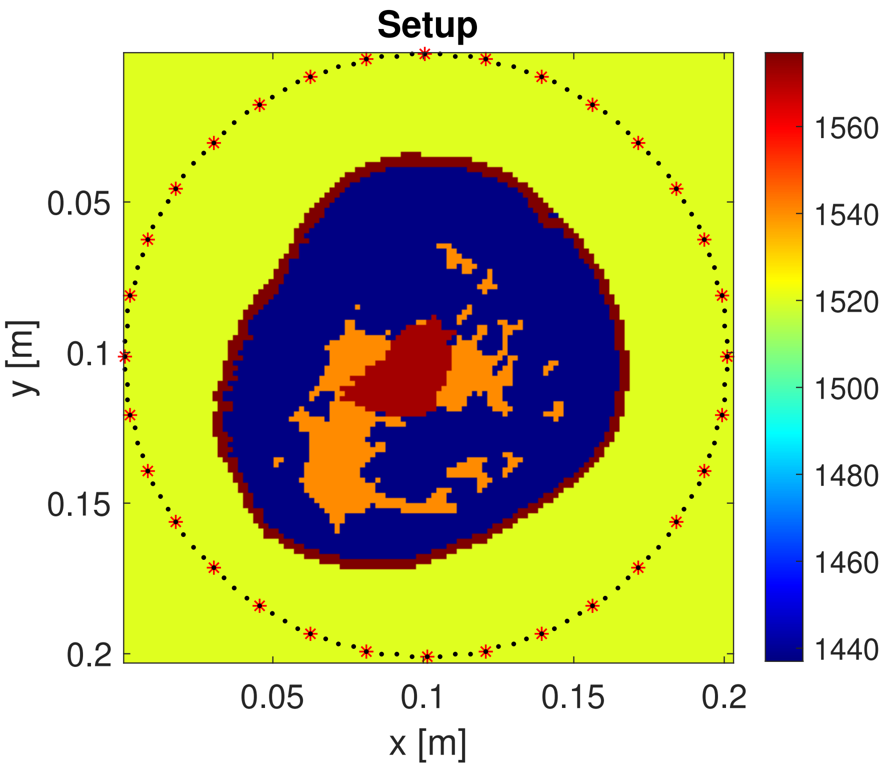

Figure 4.1: System setup. The target (synthetic breast phantom) is surrounded with sources (red asterisk) and receivers (black dot).

where $\chi(\boldsymbol{x}')$ is the contrast function that reads

$$\chi(\boldsymbol{x}') = \frac{1}{c^2(\boldsymbol{x}')} - \frac{1}{c_0^2}, \tag{4.4}$$

where $c(\boldsymbol{x}')$ and c_0 are the speed of sound of the medium and the homogeneous embedding respectively. Note that, it is assumed that density $\rho(\boldsymbol{x}')$ is constant in the whole medium.

With CSI, the unknown contrast source is updated using an iterative scheme that minimizes the cost function E that equals

$$E = \eta_{\mathbb{S}} \| \hat{p}^{\mathrm{sct}} - \mathrm{L}^{\mathbb{S}}[\hat{w}] \|_{\mathbb{S}}^2 + \eta_{\mathbb{D}} \| \chi \hat{p}^{\mathrm{inc}} - w + \chi \mathrm{L}^{\mathbb{D}}[\hat{w}] \|_{\mathbb{D}}^2, \tag{4.5}$$

where $\eta_{\mathbb{S}}$ and $\eta_{\mathbb{D}}$ are normalization terms, and where $\mathrm{L}^{\mathbb{D}}$ and $\mathrm{L}^{\mathbb{S}}$ are integral operators derived from equations (4.1) and (4.2), respectively.

In the conventional implementation of CSI the cost function E is minimized for a limited number of frequency components simultaneously. That might be problematic when the cycle skipping for the higher frequency components is dominating the inversion process. With the frequency hopping implemented, CSI is started with the lowest frequency

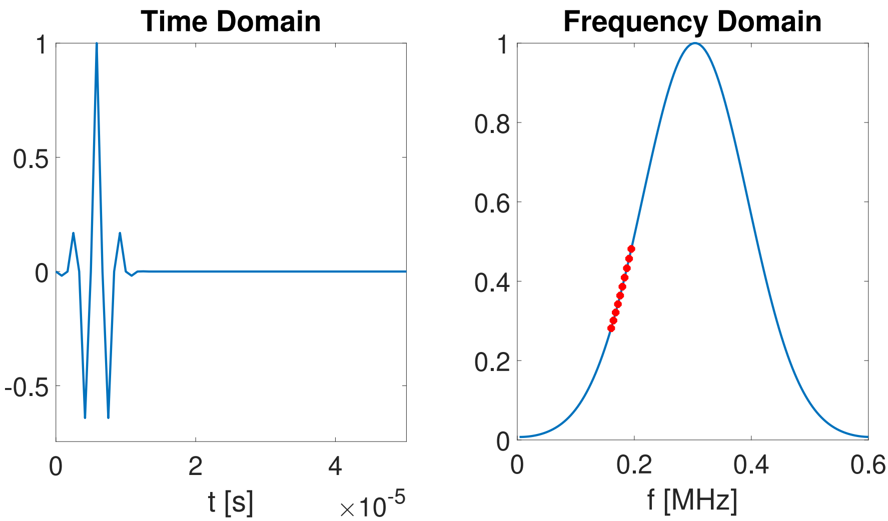

Figure 4.2: Source wavelet in time (left) and frequency (right) domain. The red dots indicate the frequency components used for inversion.

component only. The reconstructed contrast source term for this frequency component inversion is successively used as a starting model for the next frequency component. Continuing this way, all the selected frequency components are used for the inversion sequentially. Having already a good starting model for the higher frequency components helps to avoid cycle skipping to occur. In this way high resolution reconstructions may be obtained.

4.3. RESULTS

A synthetic example is used to show FWI results when cycle skipping occurs and how the implementation of frequency hopping overcomes this problem. A breast mimicking synthetic phantom is used [48], see Fig. 4.1. There are 32 sources and 128 receivers distributed equally on a circle enclosing the phantom [74]. The circle has a radius of 0.2 m.

A Gaussian modulated pulse with 0.3 MHz center frequency is used as a source wavelet, see Fig. 4.2. The frequency components used for inversion are indicated by the red dots. In total there are ten frequencies within the range 0.16 - 0.19 MHz. Synthetic measurement data is computed by solving the full forward problem using a steepest descent scheme [75]. Given the low frequencies used, attenuation is neglected [75].

Fig. 4.3 shows the reconstruction results of CSI. These results are obtained after 128 iterations using only ten frequency components with CSI. When CSI is implemented in the conventional way by inverting for all ten frequency components simultaneously, the resulting reconstructed speed-of-sound profile is not accurate. That's because the higher frequency components face the cycle-skipping problem and CSI remains in a local minima. However, when frequency hopping is implemented for CSI, an accurate speed-of-sound profile is obtained. These results show that cycle skipping is a serious problem for

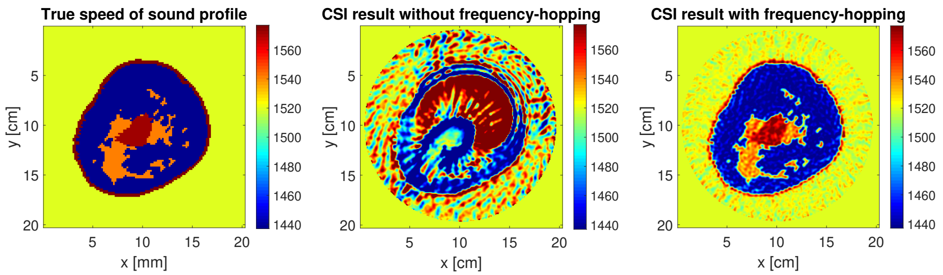

Figure 4.3: Contrast source inversion (CSI) results: true speed-of-sound profile (left), CSI results without (middle) and with (right) frequency hopping is employed.

FWI. However, with frequency hopping implemented this problem can be solved.

To explain the results obtained in Fig. 4.3, CSI results for each individual frequency component is computed and shown in the first column of Fig. 4.4. These results show that for the first five frequency components accurate reconstructions are obtained. However, starting from the sixth frequency component erroneous results are obtained, as at the sixth frequency component the cycle-skipping problem starts. These results explain the erroneous image in Fig. 4.3. In this example, cycle skipping can be avoided by using only the frequency components that are below the sixth frequency component. However, in that case the valuable information that is included in the higher frequency components would be missed. These components are essential to reconstruct profiles with high spatial resolution. Additionally, using all the frequency components in the selected bandwidth simultaneously wouldn't help much since most of the components face the cycle-skipping problem. In addition, this approach will lead to large computational loads.

Reconstruction results for each step in the frequency-hopping approach are shown in the second column of Fig. 4.4. These results are again single frequency reconstructions but now with frequency hopping implemented. It can be seen from these results that the cycle skipping that otherwise would have started at the sixth frequency component is not taking place here. The starting model that is obtained from inversion using the previous frequencies is already accurate enough to avoid the cycle skipping. Moreover, this procedure could be continued over the entire available bandwidth without facing cycle skipping. Increasing the employed bandwidth will lead to an improved reconstruction. Note that, the starting frequency has significant importance. If the starting frequency component is high and cycle skipping occurs at the beginning, it will be difficult to overcome that problem even with the frequency hopping implemented or by using regularization [76].

4.4. CONCLUSION

In conclusion, a frequency-hopping technique is developed to solve the cycle-skipping problem. The proposed method is successfully tested for contrast source inversion (CSI) as an example of frequency-domain FWI for breast imaging. With the proposed method, high frequency components are successfully included in the FWI to obtain accurate high-resolution reconstructions.

The frequency-hopping approach is tested for CSI. Results show that when CSI is em-

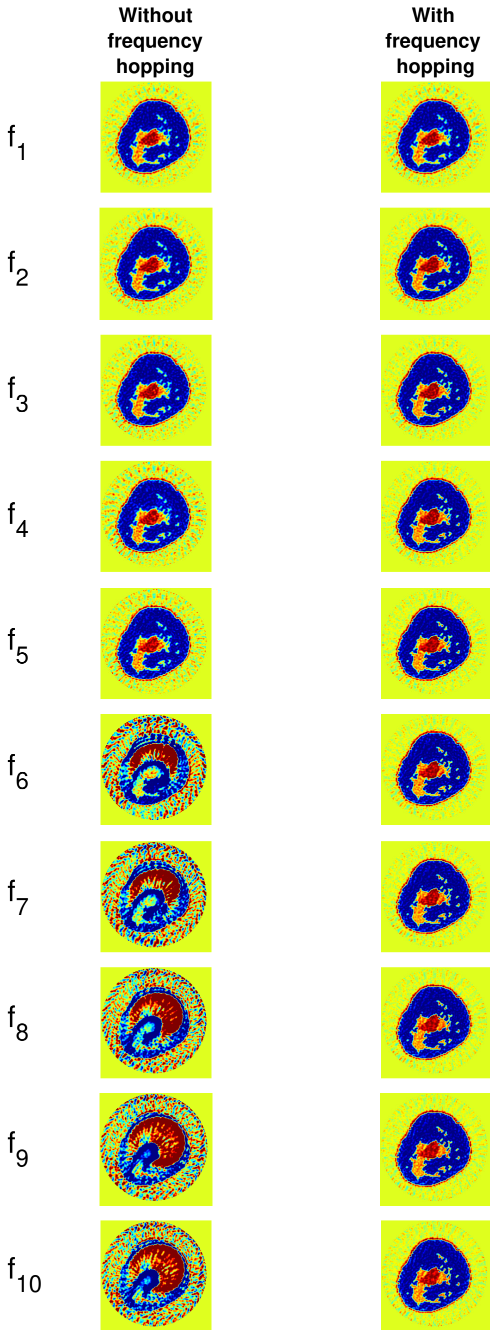

Figure 4.4: Contrast source inversion (CSI) results for each individual frequency component without (left column) and with (right column) frequency hopping applied.

ployed using all available frequency components simultaneously, it gives rise to the reconstruction of an erroneous image. When the presented frequency-hopping approach is employed, the problem of cycle skipping is successfully avoided, and an accurate reconstruction is obtained without any loss of spatial resolution.

5

REDATUMING OF 2-D WAVEFIELDS MEASURED ON AN ARBITRARY-SHAPED CLOSED APERTURE [1]

Whole breast ultrasound scanning systems are used to screen a women's breast for suspicious lesions. Typically, the transducers are located at fixed positions at relatively large distances from the breast to avoid any contact with the breast. Unfortunately, these large distances give rise to large spatial domains to be imaged. These large domains hamper the applicability of imaging by inversion. To reduce the size of the spatial computational domain, we present a two-dimensional redatuming method based on Hankel decomposition of the measured field. With this method, the field measured over an arbitrary-shaped closed curve can be redatumed to a new curve enclosing a smaller spatial domain. Additional advantages of the proposed method are that it allows to account for the finite size and orientation of a transducer and that it is robust to noise. The proposed method is successfully validated using synthetic and measured data and the results show that the recorded field can be redatumed to any position in the embedding.

[1] This chapter has been published as:
Taskin et al., "Redatuming of 2-D Wave Fields Measured on an Arbitrary-Shaped Closed Aperture," IEEE T. Ultrason Ferr. 67(1), 2020.
The text and notation used in this chapter may differ on minor details from the actual publication. This is done to achieve consistency between chapters and will especially be the case for the section Theory.

5.1. INTRODUCTION

Ultrasound is gaining interest as a modality for breast cancer detection. It has the advantage over conventional x-ray mammography that it has the capability to detect tumours in dense breasts and that it is a patient-friendly and safe imaging modality [26], [77]. Recent work on whole breast ultrasound focuses on water bath scanning systems [24], [27], [72]. As compared to hand-held systems, water bath scanning systems have the advantage that they are operator independent and need less scanning time. In addition, they provide transmission measurements together with reflection measurements by scanning the breast from all sides.

5

Recently, full-waveform inversion (FWI) methods are gaining attention as they have a potential to characterize the different tissues accurately using the reconstructed medium parameters [31], [38], [78]. These methods work especially well in case both reflection and through transmission measurements are available. However, FWI poses some challenges when applied in practice. First, FWI is computationally expensive. Several attempts have been made to overcome this problem, varying from source encoding [79] to the application of special accelerating and memory techniques [80].

To address the computational costs of FWI in geophysics, a method referred to as redatuming is commonly used [81]–[84]. With this method the wave field is back-propagated from the plane where the measurements are made to a plane near the region of interest. In this way, a reduction of the computational domain and hence costs is achieved. The main approach in seismic is to redatum the measurement from one planar domain to another by using the Rayleigh II integral [55]. Since the measurement geometry is typically not planar for whole breast ultrasound, an alternative approach is needed. A continuation method is used for a similar problem faced with electromagnetic inversion for arbitrary surfaces [85].

In general, to extrapolate fields from a closed surface to another surface Green's second identity can be used. However, that requires the normal derivative of the pressure field along a closed surface. To overcome this problem the main approach is to find a Green's function that vanishes on the measurement surface [86], [87]. Since it is not easy to compute the required Green's function with Dirichlet boundary conditions, extrapolation from an arbitrary-shaped surface is not straightforward. Therefore, we use a different approach in this work. To account for an arbitrary shaped scanning setup, we propose Hankel function decomposition of the measured field to redatum the measurements to any location in the homogeneous background. The Hankel function is among the possible solutions of the two-dimensional (2-D) wave equation in cylindrical coordinates [88].

The organization of the chapter is as follows. In section 5.2, we start with a derivation of the theory behind the proposed redatuming method. Although the theory is derived for lossless media, it can be derived for a lossy media using the same approach. Next, we provide a method to account for the finite size of the receivers. In section 5.3, we validate our method by showing results obtained with simulated data. In addition, we present reconstructions from real data before and after redatuming. In section 5.4, we discuss some details of the proposed method. Section 5.5 includes our concluding remarks.

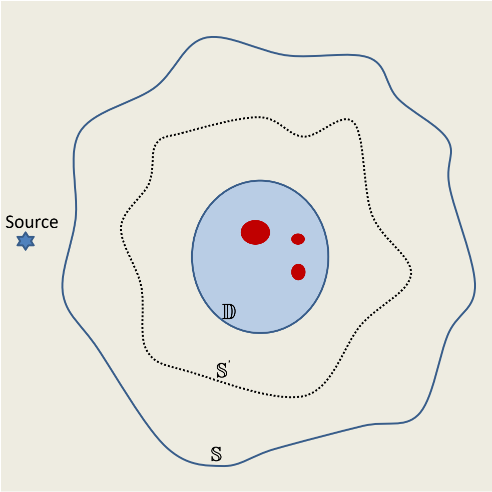

Figure 5.1: Schematic representation of the setup. The source is located outside the receiver ring $\mathbb{S}$ enclosing our domain of interest $\mathbb{D}$. The measured wave field is redatumed from $\mathbb{S}$ to $\mathbb{S}'$.

5

5.2. THEORY

Consider the 2-D scanning geometry depicted in Fig. 5.1. Here, the closed curves $\mathbb{S}$ and $\mathbb{S}'$ enclose the spatial domain $\mathbb{D}$. The curves $\mathbb{S}$ and $\mathbb{S}'$ are located in the homogeneous lossless embedding with constant speed of sound c. Contrasts in the acoustic medium parameters are only present in the spatial domain $\mathbb{D}$. A position in the spatial domain $\mathbb{R}^2$ is denoted in Cartesian coordinates by the vector (x, y) and in polar coordinates by the vector (r,ϕ), with $(x, y) = (r\cos(\phi), r\sin(\phi))$. Note that the origin lies inside $\mathbb{S}$ and $\mathbb{S}'$. All formulations are done in the temporal Fourier domain with angular frequency ω.

5.2.1. REDATUMING TOWARDS OBJECT OF INTEREST

The pressure field $\hat{p}(r,\phi,\omega)$ measured in $\mathbb{S}$ satisfies the 2-D Helmholtz equation, which reads in polar coordinates

$$r^2\frac{\partial^2\hat{p}(r,\phi,\omega)}{\partial r^2}+r\frac{\partial\hat{p}(r,\phi,\omega)}{\partial r}+\frac{\partial^2\hat{p}(r,\phi,\omega)}{\partial\phi^2}+r^2\frac{\omega^2}{c^2}\hat{p}(r,\phi,\omega)=0. \tag{5.1}$$

This equation can be solved using the separation of variables method by separating the pressure field $\hat{p}(r,\phi,\omega)$ in a radial and an angular part, hence

$$\hat{p}(r,\phi,\omega)=\hat{\Gamma}(r,\omega)\,\Phi(\phi). \tag{5.2}$$

Substituting equation (5.2) into (5.1) yields separate equations for $\hat{\Gamma}(r,\omega)$ and $\Phi(\phi)$, namely

$$\frac{1}{\hat{\Gamma}(r,\omega)}\left[r^2\frac{\partial^2\hat{\Gamma}(r,\omega)}{\partial r^2}+r\frac{\partial\hat{\Gamma}(r,\omega)}{\partial r}+r^2\frac{\omega^2}{c^2}\hat{\Gamma}(r,\omega)\right]=\mu^2, \tag{5.3}$$

and

$$\frac{1}{\Phi(\phi)}\frac{\partial^2\Phi(\phi)}{\partial\phi^2} = -\mu^2, \tag{5.4}$$

with μ a constant. Equation (5.4) is a standard second-order differential equation whose solution equals

$$\Phi(\phi) = ae^{i\mu\phi}, \tag{5.5}$$

with arbitrary constant a and $-\pi < \phi \leq \pi$. To satisfy the boundary condition $\Phi(\pi) = \Phi(-\pi)$, μ needs to be an integer. This requirement limits the possible solutions for $\Phi(\phi)$ to

$$\Phi_n(\phi) = a_n e^{in\phi}, \tag{5.6}$$

with $n \in \mathbb{Z}$. Under this condition equation (5.3) becomes

5

$$r^2\frac{\partial^2\hat{\Gamma}(r,\omega)}{\partial r^2} + r\frac{\partial\hat{\Gamma}(r,\omega)}{\partial r} + \left(r^2\frac{\omega^2}{c^2} - n^2\right)\hat{\Gamma}(r,\omega) = 0. \tag{5.7}$$

Equation (5.7) is known as Bessel's differential equation and has as solution

$$\hat{\Gamma}_n(r,\omega) = \hat{b}_{n,1}(\omega)\hat{H}_n^{(1)}\left(\frac{\omega}{c}r\right) + \hat{b}_{n,2}(\omega)\hat{H}_n^{(2)}\left(\frac{\omega}{c}r\right), \tag{5.8}$$

where the Hankel functions $\hat{H}_n^{(1)}\left(\frac{\omega}{c}r\right)$ and $\hat{H}_n^{(2)}\left(\frac{\omega}{c}r\right)$ represent inward and outward propagating cylindrical waves, respectively. By placing the origin of our coordinate system inside $\mathbb{S}$ and $\mathbb{S}'$ we know that the scattered field is only described by outward propagating waves. Consequently, all coefficients $\hat{b}_{n,1}(\omega)$ are equal to zero. By combining equations (5.2), (5.6), (5.8) and the condition $\hat{b}_{n,1}(\omega) = 0$, the solutions of equation (5.1) for each n are, up to a constant, equal to

$$\hat{p}_n(r,\phi,\omega) = \hat{\Gamma}_n(r,\omega)\Phi_n(\phi) = \hat{H}_n^{(2)}\left(\frac{\omega}{c}r\right)e^{in\phi}. \tag{5.9}$$

The final solution is obtained by taking a linear combination of the solutions given in (5.9), hence

$$\hat{p}(r,\phi,\omega) = \sum_{n=-N}^{N}\hat{c}_n(\omega)\hat{H}_n^{(2)}\left(\frac{\omega}{c}r\right)e^{in\phi}. \tag{5.10}$$

To find the complex valued coefficients $\hat{c}_n(\omega)$ of equation (5.10), the pressure field $\hat{p}(r,\phi,\omega)$ is matched to the M measurements $\hat{d}_m(\omega)$, where $\hat{d}_m(\omega)$ is the field measured by the m^{th} receiver located on $\mathbb{S}$. Consequently, the unknown coefficients $\hat{c}_n(\omega)$ are obtained by solving the following system of equations

$$\sum_{n=-N}^{N}\hat{c}_n(\omega)\hat{H}_n^{(2)}\left(\frac{\omega}{c}r_m\right)e^{in\phi_m} = \hat{d}_m(\omega), \tag{5.11}$$

for all m. Rewriting equation (5.11) in matrix-vector notation gives

$$\begin{bmatrix} \hat{H}^{(2)}_{-N}\left(\frac{\omega}{c}r_1\right)e^{-iN\phi_1} & \cdots & \hat{H}^{(2)}_{N}\left(\frac{\omega}{c}r_1\right)e^{iN\phi_1} \\ \vdots & \ddots & \vdots \\ \hat{H}^{(2)}_{-N}\left(\frac{\omega}{c}r_M\right)e^{-iN\phi_M} & \cdots & \hat{H}^{(2)}_{N}\left(\frac{\omega}{c}r_M\right)e^{iN\phi_M} \end{bmatrix} \times \begin{bmatrix} \hat{c}_{-N}(\omega) \\ \vdots \\ \hat{c}_N(\omega) \end{bmatrix} = \begin{bmatrix} \hat{d}_1(\omega) \\ \vdots \\ \hat{d}_M(\omega) \end{bmatrix} \tag{5.12}$$

or, in shorthand notation,

$$\underline{\underline{Q}}\,\underline{c} = \underline{d}, \tag{5.13}$$

with $\underline{\underline{Q}}$ a $(M)\times(2N+1)$ matrix with elements $Q_{m,n} = \hat{H}^{(2)}_n\left(\frac{\omega}{c}r_m\right)e^{in\phi_m}$, $\underline{c}$ a vector of length $(2N+1)$ with elements $\hat{c}_n(\omega)$, and $\underline{d}$ a vector of length M with elements $\hat{d}_m(\omega)$. For the convergence, sufficient number of data points (M) need to be provided to compute the $(2N+1)$ coefficients for the Hankel functions. In this work, we use Tikhonov regularization to find the coefficients $\hat{c}_n(\omega)$, consequently

$$\underline{c} = (\underline{\underline{Q}}^{\dagger}\,\underline{\underline{Q}} + \alpha I)^{-1}\underline{\underline{Q}}^{\dagger}\,\underline{d}, \tag{5.14}$$

where I is a unit matrix, α is a regularization parameter, and $\underline{\underline{Q}}^{\dagger}$ denotes the adjoint of $\underline{\underline{\mathrm{Q}}}$.

Once the coefficients $\hat{c}_n(\omega)$ are found, the field can be computed at any location outside $\mathbb{D}$ using equation (5.10). In this way, we can redatum the wave field measured at $\mathbb{S}$ to the domain $\mathbb{S}'$. Although redatuming is explained for the receiver side using the outward propagating field, it is also possible to apply the same procedure for the source side by using the inward propagating field. Finally, for an accurate reconstruction of the wave field it is important to satisfy the sampling criterion as this defines the number of coefficients needed to describe the wave field [89].

5.2.2. APPLICATION OF FINITE-SIZED RECEIVER

For the receiver it is important to account for its size and orientation. The field measured with a finite-sized receiver of aperture length L, can be written as an integral over its active curve of length $2r_m\theta$. It is assumed here that, the receiver ring $\mathbb{S}$ is a circle centered at the origin. Consequently, for transducers oriented towards the origin the measurement $\hat{d}_m(\omega)$ equals

$$\hat{d}_m(\omega) = \hat{d}(r_m,\phi_m,\omega) = \int_{-\theta}^{+\theta} \hat{p}(r_m,\phi_m+\phi')\,d\phi'. \tag{5.15}$$

When we combine equations (5.10) and (5.15) and alter the order of integration, it follows that

$$\hat{d}_m(\omega) = \sum_{n=-N}^{N} \hat{c}_n(\omega)\,T_n\hat{H}^{(1)}_n\left(\frac{\omega}{c}r_m\right)e^{in\phi_m}, \tag{5.16}$$

5

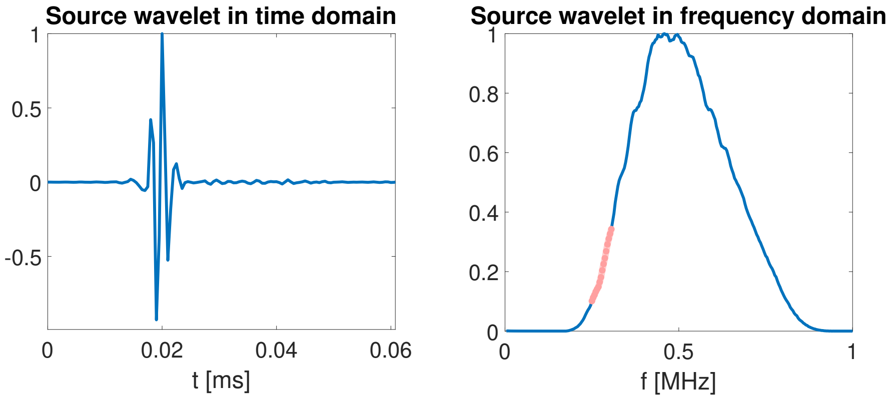

Figure 5.2: Normalized source excitation profile in time (left) and frequency (right) domain. The red dots show the frequency range used for inversion.

5

where the finite size of the transducer is accounted for via the constant T_n

$$T_n = \int_{-\theta}^{+\theta} e^{in\phi'} \, d\phi'. \tag{5.17}$$

5.3. RESULTS

The proposed method is tested on synthetic and experimental data. To show its practical applicability, we present an example where we apply contrast source inversion (CSI) [73] on measured data before and after redatuming.

5.3.1. SYNTHETIC EXAMPLE

CONFIGURATION

A full-wave method based on a frequency-domain integral equation formulation is used to solve the forward problem [90], [91]. A source is located at $(x_s, y_s) = (0.248\ \text{m}, 0.035\ \text{m})$ and generates a Gaussian modulated pressure field with 0.5 MHz central frequency. The source's excitation profile is shown in Fig. 5.2. In total 450 receivers are used to measure the scattered field. The time span of the simulation is set to 268 µs with a step size $\Delta t = 0.5$ µs. The spatial domain equals 0.1 m × 0.1 m and is discretized with a uniform grid size $\Delta x = 0.5$ mm. The grid size corresponds to six points per wavelength at central frequency. A rectangular object (0.02 m × 0.05 m) is placed at the center. The speed of sound of the background medium is 1490 m/s and of the object 1547 m/s. The background medium and the object have the same mass density $\rho = 1000$ kg/m^3 and are both lossless.

SYNTHETIC RESULTS

First, we consider the case where the field measured with a circular array is redatumed, see Fig. 5.3. For this purpose, the simulated pressure field is measured at $r = 0.09$ m using 450 point receivers and reconstructed using Hankel functions, see Fig. 5.3 first row. Then, the measured field at $r = 0.09$ m (blue circle) is redatumed to $r = 0.05$ m (red circle). The

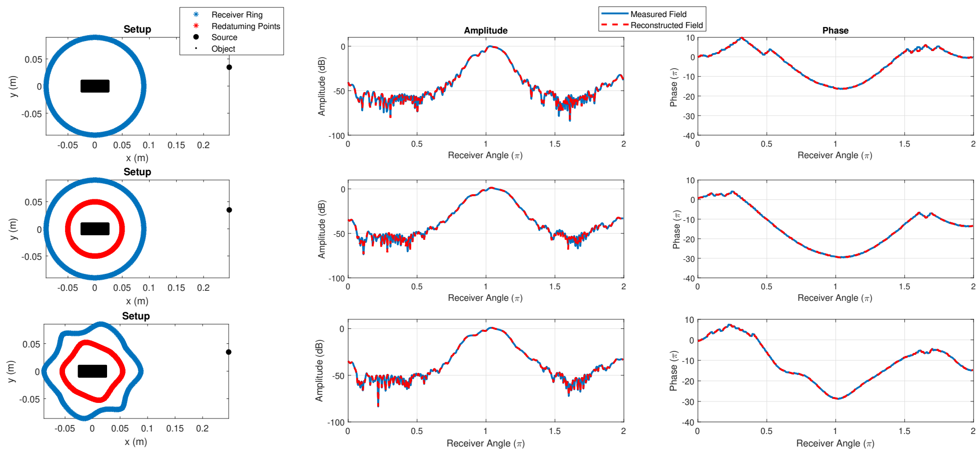

Figure 5.3: Single frequency (0.5 MHz) results using point receivers. The setups are given in the first column. The first row shows the synthetically measured and reconstructed pressure fields at the blue surface. The second and third rows show the synthetically measured and redatumed pressure field at the red surface. The redatumed field is computed from the measurements at the blue surface.

redatumed and modelled fields at the red circle are shown in Fig. 5.3 second row. The amplitudes of both fields are normalized by the same constant. These single frequency results clearly show that both the amplitude and the phase of the fields match each other perfectly. Finally, the performance of the proposed method is tested using an arbitrary shaped scanning setup. The third row of Fig. 5.3 shows the results for redatuming from one arbitrary surface to another. These results agree with the observation that the proposed method does not depend on the applied configuration, as long as the field is measured along a closed curve. Note that, we use $M = 450$ number of data points and $2N + 1 = 211$ coefficients for these experiments.

To examine the similarities between the measured and reconstructed wavefield for all frequency components, time domain results are shown in Fig. 5.4 and 5.5. Fig. 5.4 shows the measurements at five receiver locations at the transmission side; Fig. 5.5 at the reflection side. Note that all fields are normalized using the same constant.

Second, to examine the robustness of the proposed method, the results of a noisy experiment is shown in Fig. 5.6. White noise with an amplitude equal to 7.5% of the maximum amplitude of the recorded data set is added to the measured signal. A noise-free measurement is plotted together with a noisy measurement in the second graph and with reconstructed field form the noisy measurement in the third graph in Fig. 5.6. For the noisy measurement, the signal to noise ratio (SNR) equals 7.1 dB. The reconstructed field from this noisy measurement has an SNR = 10.3 dB. It is concluded from both these values and the results shown in Fig. 5.6 that with the proposed method the noise in the measurement is slightly suppressed. This is due to the fact that projecting the measurement on the Hankel functions filters out some noise. Careful analysis of denoising by Hankel decomposition is beyond the scope of this work but initial results show some potential. To

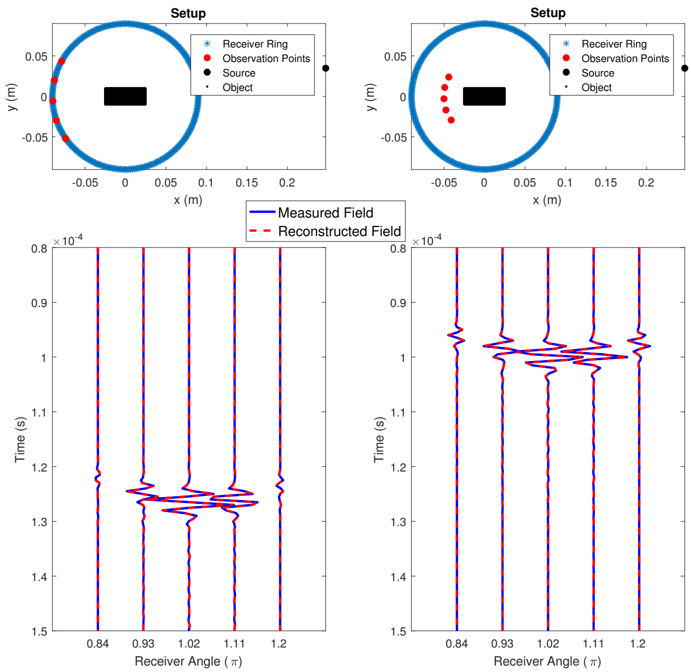

Figure 5.4: Time domain results for transmission measurements using point receivers. The setup is shown in the first row; the source (black dot) is on the right of the original receiver array (blue dots) and the redatumed locations (red dots). A-scans of the measured (blue) and reconstructed (red) wave fields are shown in the second row; (left) with the redatumed locations coinciding the original receiver locations and (right) positioned inside the receiver ring.

exploit this aspect further, one can apply inversion using an l_1-solver [92].

Finally, accounting for a finite-sized receiver is investigated. In particular, we test for receivers with an active aperture of length $L = \lambda, 2\lambda$, and 4λ. The pressure fields measured with these finite-sized receivers at $r = 0.09$ m are given in Fig. 5.7 together with the reconstructed fields. Reconstructed and measured fields are matching each other perfectly when the signal is above -40 dB. Differences in phase and amplitude occur when the amplitude of the signal is below -40 dB. This is due to the fact that the same fixed number of coefficients $c_n(\omega)$ are used to reconstruct the fields. The areas where the signal amplitude is above -40 dB are highlighted with a red square.

5.3.2. EXPERIMENTAL EXAMPLE

CONFIGURATION

The Delft Breast Ultrasound Scanner (DBUS) is used to validate our method using measured data [93]. This system has a configuration similar to the one used for the synthetic examples. A source located at $r = 0.25$ m operates at 0.5 MHz central frequency. The circular receiver array has a radius of 0.1 m. A complete measurement covers 45 source and

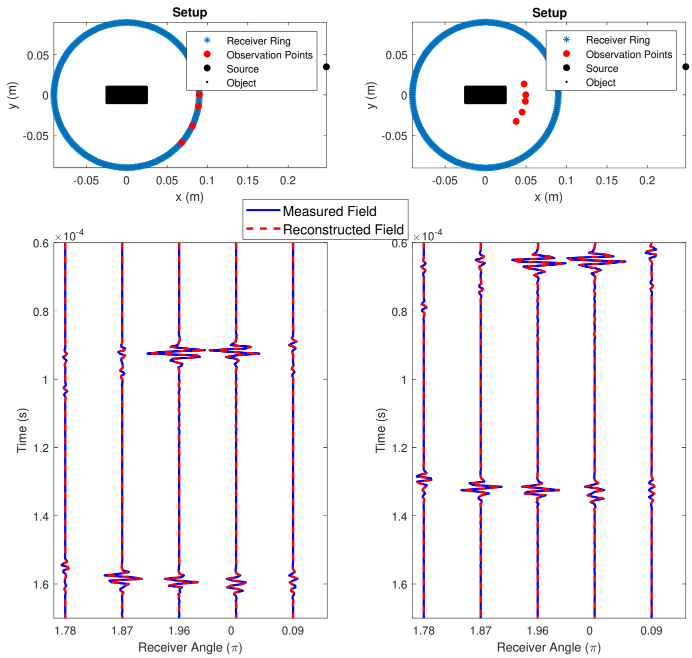

Figure 5.5: Same as Fig. 5.4, but now for reflection measurements.

450 receiver locations. The object is a rectangular agar phantom containing two copper threads and one plastic straw. A sketch of the system together with a reconstruction of the phantom using Synthetic Aperture Focusing Technique (SAFT) [94] is shown in Fig. 5.8.

EXPERIMENTAL RESULTS

CSI is applied to the data from the DBUS system [31], [73], [76]. Five frequency components between 0.25 MHz and 0.3 MHz are used for the inversion. Reconstruction result after 128 iterations without applying redatuming is shown in the first row of Fig. 5.9. The second row shows the result after redatuming the data to the circular receiver array with radius $r = 0.05$ m. The results are highly similar. The small variations visible are mainly caused by the misfit between the actual locations of the receivers and the grid points in the computational domain. With the help of redatuming, it is possible to let the receiver locations coincide exactly with the grid points of the computational domain. After redatuming, the resulting spatial domain has become four times smaller; only 204×204 pixels out of the original 406×406 pixels are preserved.

Reducing the size of the spatial domain allows us to increase the number of frequency components for the inversion without affecting the total computational load. The gain in performance is clearly visible in the third row of Fig. 5.9, where we increase the number of frequency components from 5 to 20. The computation time for this latter case is the same as for the original case using four components only (neglecting the time spent on redatuming).

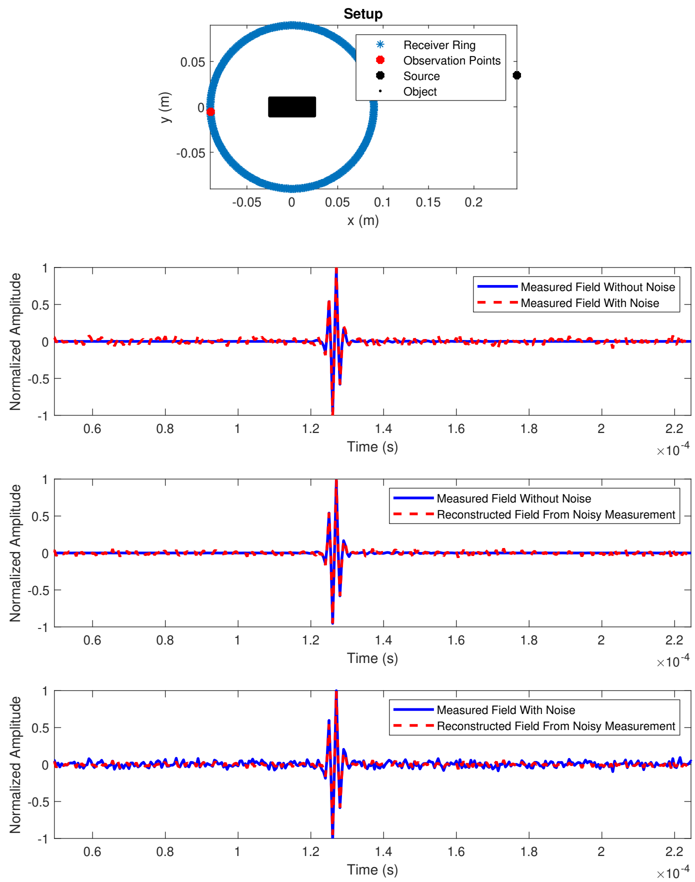

Figure 5.6: Time domain results showing the robustness of the method to noise. Setup is given at the first row. The second row shows noisy and noise-free measurements. The third row shows the noise free measurement and reconstructed signal from a noisy measurement. The fourth row shows the noisy measurement and reconstructed signal from a noisy measurement.

5.4. DISCUSSION

The method proposed in this work to redatum the measured fields is computationally efficient and suitable for water bath scanners that have a closed acquisition surface. Typically, those systems have a measurement radius greater than 20 cm. Hence, redatuming the measurements closer to the breast that may have an effective diameter of 12 cm [95] can reduce the computation time for inversion. The proposed method may also be useful for a setup that has a smaller radius. For the latter case, a non-perfect spherical or circular acquisition boundary can be easily mapped on a Cartesian grid. This is beneficial for integral-type inversion methods where FFT's may be used to compute the convolutions with the Green's function efficiently.

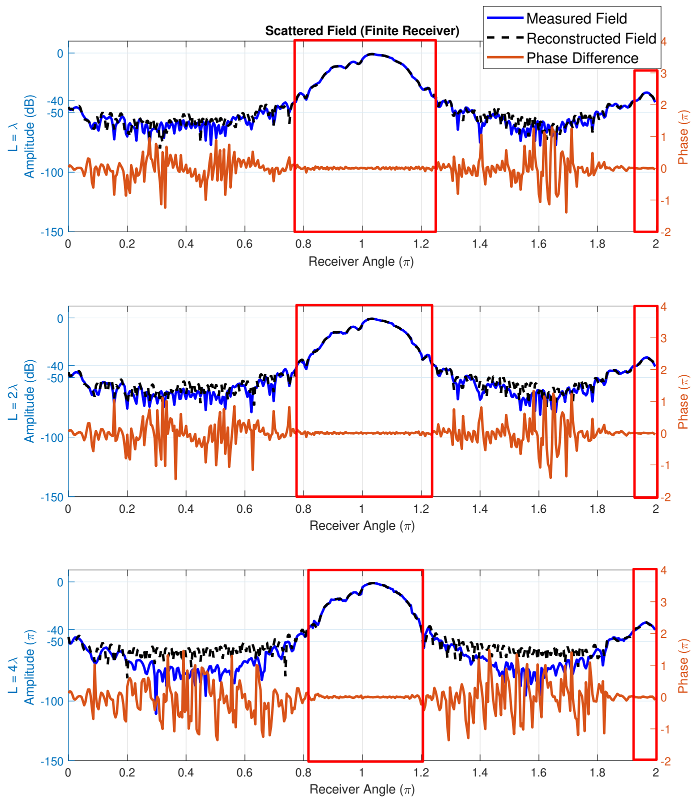

Figure 5.7: Single frequency (0.5 MHz) results using finite-sized receivers. The measured and reconstructed pressure fields using a receiver of length $L = \lambda, 2\lambda, and 4\lambda$ (top to bottom). The receivers are located at the $r = 0.09$ m circle with the normal oriented to the center. Red squares enclose the signal when the amplitude is above -40 dB.

In this work, we use CSI to solve the scattering integral equation iteratively. To compute the spatial convolutions with the Green's function efficiently we use FFT's. This requires the receivers and unknowns to be located inside the same spatial computation domain. Regarding the presented example in the experimental results section, the computation time for each iteration decreased approximately by a factor four. In addition, after redatuming the wave field to a smaller domain, CSI converges faster compared to the normal case using the same five frequency components, see Fig. 5.10. These results show that CSI has a supralinear cost functional and that the total computational gain is higher than a factor four in this case. Similar observations have been reported for the forward problem in the past [60]. There it was shown that reducing the domain of interest hides the influence of the unknowns located at points of zero contrast from the minimization procedure, thereby improving the condition number of the system and thus the convergence rate.

In a real experiment, some problems can occur with the scanning setup such as undersampled measurements, errors in receiver locations, etc. Since these problems affect any

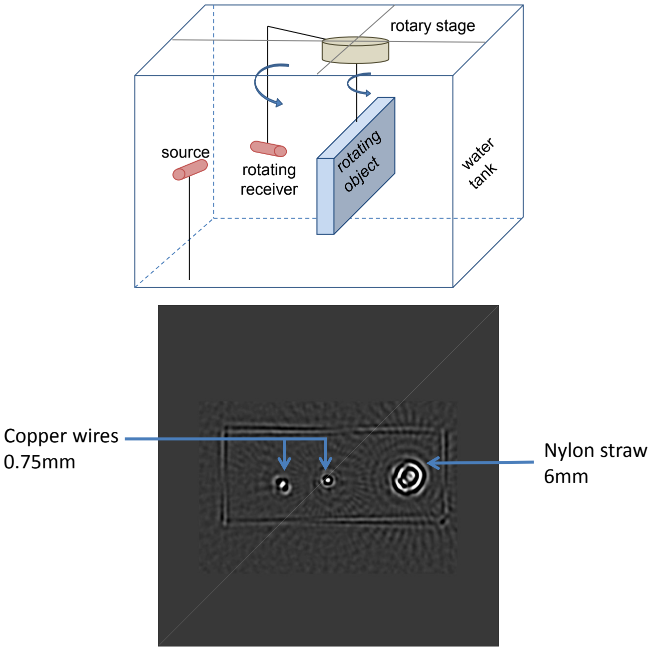

Figure 5.8: Sketch of the DBUS system (top). Reconstruction of the phantom using SAFT (bottom).

5

inversion algorithm, here it is assumed that they are already taken care of beforehand. In fact, we showed in the experimental results that the proposed method works for measured data.

The redatuming method presented in this work is computationally very efficient. For example, generating the single frequency results shown in Fig. 5.3 takes less than a second. On the other hand, each iteration of CSI takes around 5.1 minutes before redatuming and around 1.3 minutes after redatuming (using the same five frequency components). For each data set, redatuming has to be done only once while CSI has to be iterated many times. Note that, all computations are done on a Windows server with a Windows Server 2008 R2 Enterprise 64-bit operating system and Intel Xeon E5620 CPU (2.4 GHz). Redatuming is applied in MATLAB R2016b and CSI is running in a FORTRAN90 environment accelerated with OMP routines.

5.5. CONCLUSION

With redatuming, the measured acoustic wave field is transformed into a data set that is representative for a recording of the same wave field but now at a different location. A common way to migrate the wave field from one surface to another is by employing Kirchhoff integrals. Unfortunately, redatuming methods based on Kirchhoff migration fail for breast ultrasound where the recording surface is often curved and only the pressure

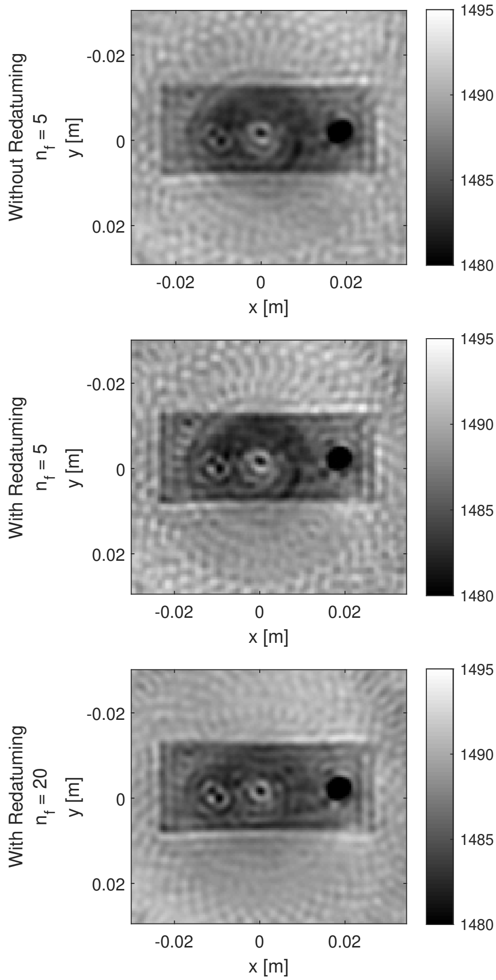

Figure 5.9: Results obtained with CSI after 128 iterations with and without redatuming. The top image shows the reconstruction using five frequency components without redatuming, the middle the reconstruction after the same five frequency components with redatuming, and the bottom the reconstruction using 20 frequency components after redatuming. The gray scale indicates speed of sound values in m/s.

field is measured.

To overcome these problems, we developed a novel redatuming method where the measured pressure field is described as a series of Hankel functions to account for the radii of the receiver locations, complex exponentials to account for angular variations and corresponding complex coefficients as weighting factors. The resulting linear system of equations is solved using Tikhonov regularization. Once the coefficients are found, the field can be redatumed to any location in the homogeneous embedding.

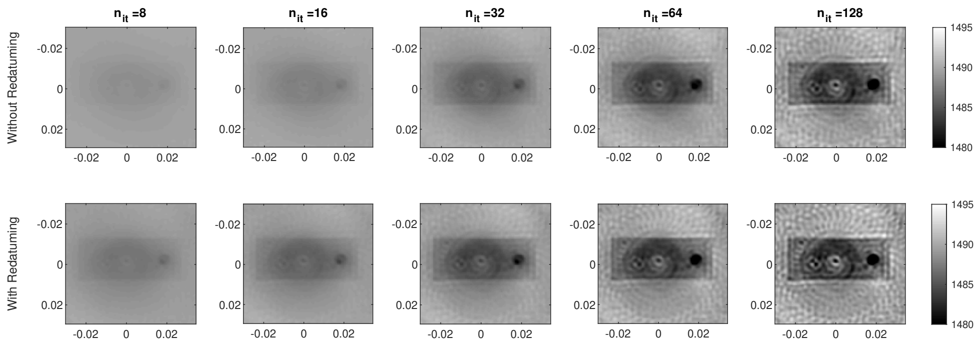

Figure 5.10: CSI results before (top row) and after (bottom row) redatuming for an increasing number of iterations (n_{it} = 8, 16, 32, 64, and 128). Note that these results are obtained using the same five frequency components. The gray scale indicates speed of sound values in m/s.

Results based on measured data show that redatuming to any location in the homogeneous embedding is possible and that it indeed leads to a reduction in computational costs. In addition, it is shown using synthetic data that it is possible to redatum when the actual measurements are done using finite-sized receivers. Finally, with a synthetic example, it is shown that the proposed method itself is robust against random noise and it also has the potential to act as a denoiser.

6

MULTI-PARAMETER INVERSION WITH THE AID OF PARTICLE VELOCITY FIELD RECONSTRUCTION[1]

Multi-parameter inversion for medical ultrasound leads to an improved tissue classification. In general, simultaneous reconstruction of volume density of mass and compressibility would require knowledge of the particle velocity field alongside with the pressure field. However, in practice the particle velocity field is not measured. In this thesis, a method for multi-parameter inversion is proposed where the particle velocity field is reconstructed from the measured pressure field in a 2-D environment. To this end, the measured pressure field is described using outward propagating Hankel functions. For a synthetic setup, it is shown that the reconstructed particle velocity field matches the forward modelled particle velocity field. Next, the reconstructed particle velocity field is used together with the synthetically measured pressure field to reconstruct density and compressibility profiles with the aid of contrast source inversion (CSI). Finally, comparing the reconstructed speed of sound profiles obtained via single-parameter versus multi-parameter inversion shows that multi-parameter outperforms single-parameter inversion with respect to accuracy and stability.

[1] This chapter has been published as:
Taskin and van Dongen, "Multi-parameter inversion with the aid of particle velocity field reconstruction," J. Acoust. Soc. Am. 47(6), 2020.
The text and notation used in this chapter may differ on minor details from the actual publication. This is done to achieve consistency between chapters and will especially be the case for the section Theory.

6.1. INTRODUCTION

Ultrasound is widely used as a medical imaging modality due to its features such as being non-invasive and safe. To retrieve quantitative information about the tissues in the image, ultrasound tomography [25], [96], [97] in combination with full-waveform inversion (FWI) [31], [38], [78], [79] is frequently used. Up to date, these methods are successfully applied in cases where the object is surrounded by transducers. Examples are the breast [26], brain [28] and bone [29].

Most inversion methods aim for speed of sound reconstruction by assuming constant mass density. This is mainly done to simplify the complex non-linear inverse problem. However, quantitative knowledge about multiple medium parameters may lead to an improved tissue characterization [35].

In various recent works, FWI is used for multi-parameter reconstruction. For example, contrast source inversion (CSI) and Born iterative method (BIM) are used to reconstruct compressibility, attenuation and density [80], [98]. In these works the parameters are directly reconstructed from the pressure field measurements. However, with these methods additional regularization is needed to reconstruct the density accurately [99]. Alternatively, the particle velocity field is used together with the pressure field to reconstruct density and compressibility simultaneously using a full vectorial CSI scheme [100]. Unfortunately, in practice only the pressure field is measured and the particle velocity field is unknown. Therefore, full vectorial CSI method can not be used directly in practical applications.

In this work, we propose a multi-parameter inversion method where we first reconstruct the particle velocity field from the pressure field measured on a closed arbitrary-shaped two-dimensional (2-D) curvature. The particle velocity field reconstruction method is based on Hankel function decomposition of the measured pressure field [101]. Once the pressure field is expressed with Hankel functions, the particle velocity field is computed by applying the gradient operator to the derived expression. After a successful reconstruction of the particle velocity field from the pressure field, both the compressibility and the mass density are reconstructed using a vectorial CSI scheme [100].

The chapter is organized as follows. Section 6.2 presents the forward model, the method to reconstruct the particle velocity field from the pressure field and finally the inverse problem. Section 6.3 presents numerical examples in which the reconstructed particle velocity field is compared with the ground truth. In addition, reconstructed density, compressibility and speed of sound profiles are presented. These profiles are obtained by employing CSI on the measured pressure and reconstructed particle velocity field. Finally, conclusions are given in Section 6.4.

6.2. THEORY

Consider an arbitrary-shaped object with unknown medium properties within the spatial domain $\mathbb{D}$ enclosed by the boundary $\mathbb{S}$. The sources and receivers are located on the boundary $\mathbb{S}$, see Fig. 6.1. The boundary $\mathbb{S}$ is located in the homogeneous lossless embedding with speed of sound c_0, volume density of mass ρ_0 and compressibility κ_0. The object domain is heterogeneous in all three medium parameters. The Cartesian and polar position vectors are denoted by $\boldsymbol{x} = (x, y)$ and $\boldsymbol{r} = (r, \phi)$ respectively. The following theory

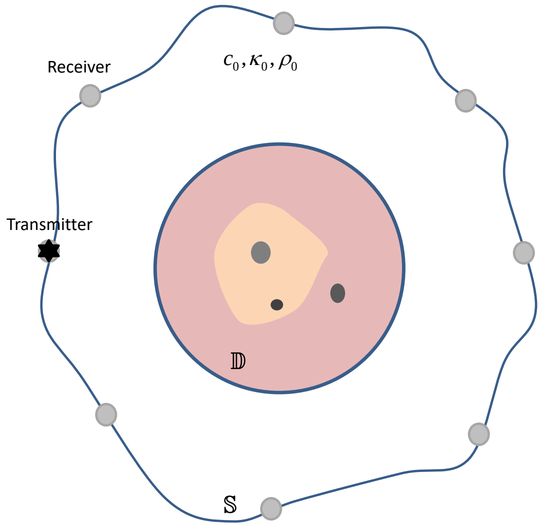

Figure 6.1: Schematic representation of the setup. Transmitters and receivers are located in $\mathbb{S}$. $\mathbb{S}$ encloses the object within the domain $\mathbb{D}$.

6

is presented in the temporal Fourier domain with angular frequency ω.

6.2.1. FORWARD PROBLEM

The acoustic field equations are given by the equation of motion and deformation. As shown in chapter 2, in the temporal Fourier domain and for loseless media these equations read [54], [102]

$$\nabla \hat{p}(\boldsymbol{x}) + i\omega\rho(\boldsymbol{x})\hat{\boldsymbol{v}}(\boldsymbol{x}) = \hat{\boldsymbol{f}}(\boldsymbol{x}) \tag{6.1}$$

and

$$\nabla \cdot \hat{\boldsymbol{v}}(\boldsymbol{x}) + i\omega\kappa(\boldsymbol{x})\hat{p}(\boldsymbol{x}) = \hat{q}(\boldsymbol{x}), \tag{6.2}$$

where $\hat{p}(\boldsymbol{x})$ is the pressure wave field, $\hat{\boldsymbol{v}}(\boldsymbol{x})$ is the particle velocity wave field, $\rho(\boldsymbol{x})$ is the volume density of mass, $\kappa(\boldsymbol{x})$ is the compressibility, $\hat{\boldsymbol{f}}(\boldsymbol{x})$ is the volume source density of volume force, $\hat{q}(\boldsymbol{x})$ is the volume source density of injection rate, i is the imaginary number defined via the relation $i^2 = -1$, and ∇ is the nabla operator. The caret symbol $\hat{}$ is used for quantities defined in the temporal Fourier domain. The incident wave fields $\hat{p}^{inc}(\boldsymbol{x})$ and $\hat{\boldsymbol{v}}^{inc}(\boldsymbol{x})$ are defined as the wave fields that are generated by the primary sources $\hat{q}(\boldsymbol{x})$ and $\hat{\boldsymbol{f}}(\boldsymbol{x})$, and that propagate in the homogeneous embedding in the absence of any acoustic contrast. In view of this definition, the scattered wave fields $\hat{p}^{sct}(\boldsymbol{x})$ and $\hat{\boldsymbol{v}}^{sct}(\boldsymbol{x})$ are defined as the numerical difference between the actual or total wave fields $\hat{p}(\boldsymbol{x})$ and $\hat{\boldsymbol{v}}(\boldsymbol{x})$, and the incident wave fields $\hat{p}^{inc}(\boldsymbol{x})$ and $\hat{\boldsymbol{v}}^{inc}(\boldsymbol{x})$. As shown in chapter 2, the scattered fields can be written in integral form as [54], [102]

$$\hat{p}^{sct}(\boldsymbol{x}) = \hat{p}(\boldsymbol{x}) - \hat{p}^{inc}(\boldsymbol{x}) = \frac{\omega^2}{c_0^2}\int_{\boldsymbol{x}'\in\mathbb{D}} \hat{G}(\boldsymbol{x}-\boldsymbol{x}')\chi^{\kappa}(\boldsymbol{x}')\hat{p}(\boldsymbol{x}')\mathrm{d}V(\boldsymbol{x}') + i\omega\rho_0\nabla\cdot\int_{\boldsymbol{x}'\in\mathbb{D}} \hat{G}(\boldsymbol{x}-\boldsymbol{x}')\chi^{\rho}(\boldsymbol{x}')\hat{\boldsymbol{v}}(\boldsymbol{x}')\mathrm{d}V(\boldsymbol{x}') \tag{6.3}$$

and

$$\hat{\boldsymbol{v}}^{sct}(\boldsymbol{x}) = \hat{\boldsymbol{v}}(\boldsymbol{x}) - \hat{\boldsymbol{v}}^{inc}(\boldsymbol{x}) = i\omega\kappa_0\nabla\int_{\boldsymbol{x}'\in\mathbb{D}} \hat{G}(\boldsymbol{x}-\boldsymbol{x}')\chi^{\kappa}(\boldsymbol{x}')\hat{p}(\boldsymbol{x}')\mathrm{d}V(\boldsymbol{x}') - \nabla\nabla\cdot\int_{\boldsymbol{x}'\in\mathbb{D}} \hat{G}(\boldsymbol{x}-\boldsymbol{x}')\chi^{\rho}(\boldsymbol{x}')\hat{\boldsymbol{v}}(\boldsymbol{x}')\mathrm{d}V(\boldsymbol{x}') - \chi^{\rho}(\boldsymbol{x})\hat{\boldsymbol{v}}(\boldsymbol{x}), \tag{6.4}$$

where $\hat{G}(\boldsymbol{x}-\boldsymbol{x}')$ is the Green's function describing the impulse response of the homogeneous embedding. The Green's function in 2-D equals

$$\hat{G}(\boldsymbol{x}-\boldsymbol{x}') = \frac{i}{4}H_0^{(2)}(k_0|\boldsymbol{x}-\boldsymbol{x}'|), \tag{6.5}$$

where $H_0^{(2)}$ is the zero-order Hankel function of the second kind. The contrast functions $\boldsymbol{\chi}^{\kappa}(\boldsymbol{x})$ and $\boldsymbol{\chi}^{\rho}(\boldsymbol{x})$ are defined as

$$\boldsymbol{\chi}^{\kappa}(\boldsymbol{x}) = \frac{\kappa(\boldsymbol{x})-\kappa_0}{\kappa_0} \tag{6.6}$$

and

$$\boldsymbol{\chi}^{\rho}(\boldsymbol{x}) = \frac{\rho(\boldsymbol{x})-\rho_0}{\rho_0}. \tag{6.7}$$

Equations (6.3) and (6.4) can be solved numerically for known sources and known contrast functions to find the unknown total wave fields inside the spatial domain $\mathbb{D}$. In literature, this situation is referred to as the forward problem. The situation where the sources generating the wave fields as well as the total wave fields at the boundary $\mathbb{S}$ are known, and where both the total wave fields and the contrast functions are unknown within the domain of interest $\mathbb{D}$ is referred to as the inverse problem. Unfortunately, in practice one only measures the pressure field and not the particle velocity field. In section 6.2.2 we present a method that allows us to reconstruct the particle velocity field from the measured pressure field.

6.2.2. PARTICLE VELOCITY FIELD RECONSTRUCTION

Multi-parameter inversion requires knowledge of both the pressure and particle velocity wave fields, where the latter one is not measured in practice. Here we present a method to construct the particle velocity field from pressure field measurements.

The scattered field satisfies the 2-D Helmholtz equation, which reads in polar coordinates

$$r^2\frac{\partial^2\hat{p}^{sct}(\boldsymbol{r})}{\partial r^2} + r\frac{\partial\hat{p}^{sct}(\boldsymbol{r})}{\partial r} + \frac{\partial^2\hat{p}^{sct}(\boldsymbol{r})}{\partial\phi^2} + r^2\frac{\omega^2}{c^2(\boldsymbol{r})}\hat{p}^{sct}(\boldsymbol{r}) = 0. \tag{6.8}$$

As it is shown in chapter 5, under the condition that the solution of Equation (6.8) represents an outward propagating wave field at the boundary of $\mathbb{S}$, the resulting scattered field may be formulated as [101]

$$\hat{p}^{sct}(\boldsymbol{r}) = \sum_{n=-N}^{N} \hat{c}_n H_n^{(2)}\left(\frac{\omega}{c_0} r\right) e^{in\phi}, \tag{6.9}$$

where $H_n^{(2)}\left(\frac{\omega}{c_0} r\right)$ are Hankel functions of the second kind and order n representing the outward propagating waves [88]. To find the complex valued coefficients $\hat{c}_n$ for each angular frequency ω, Equation (6.9) is solved for $\hat{c}_n$ using the known scattered pressure field $\hat{p}^{sct}(\boldsymbol{r})$ measured on $\mathbb{S}$ [101]. Once the coefficients $\hat{c}_n$ are reconstructed, the scattered particle velocity field $\hat{\boldsymbol{v}}^{sct}(\mathbf{r})$ is computed by considering the gradient of the scattered pressure field, hence

$$\hat{\boldsymbol{v}}^{sct}(\mathbf{r}) = -\frac{1}{i\omega\rho_0} \nabla \hat{p}^{sct}(\mathbf{r}). \tag{6.10}$$

By combining Equations (6.9) and (6.10) the following expressions for the particle velocity field in cylindrical coordinates $\hat{\boldsymbol{v}}^{sct}(\boldsymbol{r}) = (\hat{v}_r^{sct}(\boldsymbol{r}), \hat{v}_\phi^{sct}(\boldsymbol{r}))$ are obtained

$$\begin{aligned} \hat{v}_r^{sct}(\mathbf{r}) &= -\frac{1}{i\omega\rho_0} \frac{\partial \hat{p}^{sct}(\boldsymbol{r})}{\partial r} \\ &= -\frac{1}{i\omega\rho_0} \times \sum_{n=-N}^{N} \left[H_{n-1}^{(2)}\left(\frac{\omega}{c_0} r\right) - H_{n+1}^{(2)}\left(\frac{\omega}{c_0} r\right) \right] \hat{c}_n \frac{\omega}{2c_0} e^{in\phi} \end{aligned} \tag{6.11}$$

and

$$\hat{v}_\phi^{sct}(\mathbf{r}) = -\frac{1}{i\omega\rho_0} \frac{\partial \hat{p}^{sct}(\boldsymbol{r})}{\partial \phi} = -\frac{1}{i\omega\rho_0} \times \sum_{n=-N}^{N} in\hat{c}_n H_n^{(2)}\left(\frac{\omega}{c_0} r\right) e^{in\phi}, \tag{6.12}$$

where we use recurrence relations to compute the spatial derivatives of the Hankel functions [103].

6.2.3. INVERSE PROBLEM

FWI methods aim to reconstruct medium parameters by iteratively minimizing a cost function. Typically, this cost function contains at least one term that shows a measure for the mismatch between the measured and the modelled wave fields. A well-known FWI method is CSI. This method can be implemented such that it reconstructs multiple medium parameters simultaneously [100].

MULTI-PARAMETER INVERSION

Employing CSI for a multi-parameter inverse problem requires the formulation of the following cost functional

$$\mathrm{Err}^{(1)} = \eta_{\mathbb{S}}^{pv} \left\| \begin{matrix} \mathbf{p}^{sct} - \mathbf{L}_p^{\mathbb{S}}[\mathbf{w}^\kappa, \mathbf{w}^\rho] \\ \mathbf{v}^{sct} - \mathbf{L}_v^{\mathbb{S}}[\mathbf{w}^\kappa, \mathbf{w}^\rho] \end{matrix} \right\|_{\mathbb{S}}^2 + \eta_{\mathbb{D}}^{pv} \left\| \begin{matrix} \boldsymbol{\chi}^\kappa \mathbf{p}^{inc} + \boldsymbol{\chi}^\kappa \mathbf{L}_p^{\mathbb{D}}[\mathbf{w}^\kappa, \mathbf{w}^\rho] - \mathbf{w}^\kappa \\ \boldsymbol{\chi}^\rho \mathbf{v}^{inc} + \boldsymbol{\chi}^\rho \mathbf{L}_v^{\mathbb{D}}[\mathbf{w}^\kappa, \mathbf{w}^\rho] - \mathbf{w}^\rho \end{matrix} \right\|_{\mathbb{D}}^2, \tag{6.13}$$

where $\eta_{\mathbb{S}}^{pv}$ and $\eta_{\mathbb{D}}^{pv}$ are normalization terms, $\mathbf{L}_p^{\mathbb{S}}$, $\mathbf{L}_p^{\mathbb{D}}$, $\mathbf{L}_v^{\mathbb{S}}$ and $\mathbf{L}_v^{\mathbb{D}}$ are integral operators that map the contrast sources $\mathbf{w}^\kappa$ and $\mathbf{w}^\rho$ to the pressure and particle velocity wave fields in $\mathbb{S}$

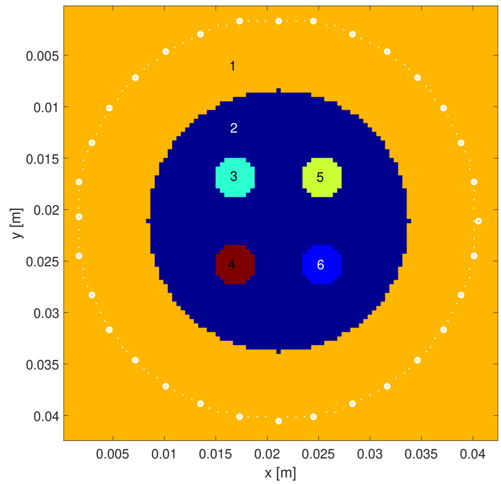

Figure 6.2: Synthetic breast phantom. The large and small white dots show the locations of the sources and the receivers respectively. The numbers indicate the different tissue types.

and $\mathbb{D}$, and where $||\cdot||_{\mathbb{S}}$ and $||\cdot||_{\mathbb{D}}$ represent the l_2-norm of a quantity defined in $\mathbb{S}$ and $\mathbb{D}$ respectively. For a spatially varying compressibility and density the contrast sources equal

$$\mathbf{w}^{\kappa} = \chi^{\kappa}\mathbf{p} \tag{6.14}$$

and

$$\mathbf{w}^{\rho} = \chi^{\rho}\mathbf{v}. \tag{6.15}$$

To solve the inverse problem for the unknown contrast functions χ^{κ} and χ^{ρ}, the cost function in Equation (6.13) is minimized iteratively for known incident fields in $\mathbb{S}$ and $\mathbb{D}$ and scattered fields in $\mathbb{S}$.

SINGLE-PARAMETER INVERSION

It is common practice to assume a constant density throughout the entire domain, i.e. $\rho(\boldsymbol{r}) = \rho_0$. Within this assumption the vectorial problem reduces to a scalar problem and the cost function $\mathrm{Err}^{(1)}$ for CSI that needs to be minimized reduces to, [76]

$$\mathrm{Err}^{(2)} = \eta_{\mathbb{S}} \left\| \mathbf{p}^{\mathrm{sct}} - \mathbf{L}_p^{\mathbb{S}}[\mathbf{w}^{\kappa}] \right\|_{\mathbb{S}}^2 + \eta_{\mathbb{D}} \left\| \boldsymbol{\chi}^{\kappa}\mathbf{p}^{\mathrm{inc}} - \mathbf{w}^{\kappa} - \boldsymbol{\chi}^{\kappa}\mathbf{L}_p^{\mathbb{D}}[\mathbf{w}^{\kappa}] \right\|_{\mathbb{D}}^2. \tag{6.16}$$

Note that, for this single-parameter inversion a spatially varying speed of sound profile is obtained via the relation $c(\boldsymbol{x}) = \dfrac{1}{\sqrt{\kappa(\boldsymbol{x})\rho_0}}$.

6.3. RESULTS

A synthetic example is presented in this section. First, the forward problem is solved to obtain both pressure and particle velocity fields [104]. Next, the particle velocity field is computed with the proposed method and compared with the "exact" result obtained by

Table 6.1: Medium parameters of the tissues.

Tissue #	c [m/s]	ρ [kg/m^3]	κ [1/Pa]
1	1520	996	0.435e-9
2	1494	1013	0.442e-9
3	1514	986	0.442e-9
4	1527	986	0.435e-9
5	1514	1013	0.430e-9
6	1494	1041	0.430e-9

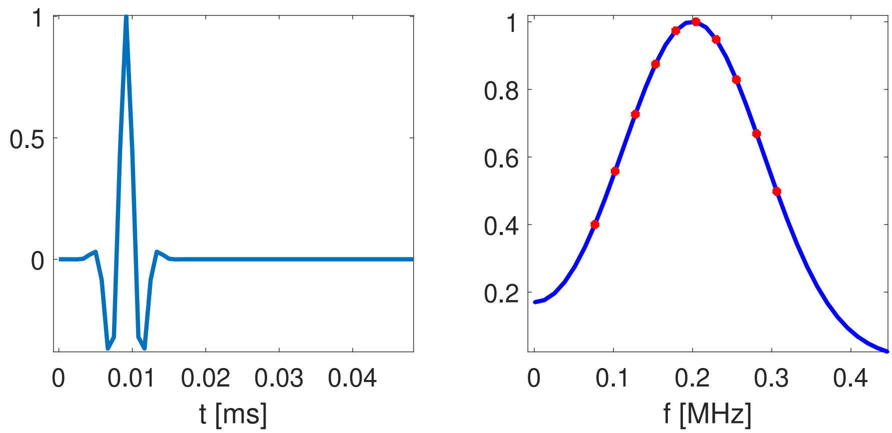

Figure 6.3: Excitation profile in time (left) and frequency (right) domain. The red dots indicate the frequency components used with CSI.

directly solving the forward problem. Finally, contrasts source inversion (CSI) is used as a multi- and single-parameter inversion method.

6.3.1. CONFIGURATION

A synthetic "breast" phantom is used in this work. The phantom alongside with the transducer locations is shown in Fig. 6.2. The medium parameters of the tissues are listed in Table 6.1 [67], [70]. Attenuation is neglected since it is known to have little effect on the acoustic fields at these frequencies [90]. The spatial domain contains 100×100 elements of size 0.42 mm $\times$ 0.42 mm. The 32 sources and 128 receivers are equally distributed over the white dotted circle indicating $\mathbb{S}$ (see Fig. 6.2) [36]. In Fig. 6.3, the source excitation is given; a Gaussian modulated pulse with a center frequency $f_0 = 0.2$ MHz.

6.3.2. SOLUTION OF FORWARD PROBLEM

Synthetic data (both pressure and particle velocity field) is obtained by solving the forward problem for the breast phantom in the frequency domain [104]. Time-domain results are obtained using inverse Fourier transformations.

Fig. 6.4 shows snapshots of the incident, scattered and total pressure and particle ve-

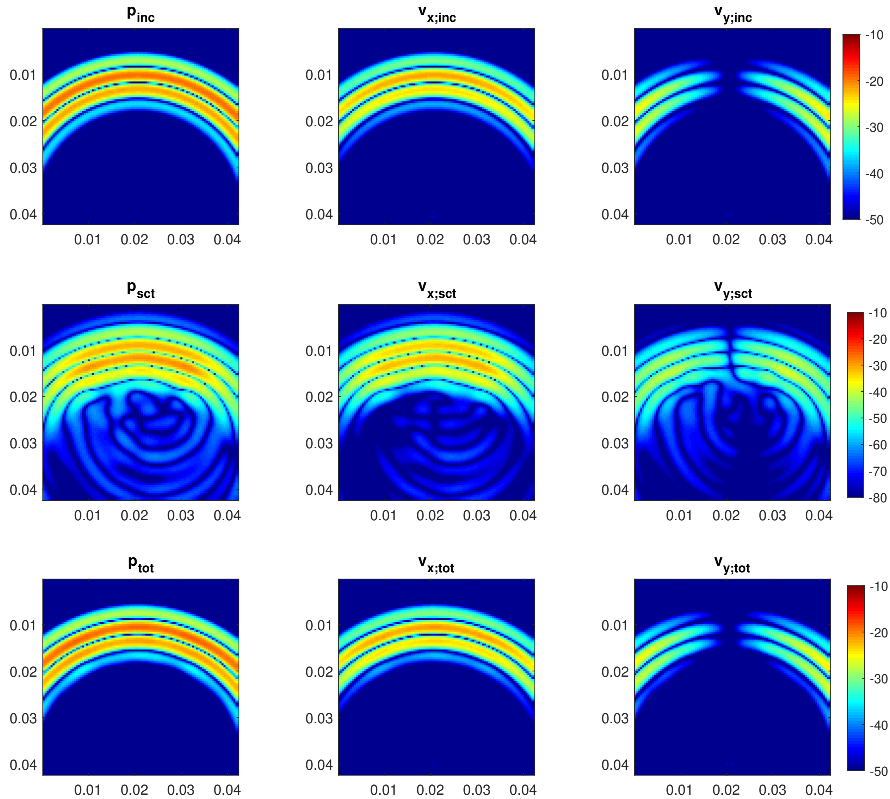

Figure 6.4: Snapshots of incident (top row), scattered (middle row) and total fields (bottom row) at $t = 28\mu s$. Left column shows the pressure field; the middle and right columns the particle velocity fields. All fields are normalized with respect to the maximum absolute value and shown on a dB scale.

locity fields at $t = 28$ μs. The source is located at $(x, y) = (21\text{ mm}, 41\text{ mm})$. The wave fields are computed by solving the full-wave forward problem for the pressure and particle velocity field simultaneously. The obtained particle velocity field will serve as a benchmark for the reconstructed particle velocity field.

6.3.3. VELOCITY FIELD RECONSTRUCTION

The particle velocity fields are reconstructed from the pressure fields using the proposed method. These pressure fields are synthetically measured by the 128 receivers indicated by the small white dots in Fig. 6.2 and a single source that is located at $(x, y) = (41\text{ mm}, 21\text{ mm})$.

First, frequency-domain results are shown in Fig. 6.5. The top row shows the pressure fields measured in the receiver locations; in blue the synthetically generated and in red the reconstructed pressure fields. The following rows show the particle velocity fields. It is observed from these results that the reconstructed fields have an excellent match with the synthetically generated fields for both amplitude and phase.

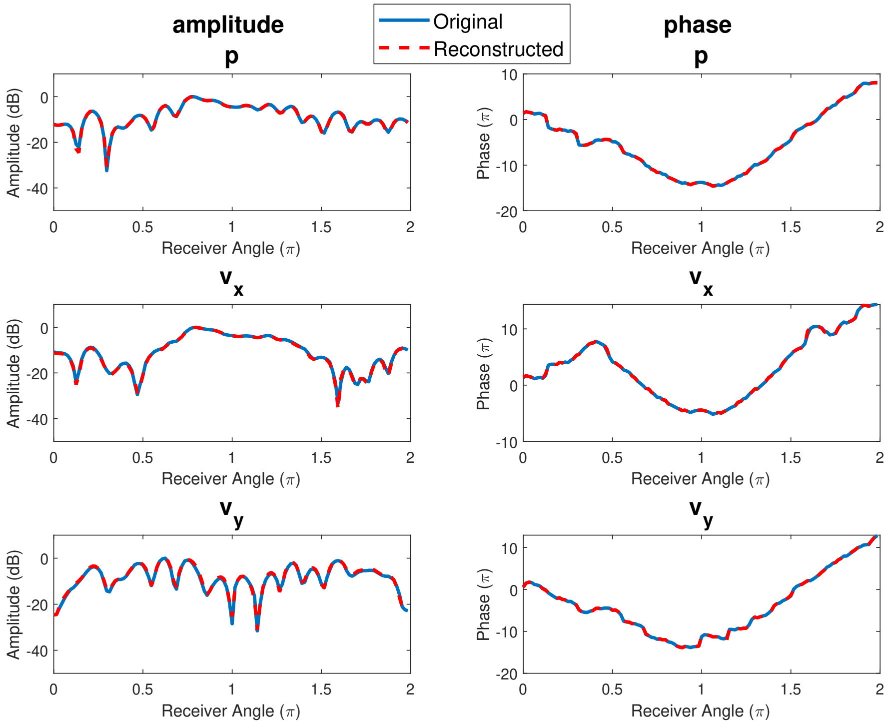

Figure 6.5: Particle velocity field reconstruction results in frequency domain. Both amplitude (left column) and phase (right column) of the synthetically generated and reconstructed fields are shown. Top row shows the Hankel decomposition of the pressure field (red) with the synthetically generated (blue); middle and bottom row the reconstructed particle velocity fields (red) together with the synthetically generated (blue).

Next, time-domain results are shown in Fig. 6.6. The source and receiver locations are shown in the image at the top. A-scans at the given receiver locations for the particle velocity field are given in the bottom images. Ground truth and reconstructed fields are plotted together. These results show that the proposed method works well over the entire bandwidth.

6.3.4. SOLUTION OF INVERSE PROBLEM

The effect of the particle velocity field on the inversion is shown in this subsection. First, CSI is used in its traditional way [73] by using only the pressure field and inverting for the speed of sound (assuming constant density) only. Note that, the forward problem is based on a spatially varying compressibility as well as density profile. Next, CSI is used as described in Ref. [100] by using pressure and particle velocity fields together and inverting for both compressibility and density. For all examples, 32 sources and 128 receivers are used, all equally distributed on a circle with radius $r = 20$ mm, see Fig. 6.2. Ten frequency

6

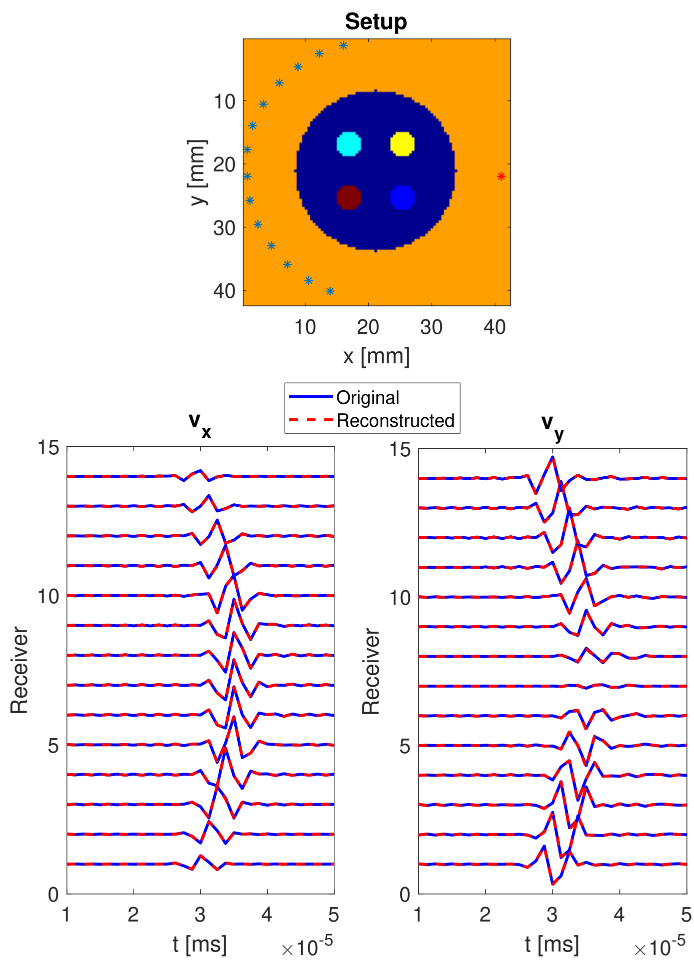

Figure 6.6: Particle velocity field reconstruction results in time domain. The top image shows the locations of the source (red star) and the 15 receivers (blue stars). The bottom images show the reconstructed particle velocity field (red) together with the ground truth (blue). Note that, all fields are normalized with respect to the maximum value.

components are used for the inversion, see Fig. 6.3.

Fig. 6.7 shows the single-parameter inversion results obtained with CSI after 2048 iterations. The first row shows the true compressibility, density and speed of sound profiles. The second row shows the inversion results using pressure field only and assuming constant density. The four small lesions are all visible in the results but with wrong parameter values. The values for the compressibility and density contrast in the lower right corner are selected such that the small cylinder doesn't show any speed of sound contrast with respect to its direct surrounding but that it still will give rise to scattering. Not allowing for a density contrast during reconstruction automatically means the formation of an er-

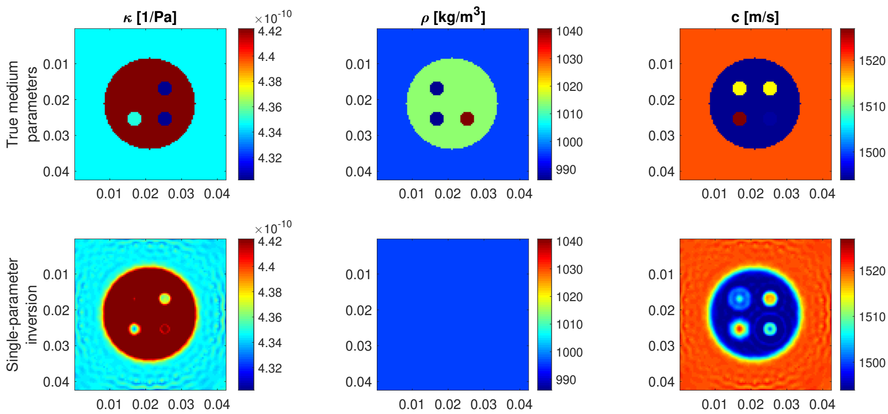

Figure 6.7: CSI results (single parameter). Top row shows the true compressibility, density and speed of sound profiles; bottom row shows the CSI reconstruction using the synthetically generated pressure field only and assuming constant density. Note that with this example we intend to show the leakage of density contrast into a compressibility and hence speed of sound contrast.

roneous speed of sound contrast at this particular location.

Note that in literature there are works that show that single-parameter inversion reconstructs speed of sound accurately with experimental data. With this specific example we intended to show where these single-parameter inversion methods might face problems.

Fig. 6.8 shows the multi-parameter inversion results obtained with CSI after 2048 iterations. The first row shows the true compressibility, density and speed of sound profiles. These profiles are identical to the ones used in Fig. 6.7. The second row shows the inversion results using the synthetically generated pressure and particle velocity fields. The third row shows the inversion results when the synthetically generated pressure and reconstructed particle velocity fields are used to invert for both density and compressibility. In both cases similar results are obtained and the four small lesions have almost the correct parameter values. The ripples seen in the background are caused by the coarse discretization of the domain and can be solved by using a finer spatial discretization or additional regularization based on total variation or sparsity constraints [76], [105]. Integral equation formulations have the advantage that they perform well with relatively coarse sampling because of having a bounded operator. This is valid for CSI for the single-parameter inversion. However, this feature is not valid for the multi-parameter inversion anymore. The operator in multi-parameter inversion is unbounded because of the spatial derivatives involved. Therefore, a finer discretization will improve these results.

To examine the performance of the method against noise, we added 5% complex valued white noise to the data. Results for the reconstructions are shown in Fig. 6.9. It can be seen from these results that all small inclusions are reconstructed with a good accuracy.

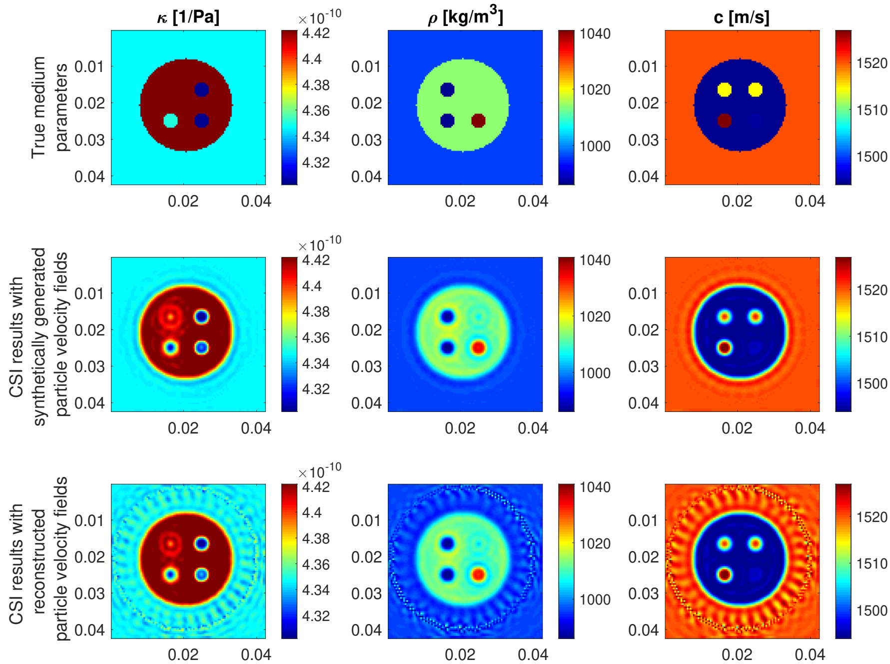

Figure 6.8: CSI results (multi parameter). Top row shows the true compressibility, density and speed of sound profiles; middle row shows the CSI reconstruction using synthetically generated pressure and particle velocity fields; bottom row shows the CSI reconstruction using pressure field together with reconstructed particle velocity fields.

6

6.4. CONCLUSION

In this chapter, we present a multi-parameter FWI method where the required particle velocity field is reconstructed from the measured pressure field using Hankel function decomposition. The inversion method has been successfully tested using a 2-D synthetic example; a breast phantom containing heterogeneities in compressibility, density and speed of sound.

First we have tested the particle velocity field reconstruction method. To this end, the particle velocity field obtained by solving the full vectorial forward problem has been compared with the reconstructed particle velocity field using the synthetically measured pressure field. It has been shown that both particle velocity fields matches each other perfectly well.

Next, the synthetically measured pressured field has been used together with the reconstructed particle velocity field to successfully invert for density, compressibility and speed-of sound profiles using an FWI method referred to as contrast source inversion (CSI). Finally, CSI has been implemented in its traditional way where only a pressure field is used to invert for a speed of sound profile given the assumption of a constant density. Application of this single-parameter inversion on the synthetic data derived from the multi-parameter synthetic breast phantom gives rise to “ghost” objects in the resulting

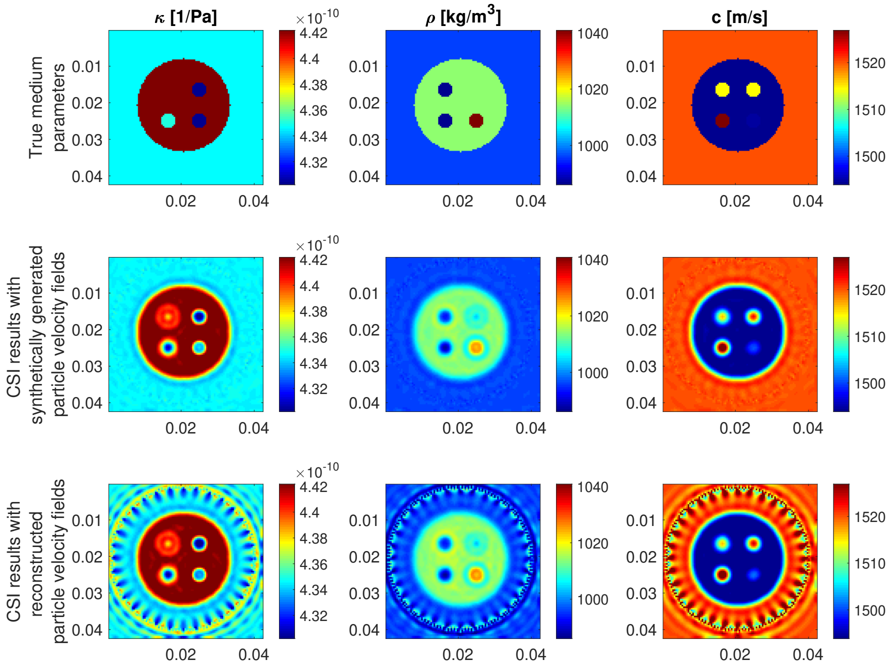

Figure 6.9: Same as Fig. 6.8 but now with 5% noise added to the data.

6

speed of sound profile. These results underline the importance of multi-parameter inversion in case the object of interest shows spatial variations in compressibility, density and speed of sound.

Attenuation is another important parameter in medical ultrasound. There are already quite some inversion related publications that include attenuation. We believe that it needs a detailed examination in a future work. Finally, a 3-D extension of the method introduced in this chapter is straightforward and will only lead to an increase in computational load. [106]

7

CONCLUSION AND RECOMMENDATIONS

7.1. CONCLUSION

Full-waveform inversion (FWI) is a well-established imaging technique that is widely used within the oil and gas exploration community. Recently, various attempts have been made to share and apply this knowledge within the field of medical ultrasound. These attempts have been particular successful for breast ultrasound. To maximize the performance of FWI for breast cancer detection using ultrasound, additional research is required.

The forward model is an essential building block of FWI. That's why we started this thesis with examining various forward solvers. We showed that modeling methods that use some kind of approximation, in particular Born, paraxial or ray, for efficiency reasons fail to accurately model the waves propagating through the breast when compared to a full-waveform modeling technique. With aforementioned approximations, wave phenomena such as (back) scattering, refraction, diffraction are not always included. In addition, we evaluated the effect the individual acoustical medium parameters (compressibility, density and attenuation) have on the scattered pressure field. The most important observation is that, for frequencies below 1 MHz, attenuation has a neglectible effect. From the above results, we conclude that a full-waveform modeling technique is required during inversion in order to get accurate reconstructions.

In this thesis, we use an FWI method technique referred to as contrast source inversion (CSI). CSI is based on a frequency-domain integral-equation formulation. To stabilize the inversion, regularization based on total variation or sparsity may be used. In addition, we point out cycle-skipping problem and propose a frequency-hopping technique implemented in CSI to overcome that problem.

To reduce the computation time for FWI, a redatuming method that is based on Hankel function decomposition is developed. By redatuming the receivers closer to the region of interest, the spatial computational domain is reduced and unnecessary computations for reconstructing the homogeneous embedding are avoided. Another important feature of the presented redatuming method is that the particle velocity field can be reconstructed from a pressure field measurements only. This particle velocity is required for multi-parameter inversion. With multi-parameter inversion density and compressibility profiles are reconstructed simultaneously. It is shown that with the proposed multi-parameter inversion scheme accurate reconstruction results are obtained without using additional regularization. Having both medium parameters is useful for tissue classification.

7.2. RECOMMENDATIONS FOR FURTHER RESEARCH

7.2.1. EXTENSION TO THREE-DIMENSIONAL INVERSION

The work presented in this thesis mainly focuses on two-dimensional (2-D) problems due to computational restrictions. Although the forward problem is investigated for a 3-D breast model in Chapter 3, redatuming and multi-parameter inversion are done in 2-D in Chapter 5 and Chapter 6. Fortunately, the implementation of CSI in 3-D is a straightforward exercise. Moreover, in Appendix A, we present a 3-D implementation of redatuming and CSI for a relatively small domain. In a real measurement scenario, measured data have 3-D characteristics and it is desired to use 3-D inversion to avoid artifacts that occur due to 2-D assumptions. Thanks to the increase in computational power, a full 3-D implementation of FWI in a clinical setting should be feasible within the near future.

7.2.2. GENERATING A STARTING MODEL FOR FWI

7

In this thesis a homogeneous background, which is water for a water-bath scanner, is used as a starting model for our CSI. In principle, with the availability of low frequency data, a homogeneous water model is a good starting point for breast imaging. However, in many cases low frequency data is not available and therefore a homogeneous water model may not be good enough as a starting model for FWI. Mainly because 'cycle-skipping' problems will occur when only high frequencies are used for the inversion. As a result of that, FWI may get stuck in a local minimum, resulting in a poor reconstruction. One solution to the cycle-skipping problem in the presence of low and high frequency data is to implement a frequency-hopping technique for FWI. With frequency hopping, inversion is started from the lowest available frequency component. The resulting speed of sound profile is subsequently used as a starting model for the higher frequency components to avoid the cycle-skipping problem. Although frequency-hopping is an efficient solution to the cycle-skipping problem, it still requires low frequency data. An other solution is to employ a fast tomographic reconstruction method such as filtered-backpropagation and use the resulting speed of sound profile as a starting model for FWI.

7.2.3. LOCAL INVERSION

Current implementation of CSI requires a computational domain that includes the receivers. With the redatuming method used in this work, receivers can be redatumed to any location in the homogeneous embedding outside the target domain. That helps to reduce the computational domain and hence inversion time to some extend. However, the computational domain needs to cover the entire breast and may therefore still be a relatively large domain. Consequently, it may be interesting to develop a redatuming method that can redatum the wavefield inside the breast in the direct neighborhood of the suspicious lesion. By doing that, a local inversion can be applied on a significantly smaller domain which will be computationally very efficient.

7.2.4. MACHINE LEARNING

Although machine learning is out of the scope of this thesis, there is still a huge interest to apply machine learning on all kinds of medical imaging applications. Machine learning can be selected as a possible direction for future research. There is a variety of research topics with machine learning for breast ultrasound. For example, it may be used to generate a starting model for FWI or as a constraint during inversion instead of TV.

7.2.5. IN-VIVO MEASUREMENTS

This thesis includes only synthetic examples and lab measurements for CSI. Obviously, the next step for the current research is applying CSI together with the ideas presented in this thesis on in-vivo measurement data obtained in a clinical setting. Implementation of the presented techniques is expected to be straightforward. However, there are some issues that needs to be deal with. One problem is patient movement during the scan. This problem might lead to blurry reconstructions. Another problem is the calibration of the scanning system. A calibration method needs to be designed to obtain exact transducer locations, source wavelet, water temperature, etc.

7.2.6. OTHER APPLICATIONS

FWI has shown its potential by successfull application to water bath breast scanners. Certainly, FWI could also be used for other suitable applications. One possible candidate is the brain. It is still challenging to image the brain accurately with ultrasound because of the skull. Fortunately, some promising initial results have already been obtained with the application of FWI on the brain [28]. More research is required to improve these initial results. Another possible application is bone [29]. It is difficult to penetrate into the bone with acoustic waves because it has a relatively high speed of sound value compared to the surrounding soft tissue. With FWI however, a speed-of-sound profile of the bone and the surrounding tissue could be retrieved. Finally, it might be needed to include perfectly matching layers in the model to account for the finite size of the computational domain [59].

A

Appendix A: 3-D redatuming for breast ultrasound[1]

Breast cancer is the most common form of cancer diagnosed with women. To reduce its mortality rate, early diagnosis is important. In the past, this has led to the introduction of national screening programs using mammography. The disadvantages of mammography (application of ionizing radiation and low detection rate in dense breast) resulted in the demand for an alternative. This demand has led to the development of ultrasonic water bath scanning systems. Those systems scan the breast from all sides and aim for reconstructing the acoustic tissue properties from the measured pressure fields by employing among others full-waveform inversion (FWI) methods. However, FWI is computationally expensive, especially in 3-D, and scales almost linear with the size of the spatial domain. To reduce the computational load, we propose a method that reduces the size of the spatial computational domain by back-propagating the field measured on the surface of the 3-D scanning geometry to a surface enclosing a reduced volume. To this end, the measured field is first decomposed into spherical Hankel functions with complex coefficients and subsequently redatumed to a new surface closer by the object. The proposed redatuming method is tested successfully for 3-D synthetic examples.

[1] This chapter has been published as:
Taskin and van Dongen, "3-D redatuming for breast ultrasound," Medical Imaging, SPIE, 2020.
The text and notation used in this chapter may differ on minor details from the actual publication. This is done to achieve consistency between chapters and will especially be the case for the section Theory.

A.1. INTRODUCTION

Recent research has shown that ultrasound is a promising imaging method for breast cancer diagnosis. Various groups around the world work on the development of water bath scanning systems. Some of these systems have already been tested in a clinical setting [27], [107], [108]. With a water bath scanner, the breast is scanned from all sides, and transmission and reflection measurements are done simultaneously. Typically, three kind of images are generated; reflectivity, speed of sound, and attenuation images. Reflectivity images reveal the echogenicity of breast tissues. Whereas, speed of sound and attenuation images provide quantitative information about the acoustical properties of the various breast tissues. Consequently, tissue characterization and diagnosis can be done by combining these three images [35].

It is known that full-waveform inversion (FWI) is the best imaging method to generate accurate speed of sound images [31]. The main challange with FWI is the comutational costs required for solving the inverse problem. These computational costs are proportional with the size of the region of interest to be imaged. To reduce the size of the region of interest, we proposed a redatuming technique which is valid for a 2-D setup [101]. By redatuming the measured pressure field to the outer boundaries of the region of interest, computational domain becomes smaller and consequently the computational cost for FWI reduces. In this work, we extend this idea to 3-D. We use spherical Hankel functions to describe and back-propagate the measured pressure wave. We present the achieved computational gain by comparing the computation time for two cases; one where FWI is applied to the original region of interest, and second, where it is applied to a smaller region that is constructed after redatuming.

A.2. THEORY

Consider an unknown object within a finite spatial domain $\mathbb{D}$. A measurement domain $\mathbb{S}$ and a redatuming domain $\mathbb{S}'$ enclose the object. A position in the spatial domain $\mathbb{R}^3$ is denoted in Cartesian coordinates by the vector (x, y, z) and in spherical coordinates by the vector (r, θ, ϕ). All formulations are done in the temporal Fourier domain with angular frequency ω.

The pressure field $p\left(r,\theta,\phi,\omega\right)$ measured in $\mathbb{S}$ satisfies the 3-D Helmholtz equation, which reads in spherical coordinates [109]

$$\frac{1}{r^2}\frac{\partial}{\partial r}\left(r^2\frac{\partial p\left(r,\theta,\phi,\omega\right)}{\partial r}\right)+\frac{1}{r^2\sin(\theta)}\frac{\partial}{\partial\theta}\left(\sin(\theta)\frac{\partial p\left(r,\theta,\phi,\omega\right)}{\partial\theta}\right)+\frac{1}{r^2\sin^2(\theta)}\frac{\partial^2 p\left(r,\theta,\phi,\omega\right)}{\partial\phi^2}$$
$$+\frac{\omega^2}{c^2}p\left(r,\theta,\phi,\omega\right)=0. \tag{A.1}$$

Equation (A.1) can be solved using separation of variables, hence

$$p\left(r,\theta,\phi,\omega\right)=R\left(r,\omega\right)\Theta\left(\theta\right)\Phi\left(\phi\right). \tag{A.2}$$

Substituting equation (A.2) into (A.1) yields separate equations for $R\left(r,\omega\right)$, $\Theta\left(\theta\right)$ and $\Phi\left(\phi\right)$, namely [109]

$$\frac{\partial}{\partial r}\left(r^2\frac{\partial R\left(r,\omega\right)}{\partial r}\right)+\left[r^2\frac{\omega^2}{c^2}-n(n+1)\right]R\left(r,\omega\right)=0, \tag{A.3}$$

$$\frac{1}{\sin(\theta)}\frac{\partial}{\partial\theta}\left(\sin(\theta)\frac{\partial\Theta(\theta)}{\partial\theta}\right)+\left[n(n+1)-\left(\frac{m}{\sin(\theta)}\right)^2\right]\Theta(\theta)=0, \tag{A.4}$$

and

$$\frac{1}{\Phi(\phi)}\frac{\partial^2\Phi(\phi)}{\partial\phi^2}=-l^2, \tag{A.5}$$

with n and l constants.

Equation (A.3) is closely related to Bessel's differential equation and has the following solution

$$R_n(r,\omega)=b_{n,1}(\omega)h_n^{(1)}\left(\frac{\omega}{c}r\right)+b_{n,2}(\omega)h_n^{(2)}\left(\frac{\omega}{c}r\right), \tag{A.6}$$

where the spherical Hankel functions $h_n^{(1)}\left(\frac{\omega}{c}r\right)$ and $h_n^{(2)}\left(\frac{\omega}{c}r\right)$ represent inward and outward propagating waves, respectively. By positioning the origin of our coordinate system inside $\mathbb{S}$ and $\mathbb{S}'$ we know that the scattered field outside the contrast is only described by outward propagating waves. Consequently, all coefficients $b_{n,1}(\omega)$ are equal to zero.

Equation (A.4) is similar to the Legendre differential equation and has the following solution

$$\Theta_n(\theta)=b_{n,1}(\omega)P_n^l(\cos(\theta))+b_{n,2}(\omega)Q_n^l(\cos(\theta)), \tag{A.7}$$

where $P_n^l(\cos(\theta))$ and $Q_n^l(\cos(\theta))$ are associated Legendre functions of the first and second kind.

Equation (A.5) is a standard second-order differential equation whose solution equals

$$\Phi(\phi)=ae^{-il\phi}, \tag{A.8}$$

with arbitrary constant a and $-\pi<\phi\leq\pi$.

By combining equations (A.2), (A.6), (A.7) and (A.8) the solutions of equation (A.1) are equal to

$$p(r,\theta,\phi,\omega)=\sum_{n=-N}^{N}\sum_{l=-n}^{n}c_{nl}(\omega)h_n^{(2)}\left(\frac{\omega}{c}r\right)P_n^l(\cos\theta)e^{-il\phi}, \tag{A.9}$$

To find the complex valued coefficients $c_{nl}(\omega)$ of equation (A.9), the pressure field $p(r,\theta,\phi,\omega)$ is matched to the M measurements $d_m(\omega)$, where $d_m(\omega)$ is the field measured by the m^{th} receiver located on $\mathbb{S}$. Consequently, the unknown coefficients $c_{nl}(\omega)$ are obtained by solving the following system of equations

$$\sum_{n=-N}^{N}\sum_{l=-n}^{n}c_{nl}(\omega)h_n^{(2)}\left(\frac{\omega}{c}r\right)P_n^l(\cos\theta)e^{-il\phi}=d_m(\omega), \tag{A.10}$$

for all m.

Once the coefficients $c_{nl}(\omega)$ are found, the field can be computed at any location outside $\mathbb{D}$ using equation (A.10). In this way, we can redatum the wave field measured at $\mathbb{S}$ to the domain $\mathbb{S}'$.

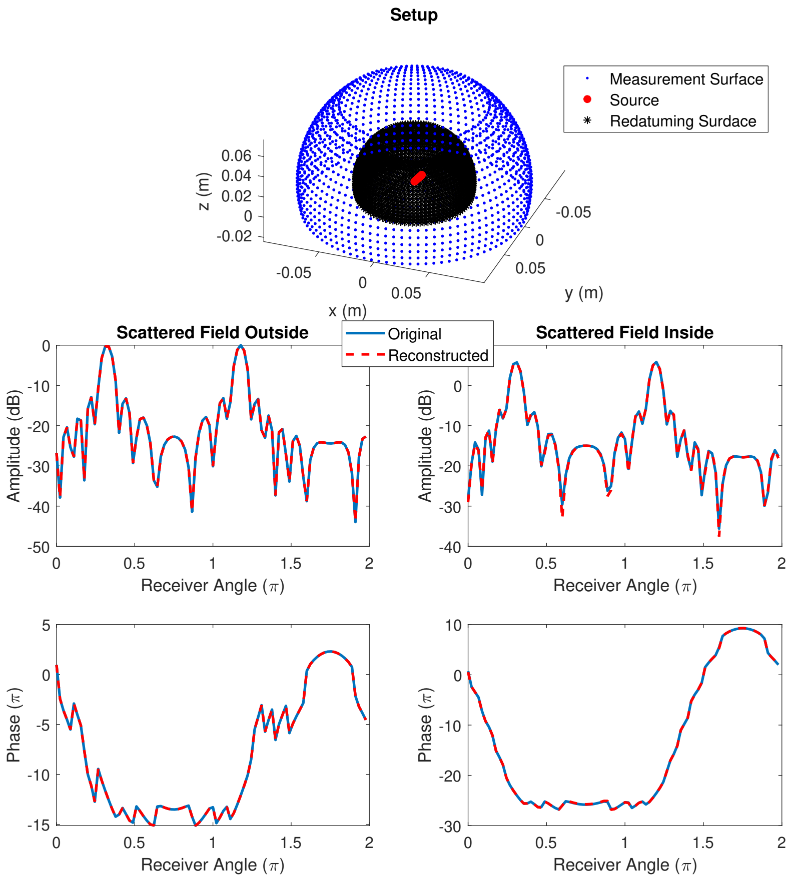

Figure A.1: A synthetic example showing results of the redatuming method. System geometry is given at the top. The amplitudes and phases of the measured (blue) and redatumed (red) wave fields are compared in the graphs below; left the fields at $R_1 = 0.1$ m and right at $R_2 = 0.05$ m.

A.3. RESULTS

The proposed redatuming method is tested using two synthetic examples. In the first example, we validate the proposed redatuming method by back-propagating the measured pressure field that is generated by an arbitrary source distribution. In the second example, we apply contrast source inversion (CSI) [73] on the measured data before and after redatuming.

A.3.1. VALIDATION

A source is constructed via an arbitrary collection of point sources, see Fig. A.1. This source generates a pressure field that is measured at two hemispheres with radii R_1 and R_2. Next,

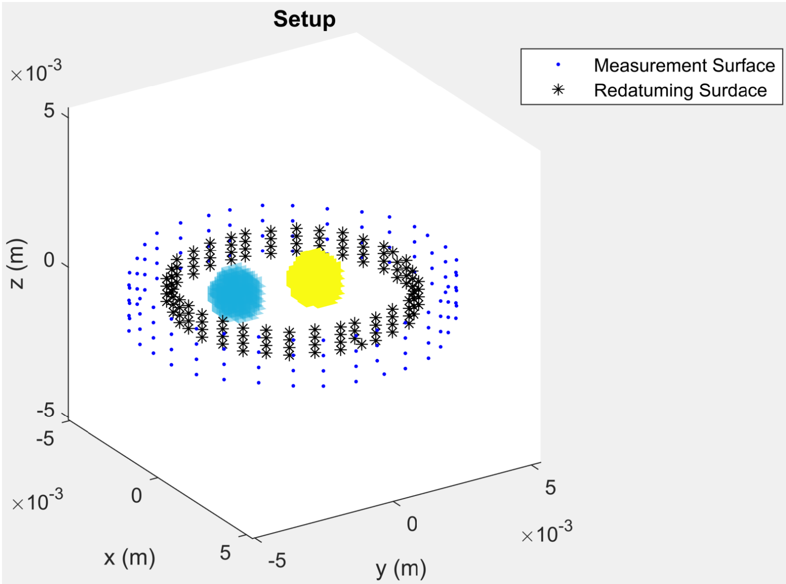

Figure A.2: System geometry of the inversion example.

the field measured at the outer hemisphere with radius R_1 is decomposed into spherical Hankel functions. This decomposed field is compared with its original measured field, see bottom left image in Fig. A.1. Next, the field measured at the hemisphere with radius R_1 is redatumed to a hemisphere with radius $R_2 < R_1$. A comparison of the redatumed and measured field at the hemisphere with radius R_2 is shown in the bottom right image. An excellent match between the original and redatumed wave fields is observed for both cases.

A.3.2. INVERSION

The forward problem is solved using a full-wave method [75] and the pressure field is measured at the measurement surface, see Fig. A.2. There are eight sources distributed equally on the circle with radius $r = 5$ mm in the plane $z = 0$. The central frequency of the wave transmitted by the source is 1 MHz. As illustrated in Fig. A.2, 128 receivers are located on the measurement surface. Two spherical objects are placed in the region of interest. One of them has a lower (1485 m/s) and the other one has a higher (1634 m/s) speed of sound value as compared to the homogeneous embedding (1524 m/s).

First, CSI is applied on the pressure field at the measurement surface. Next, CSI is applied on the redatumed pressure field. Reconstruction results for both geometries are presented in Fig. A.3. These images show the resulting reconstructions in the $z = 0$ plane. In both cases, CSI reconstructed the two spherical objects with an accurate location and diameter. The number of pixels in the region of interest is $42 \times 42 \times 42$ before and $32 \times 32 \times 32$ after redatuming. Hence, in this particular example, the computational load is reduced by 55 %. This means that the inversion after redatuming becomes approximately two times faster. Depending on the measurement setup and object of interest, the amount of reduction may vary.

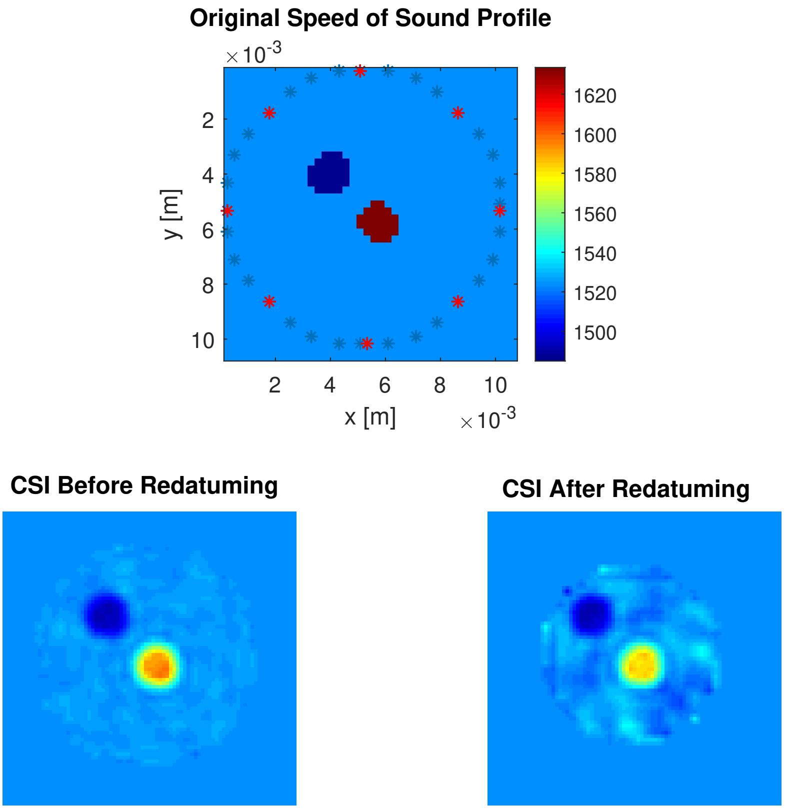

Figure A.3: Reconstruction results of CSI. System geometry is given at top. Red dots are the sources, and blue dots are the receivers located at $z = 0$ plane. Colorbar indicates speed of sound in m/s. CSI results before and after redatuming are given at the bottom images.

A.4. CONCLUSION

A new redatuming method for a 3-D environment based on Hankel function decomposition is presented. The method aims to reduce the spatial computational domain and hence the computation time for 3-D FWI. Results with two synthetic examples show that the proposed method is accurate and efficient. For the first example shown in this work, the radius of the hemisphere is reduced from $R_1 = 0.1$ m to $R_2 = 0.05$ m. This reduces the size of the domain of interest and hence the computational load for inversion by a factor eight. For the second example, FWI is applied to the measured and redatumed data. Similar reconstruction results are obtained for the redatumed case as compared to the original situation.

In this work, we only focus on the computational gain that is achieved with redatuming. In practice, redatuming brings more advantages. First, with the ability of redatuming to any point in the embedding, the measurement geometry can be altered. This can be useful for applying different kinds of imaging and inversion methods optimized for a specific geometry. Second, redatuming acts as a filter on the pressure field so it can be used to remove noise from the measured data. Third, it may lead to an improved convergence as is observed with solving the forward problem [60]. Finally, the particle velocity can be computed with this method which can be useful for inversion of mass density [100].

B

Appendix B: Wavelet Regularized Born Inversion[1]

Breast ultrasound is gaining interest as an alternative to mammography. To improve its diagnostic value, full waveform inversion (FWI) methods are developed. These methods aim for reconstructing speed of sound maps of the breast. When the inversion is performed in the frequency domain, computation time is reduced by limiting the number of frequency components at the cost of retrieving noisy images. To compensate for the lack of frequency information and to reduce the noise in the reconstruction, we propose two solutions. First, we select the frequency components randomly out of the entire available bandwidth for each source-receiver combination separately. Next, a regularization method is applied that takes advantage of the sparseness of the reconstructed contrast in the wavelet domain.

[1] This chapter has been published as:
Bouchan, Taskin and van Dongen, "Wavelet Regularized Born Inversion," IUS, IEEE, 2019.
The text and notation used in this chapter may differ on minor details from the actual publication. This is done to achieve consistency between chapters and will especially be the case for the section Theory.

B

B.1. Introduction

Breast cancer is the most frequently diagnosed cancer among women. Detecting it at an early stage enables to significantly reduce the mortality rate [110]. Currently, mammography is the gold standard for screening. Unfortunately, it has some disadvantages, among which the difficulty to scan women with dense breasts. Ultrasound is a promising alternative enabling safe and fast diagnosis [10]. To ease the differention between malignant and benign tissues, waveform inversion methods have become of interest. With these methods speed of sound profiles of the breast are reconstructed [31].

When applying waveform inversion in the frequency domain, special attention is given to the selection of frequency components. It is common practice to select only a limited number of frequency components from the available bandwidth to reduce computation time [111], [112]. Another common practice is reffered to as frequency-hopping [113], which may be useful to avoid local minima (see also chapter 4 of this thesis).

To improve on convergence, regularization is employed when solving the inverse problem. The most common regularization techniques are related to the total variation [76] in and sparsity [105] of the reconstruction. Regularization is an important tool to stabilize the inversion.

In this appendix, regularized frequency domain Born inversion is investigated [114], [115]. To improve its convergence, the frequencies used for the inversion are chosen randomly over the available bandwidth for each source receiver combination, at the expense of additional noise in the reconstruction. To regularize the inverse problem and to reduce the amount of noise in the reconstruction, the sparsity constraint for the reconstruction in the wavelet domain is utilized. To test and validate Born inversion in combination with sparsity based regularization, a study has been performed using synthetic and real data.

B.2. Theory

The acoustic pressure field $\hat{p}(\boldsymbol{x})$, where $\boldsymbol{x}$ denotes a position in the two-dimensional spatial domain $\mathbb{D}$ and ω is the angular frequency, can be decomposed into an incident field $\hat{p}^{inc}(\boldsymbol{x})$ that is generated by the source and propagates in the homogeneous embedding, and a scattered field $\hat{p}^{sct}(\boldsymbol{x})$ that equals

$$\hat{p}^{sct}(\boldsymbol{x}) = \omega^2 \int_{\boldsymbol{x}'\in\mathbb{D}} \hat{G}(\boldsymbol{x}-\boldsymbol{x}')\chi(\boldsymbol{x}')\hat{p}(\boldsymbol{x}')dV, \tag{B.1}$$

where $\hat{G}(\boldsymbol{x}-\boldsymbol{x}')$ is the Green's function and $\chi(\boldsymbol{x}')$ is the contrast function given by

$$\chi(\boldsymbol{x}') = \frac{1}{c^2(\boldsymbol{x}')} - \frac{1}{c_0^2}, \tag{B.2}$$

where $c(\boldsymbol{x}')$ and c_0 are the speed of sound of the actual medium and of the homogeneous embedding respectively. Under the weak scattering approximation, the pressure field inside integral equation (B.1) can be replaced by the incident field, hence

$$\hat{p}^{sct}(\boldsymbol{x}) = \omega^2 \int_{\boldsymbol{x}'\in\mathbb{D}} \hat{G}(\boldsymbol{x}'-\boldsymbol{x}')\chi(\boldsymbol{x}')\hat{p}^{inc}(\boldsymbol{x}')dV. \tag{B.3}$$

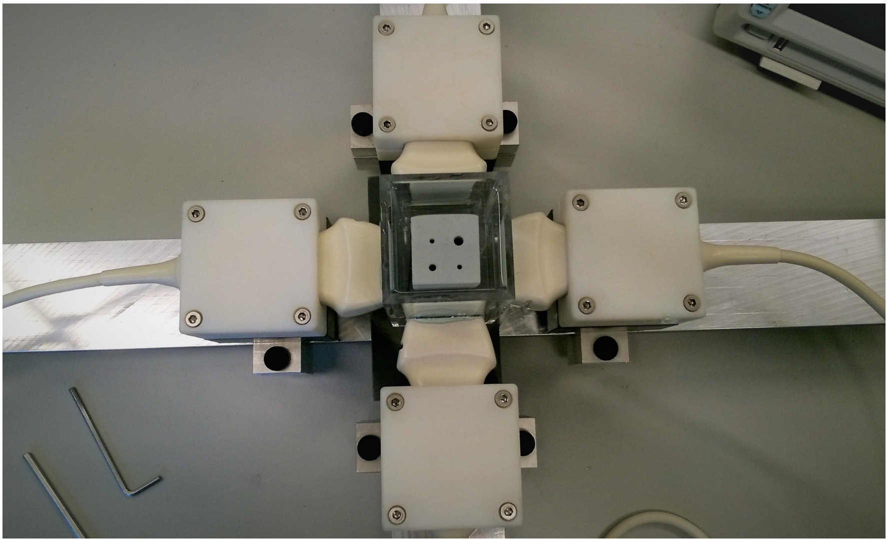

Figure B.1: Measurement setup.

This linearisation is known as the Born approximation. The unknown contrast function $\chi(\boldsymbol{x}')$ can be found by solving the minimization problem

$$\min_\chi \left\|\mathbf{d} - \mathrm{M}[\chi]\right\|^2, \tag{B.4}$$

where $\mathbf{d}$ is the measured scattered field and M is an operator representing integral formulation (B.3). To find the contrast function $\chi(\boldsymbol{x}')$, equation (B.4) is minimized using an iterative optimization method [114].

B.2.1. FREQUENCY SELECTION

The minimization problem in equation (B.4) can be solved for different frequencies independently. In this work, we randomly select a unique set of frequencies for each source-receiver combination. By doing this, the computation time is reduced and information from the entire available bandwidth is included in the reconstruction. However, limiting the total amount of data used for the reconstruction leads to an increase of the amount of noise in the reconstruction.

B.2.2. WAVELET DOMAIN REGULARIZATION

Wavelet domain regularization is used to filter the noise introduced by the random frequency selection. This noise has no spatial correlation and is represented by many coefficients with low intensity in the wavelet domain. At the same time, the image is often structured and may well be represented with only a few coefficients with a high amplitude in the wavelet domain. By applying a hard threshold in the wavelet domain, it is possible to filter out the noise. With the thresholding constraint, the minimization problem of interest becomes

$$\min_\chi \left\|\mathbf{d} - \mathrm{M}[\chi]\right\|^2 \quad s.t. \quad \left\|\psi[\chi]\right\|_0 < \alpha, \tag{B.5}$$

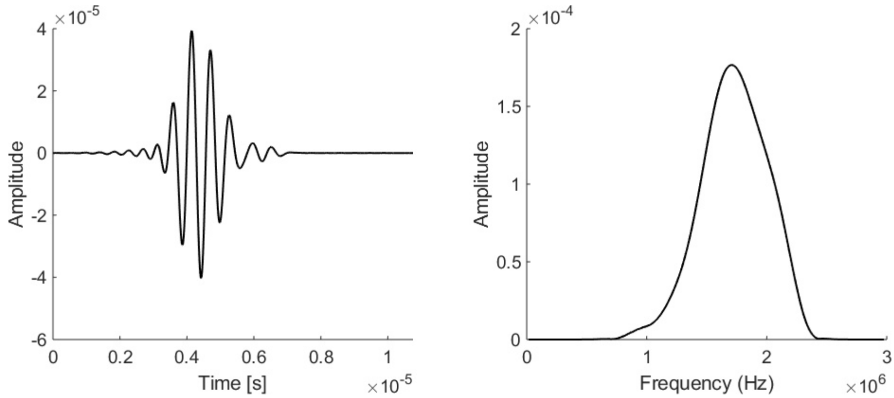

Figure B.2: Source excitation profile in time (left) and frequency (right) domain.

where ψ is the multidimensional wavelet transform and α is the threshold value. Because we use a 2-D inversion method in this work, the wavelet transform is 2-D as well and it is applied to all spatial dimensions.

B.3. Results

B.3.1. Configuration

To acquire real data, four Philips P4-1 probes connected to a Verasonics Vantage 256 device are used. Each probe contains a linear array of 96 elements and is fixed in a holder during the measurement. The water tank has dimensions of 45 mm × 45 mm and contains an agar based phantom [116]. The phantom has dimensions of 26 mm × 29 mm and includes holes with diameters of 2 mm, 3 mm and 4 mm, see Fig. B.1.

First, an empty measurement, where the tank is only filled with water, is done to calibrate the system. From this empty measurement the incident field and the excitation pulse is retrieved. The excitation pulse has a center frequency of 1.5 MHz. The measured wavelet and its spectrum are shown in Fig. B.2. Next, a measurement with the phantom placed in the tank is done. The scattered field is obtained by subtracting the empty measurement from the phantom measurement.

A synthetic data set is generated by using a forward modelling method based on a frequency domain integral equation formulation [75]. The synthetic setup is designed to mimic the real measurement setup. The synthetic data is useful to evaluate the reconstruction method as it represents the ideal noise-free data for which the ground truth is known.

B.3.2. Randomizing

Within a predefined bandwidth, the same number of frequency components is randomly picked for each source-receiver combination. In the end, all frequencies from the available bandwidth are used in the same proportion. This is different from the commonly applied selection method, where the same frequency components are selected for all source-

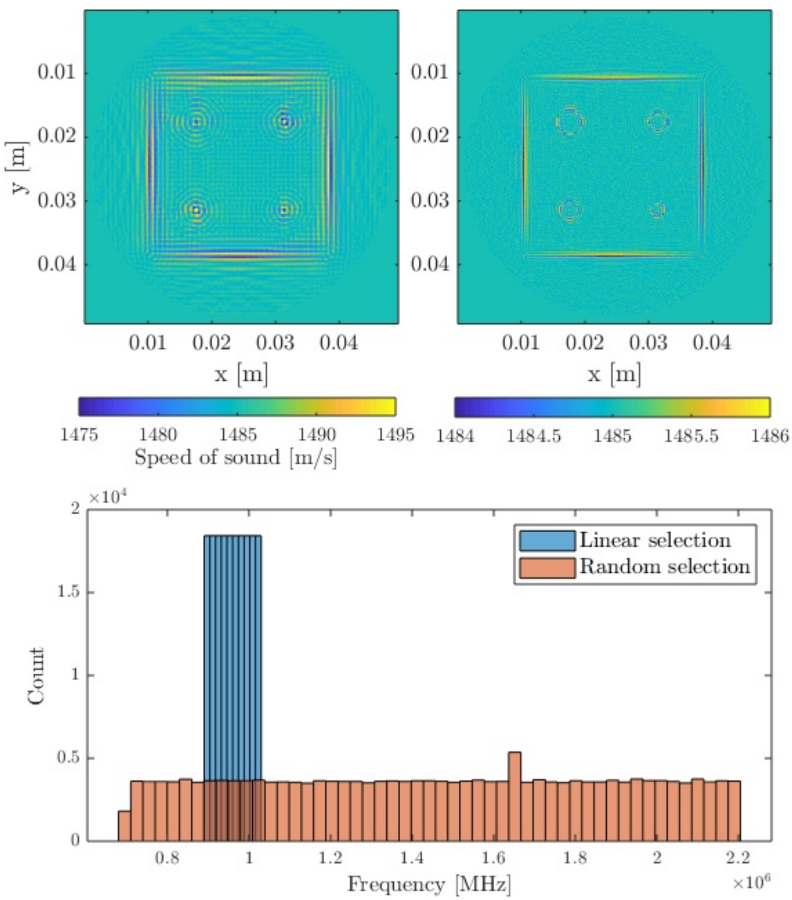

Figure B.3: Difference between linear and random selection of the frequencies. For both reconstructions only ten frequency components from the available synthetic data are used, with synthetic data and only reflection signals. (Left) The ten frequency components are selected out of the same narrow band (0.9 - 1.05 MHz) for all source-receiver combination. (Right) The ten frequency components are selected randomly for each source-receiver combination out of the available bandwidth (0.7 - 2.2 MHz). (Bottom) Histogram of frequency selection for both approaches.

receiver combinations. Unfortunately, the latter technique does not allow for a wide coverage of the available bandwidth leading to a reconstruction of lower quality. Fig. B.3 shows the difference in the reconstruction for those two techniques. Although the amplitudes of both images are not the same, the reconstruction with the random frequency selection has a better quality; it has sharper edges and shows less ringing effect and therefore leads to a better reconstruction of the holes. Fig. B.3 also shows a histogram of the selected frequencies for the two methods.

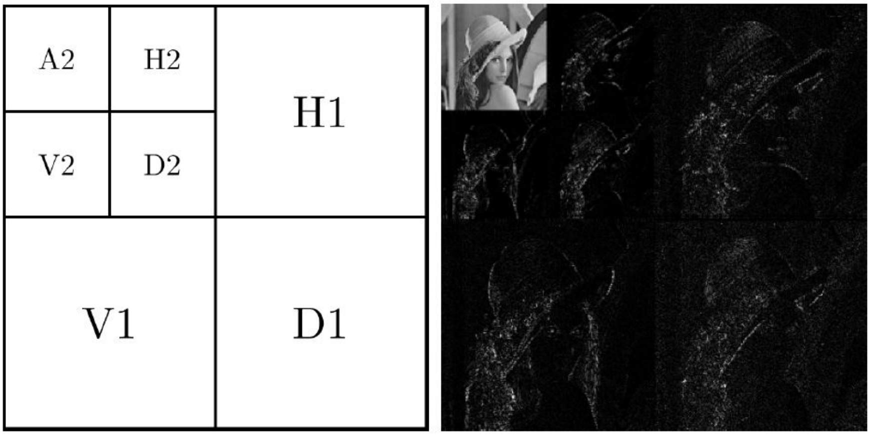

Figure B.4: Structure of the 2-D wavelet transform (left) and wavelet transform of Lena at level 2 using Daubechies 4 wavelet (right).

B.3.3. WAVELET DOMAIN REGULARIZATION

A wavelet transform example is presented in Fig. B.4. Here a two-level wavelet transform is performed on the well known Lena image using the commonly used Daubechies 4 wavelet. The first level gives four images of half the size of the initial image, which are the approximation (A1), horizontal (H1), vertical (V1) and diagonal (D1) details. To achieve a higher level decomposition the same scheme is applied on A1, to give A2, H2, V2, and D2. Fig. B.4 presents the layout of those details. As can be seen the discrete wavelet transform is a one-to-one transformation, which means that the number of elements is conserved throughout the transformation. A majority of the coefficients have low amplitudes. Consequently, the information contained in the original image in the Cartesian domain is represented by only a few dominating coefficients in the wavelet domain. This is important for the use of this basis as a regularization tool.

B.3.4. BORN INVERSION RESULTS

Born inversion with and without wavelet regularization are tested on synthetic and real data and compared with each other. The results are presented for reflections and transmissions measurements separately. A reflection image is produced by using only the data received by the probe containing the source. A transmission image is created from data received by the probe facing the source. All images are the result of Born inversion for ten frequencies randomly picked out of the bandwidth 0.7 - 2.2 MHz, and 16 iterations.

Results obtained with Born inversion with the synthetic data-set are presented in Fig. B.5. The color scale is the same for all images. The regularization method does not change the shape of the phantom but it does change the contrast and therefore the amplitude of the reflections. This phenomena does not appear in the reconstruction using transmission data only, where it would lead to errors in the speed of sound reconstruction. The thresholding method clearly denoises the image without affecting the shape of the phantom. Only the highest 2% of the coefficients have been used. This thresholding

B

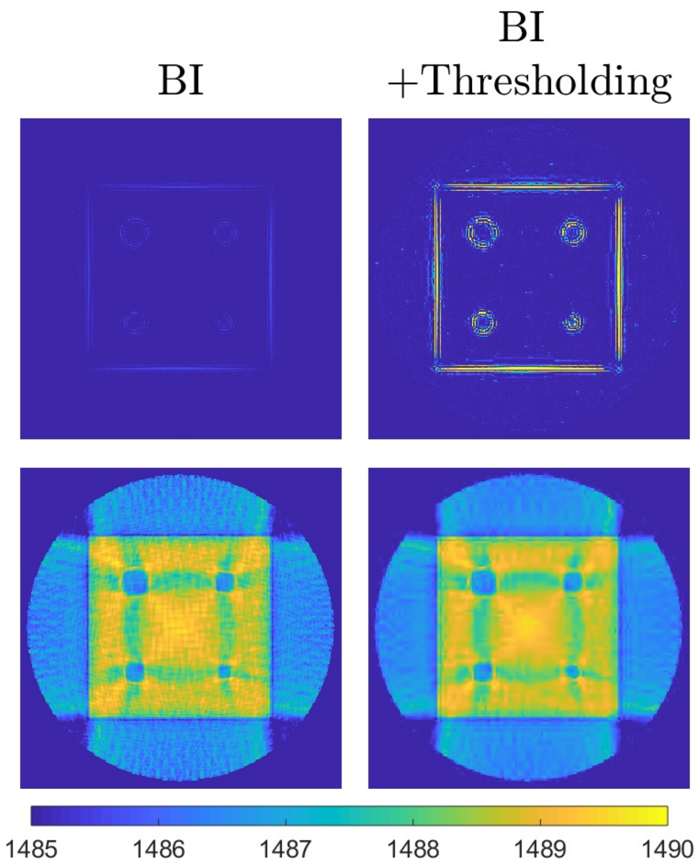

Figure B.5: Born inversion results for the synthetic data-set. The top row shows the reconstruction obtained with reflection measurements. The bottom row shows the reconstruction obtained with transmission measurements.

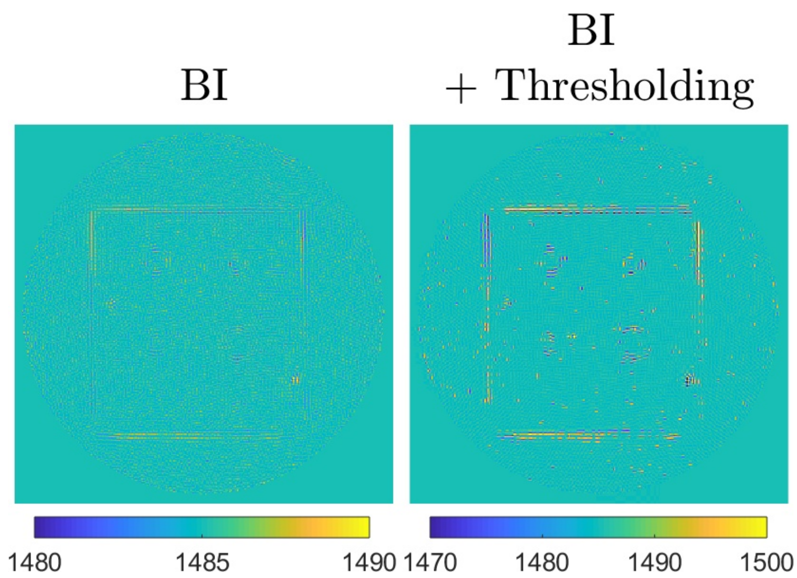

Figure B.6: Born inversion results for real measurement data. The reconstructions are obtained with reflection measurements.

is performed from the 7th iteration onwards. In this way a good estimation of the reconstruction is obtained before applying a regularization which may change the shape of the contrast.

The reconstructions for measurement data are presented in Fig. B.6. The colorbars are different for the two reconstructions to enhance the main characteristic of each reconstruction. With Born inversion without regularization, the contrast of the boundary of the holes is low and it is hard to distinguish them. With the regularized Born inversion method the holes become clearly visible. After thresholding, the noise is reduced with the boundaries preserved.

Fig. B.7 shows the result of Born inversion with a varying proportion of coefficients being retained. The performance of the denoising process is optimal when the noise is reduced while the structure of the object remains unchanged.

B.4. CONCLUSION

A new method to improve the performance of Born inversion is presented. It combines random frequency selection with hard thresholding of the contrast in the wavelet domain. The method has been successfully tested on both synthetic and real measurements and has shown to reconstruct the object with a better accuracy than traditional Born inversion.

Although not tested, the proposed methods are expected to work especially well in combination with interface contrast imaging, which aims for reconstructing reflectivity images [117], [118].

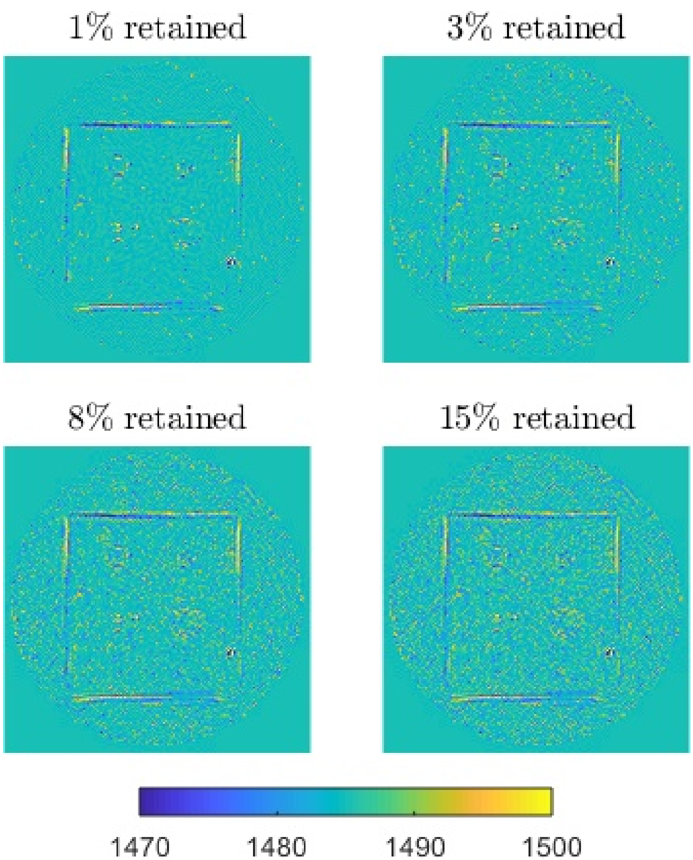

Figure B.7: Comparison of the results of Born inversion for different percentages of the coefficients retained.

Bibliography

[1] M. Heron, "Deaths: Leading causes for 2017.", *National Vital Statistics Reports: From the Centers for Disease Control and Prevention, National Center for Health Statistics, National Vital Statistics System*, vol. 68, no. 6, pp. 1–77, 2019.

[2] WHO, "Disease burden and mortality estimates", *Geneva: WHO*, 2018.

[3] F. Bray, J. Ferlay, I. Soerjomataram, R. L. Siegel, L. A. Torre, and A. Jemal, "Global cancer statistics 2018: Globocan estimates of incidence and mortality worldwide for 36 cancers in 185 countries", *CA: a cancer journal for clinicians*, vol. 68, no. 6, pp. 394–424, 2018.

[4] RIVM, *Breast cancer in the netherlands*, https://www.rivm.nl/en/breast-cancer-screening-programme/breast-cancer-in-netherlands, Accessed: 2020-06-30.

[5] WHO, *Top 10 causes of death*, https://www.who.int/gho/mortality_burden_disease/causes_death/top_10/en, Accessed: 2020-06-30.

[6] S. Winters, C. Martin, D. Murphy, and N. K. Shokar, "Breast cancer epidemiology, prevention, and screening", in *Progress in Molecular Biology and Translational Science*, vol. 151, Elsevier, 2017, pp. 1–32.

[7] G. Carioli, M. Malvezzi, T. Rodriguez, P. Bertuccio, E. Negri, and C. La Vecchia, "Trends and predictions to 2020 in breast cancer mortality in europe", *The Breast*, vol. 36, pp. 89–95, 2017.

[8] SEER, *Survival rates by time since diagnosis, 2000-2016*, https://seer.cancer.gov/explorer/application.html, Accessed: 2020-09-29.

[9] I. Ljuslinder, "Studies of lrig1 and the erbb receptor family in breast and colorectal cancer", PhD thesis, Umeå universitet, 2009.

[10] J. Geisel, M. Raghu, and R. Hooley, "The role of ultrasound in breast cancer screening: The case for and against ultrasound", in *Seminars in Ultrasound, CT and MRI*, Elsevier, vol. 39, 2018, pp. 25–34.

[11] C. M. Checka, J. E. Chun, F. R. Schnabel, J. Lee, and H. Toth, "The relationship of mammographic density and age: Implications for breast cancer screening", *American Journal of Roentgenology*, vol. 198, no. 3, W292–W295, 2012.

[12] R. Guo, G. Lu, B. Qin, and B. Fei, "Ultrasound imaging technologies for breast cancer detection and management: A review", *Ultrasound in Medicine & Biology*, vol. 44, no. 1, pp. 37–70, 2018.

[13] N. F. Boyd, H. Guo, L. J. Martin, L. Sun, J. Stone, E. Fishell, R. A. Jong, G. Hislop, A. Chiarelli, S. Minkin, *et al.*, "Mammographic density and the risk and detection of breast cancer", *New England Journal of Medicine*, vol. 356, no. 3, pp. 227–236, 2007.

[14] W. A. Berg, J. D. Blume, A. M. Adams, R. A. Jong, R. G. Barr, D. E. Lehrer, E. D. Pisano, W. P. Evans III, M. C. Mahoney, L. Hovanessian Larsen, *et al.*, "Reasons women at elevated risk of breast cancer refuse breast mr imaging screening: Acrin 6666", *Radiology*, vol. 254, no. 1, pp. 79–87, 2010.

[15] D. Thigpen, A. Kappler, and R. Brem, "The role of ultrasound in screening dense breasts—a review of the literature and practical solutions for implementation", *Diagnostics*, vol. 8, no. 1, p. 20, 2018.

[16] L. Chen, Y. Chen, X.-H. Diao, L. Fang, Y. Pang, A.-Q. Cheng, W.-P. Li, and Y. Wang, "Comparative study of automated breast 3-d ultrasound and handheld b-mode ultrasound for differentiation of benign and malignant breast masses", *Ultrasound in Medicine & Biology*, vol. 39, no. 10, pp. 1735–1742, 2013.

[17] G. Glover, "Characterization of in vivo breast tissue by ultrasonic time-of-flight computed tomography", in *Natl Bur Stand Int Symp Ultrason Tissue Characterization, National Science Foundation, Ultrasonic Tissue Characterization II*, 1979, pp. 221–225.

[18] G. H. Glover, "Computerized time-of-flight ultrasonic tomography for breast examination", *Ultrasound in Medicinde & Biology*, vol. 3, no. 23, pp. 117–127, 1977.

[19] P. L. Carson, T. V. Oughton, W. R. Hendee, and A. S. Ahuja, "Imaging soft tissue through bone with ultrasound transmission tomography by reconstruction", *Medical Physics*, vol. 4, no. 4, pp. 302–309, 1977.

[20] P. L. Carson, C. R. Meyer, A. L. Scherzinger, and T. V. Oughton, "Breast imaging in coronal planes with simultaneous pulse echo and transmission ultrasound", *Science*, vol. 214, pp. 213–215, 1981.

[21] J. F. Greenleaf and R. C. Bahn, "Clinical imaging with transmissive ultrasonic computerized tomography", *IEEE Transactions on Biomedical Engineering*, no. 2, pp. 177–185, 1981.

[22] J. F. Greenleaf, "Computerized tomography with ultrasound", *Proc. IEEE*, vol. 71, no. 3, pp. 330–337, 1983.

[23] M. Birk, E. Kretzek, P. Figuli, M. Weber, J. Becker, and N. V. Ruiter, "High-speed medical imaging in 3d ultrasound computer tomography", *IEEE Transactions on Parallel and Distributed Systems*, vol. 27, no. 2, pp. 455–467, 2016.

[24] N. Ruiter, M. Zapf, R. Dapp, T. Hopp, W. Kaiser, and H. Gemmeke, "First results of a clinical study with 3d ultrasound computer tomography", in *Ultrasonics Symposium (IUS), 2013 IEEE International*, IEEE, 2013, pp. 651–654.

[25] H. Gemmeke and N. Ruiter, "3d ultrasound computer tomography for medical imaging", *Nuclear Instruments and Methods in Physics Research Section A: Accelerators, Spectrometers, Detectors and Associated Equipment*, vol. 580, no. 2, pp. 1057–1065, 2007.

[26] N. Duric, P. Littrup, L. Poulo, A. Babkin, R. Pevzner, E. Holsapple, O. Rama, and C. Glide, "Detection of breast cancer with ultrasound tomography: First results with the computed ultrasound risk evaluation (cure) prototype", *Medical Physics*, vol. 34, no. 2, pp. 773–785, 2007.

[27] J. Wiskin, D. Borup, M. Andre, S. Johnson, J. Greenleaf, Y. Parisky, and J. Klock, “Three-dimensional nonlinear inverse scattering: Quantitative transmission algorithms, refraction corrected reflection, scanner design, and clinical results”, *The Journal of the Acoustical Society of America*, vol. 133, no. 5, pp. 3229–3229, 2013.

[28] L. Guasch, O. C. Agudo, M.-X. Tang, P. Nachev, and M. Warner, “Full-waveform inversion imaging of the human brain”, *NPJ Digital Medicine*, vol. 3, no. 1, pp. 1–12, 2020.

[29] S. Bernard, V. Monteiller, D. Komatitsch, and P. Lasaygues, “Ultrasonic computed tomography based on full-waveform inversion for bone quantitative imaging”, *Physics in Medicine & Biology*, vol. 62, no. 17, p. 7011, 2017.

[30] E. Kretzek and N. Ruiter, “Gpu based 3d saft reconstruction including phase aberration”, in *Medical Imaging 2014: Ultrasonic Imaging and Tomography*, International Society for Optics and Photonics, vol. 9040, 2014, 90400W.

[31] N. Ozmen, R. Dapp, M. Zapf, H. Gemmeke, N. V. Ruiter, and K. W. A. van Dongen, “Comparing different ultrasound imaging methods for breast cancer detection”, *IEEE Transactions on Ultrasonics, Ferroelectrics, and Frequency Control*, vol. 62, no. 4, pp. 637–646, 2015.

[32] J. Jago and T. Whittingham, “Experimental studies in transmission ultrasound computed tomography”, *Physics in Medicine & Biology*, vol. 36, no. 11, p. 1515, 1991.

[33] T. Hopp, F. Zuch, P. Comby, and N. Ruiter, “Fat ray ultrasound transmission tomography: Preliminary experimental results with simulated data”, in *Medical Imaging 2020: Ultrasonic Imaging and Tomography*, International Society for Optics and Photonics, vol. 11319, 2020, p. 113190M.

[34] S. Li, M. Jackowski, D. P. Dione, T. Varslot, L. H. Staib, and K. Mueller, “Refraction corrected transmission ultrasound computed tomography for application in breast imaging”, *Medical Physics*, vol. 37, no. 5, pp. 2233–2246, 2010.

[35] B. Malik, J. Klock, J. Wiskin, and M. Lenox, “Objective breast tissue image classification using quantitative transmission ultrasound tomography”, *Scientific Reports*, vol. 6, p. 38 857, 2016.

[36] A. B. Ramirez, S. A. Abreo, and K. W. A. van Dongen, “Selecting the number and location of sources and receivers for non-linear time-domain inversion”, in *2017 IEEE International Ultrasonics Symposium (IUS)*, IEEE, 2017, pp. 1–3.

[37] J. Virieux and S. Operto, “An overview of full-waveform inversion in exploration geophysics”, *Geophysics*, vol. 74, no. 6, WCC1–WCC26, 2009.

[38] G. Y. S. Sandhu, C. Li, O. Roy, S. Schmidt, and N. Duric, “High-resolution quantitative whole-breast ultrasound: In vivo application using frequency-domain waveform tomography”, in *Medical Imaging 2015: Ultrasonic Imaging and Tomography*, International Society for Optics and Photonics, vol. 9419, 2015, p. 94190D.

[39] R. L. Siegel, K. D. Miller, S. A. Fedewa, D. J. Ahnen, R. G. Meester, A. Barzi, and A. Jemal, “Colorectal cancer statistics, 2017”, *CA: a Cancer Journal for Clinicians*, vol. 67, no. 3, pp. 177–193, 2017.

[40] R. E. Bird, T. W. Wallace, and B. C. Yankaskas, "Analysis of cancers missed at screening mammography", *Radiology*, vol. 184, no. 3, pp. 613–617, 1992.

[41] N. V. Ruiter, G. F. Schwarzenberg, M. Zapf, R. Liu, R. Stotzka, and H. Gemmeke, "3D ultrasound computer tomography: Results with a clinical breast phantom", in *Ultrasonics Symposium (IUS), 2006 IEEE*, 2006.

[42] J. Wiskin, D. T. Borup, S. A. Johnson, and M. Berggren, "Non-linear inverse scattering: High resolution quantitative breast tissue tomography", *The Journal of the Acoustical Society of America*, vol. 131, no. 5, pp. 3802–3813, 2012.

[43] F. Simonetti, L. Huang, N. Duric, and O. Rama, "Imaging beyond the Born approximation: An experimental investigation with an ultrasonic ring array", *Physical Review E*, vol. 76, no. 3, pp. 036 601–10, 2007.

[44] M. C. Hesse and G. Schmitz, "Comparison of linear and nonlinear unidirectional imaging approaches in ultrasound breast imaging", in *Ultrasonics Symposium (IUS), 2012 IEEE International*, IEEE, 2012, pp. 1295–1298.

[45] R. Jirik, I. Peterlik, N. Ruiter, J. Fousek, R. Dapp, M. Zapf, and J. Jan, "Sound-speed image reconstruction in sparse-aperture 3-d ultrasound transmission tomography", *IEEE Transactions on Ultrasonics, Ferroelectrics, and Frequency Control*, vol. 59, no. 2, 2012.

[46] K. W. A. van Dongen and W. M. D. Wright, "A forward model and conjugate gradient inversion technique for low-frequency ultrasonic imaging", *J. Acoust. Soc. Am.*, vol. 120, no. 4, pp. 2086–2095, 2006.

[47] N. Ozmen-Eryilmaz, L. Demi, E. J. Alles, M. D. Verweij, and K. W. A. van Dongen, "Modeling acoustic wave field propagation in 3D breast models", in *Ultrasonics Symposium (IUS), 2011 IEEE International*, 2011, pp. 1700–1703.

[48] J. F. Bakker, M. M. Paulides, I. Obdeijn, G. C. van Rhoon, and K. W. A. van Dongen, "An ultrasound cylindrical phased-array for deep heating in the breast: Theoretical design using heterogeneous models", *Physics in Medicine & Biology*, vol. 54, pp. 3201–3215, 2009.

[49] R. Hardin and F. Tappert, "Applications of the split-step fourier method to the numerical solution of nonlinear and variable coefficient wave equations", *Siam Review*, no. 15, p. 423, 1973.

[50] A. C. Kak and M. Slaney, *Principles of computerized tomographic imaging*. SIAM, 1988, vol. 33.

[51] R. S. C. Cobbold, *Foundations of biomedical ultrasound*. Oxford University Press New York, 2007.

[52] G. C. Herman and P. M. van den Berg, "A least-square iterative technique for solving time-domain scattering problems", *The Journal of the Acoustical Society of America*, vol. 72, no. 6, pp. 1947–1953, 1982.

[53] R. E. Kleinman and P. M. van den Berg, "Iterative methods for solving integral equations", *Radio Science*, vol. 26, no. 1, pp. 175–181, 1991.

[54] J. T. Fokkema and P. M. van den Berg, *Seismic applications of acoustic reciprocity*. Elsevier, 2013.

[55] D. Gisolf and E. Vershuur, *The principles of quantitative acoustical imaging*. EAGE Publications bv, 2010.

[56] L. Demi, K. W. A. van Dongen, and M. D. Verweij, “A contrast source method for nonlinear acoustic wave fields in media with spatially inhomogeneous attenuation”, *The Journal of the Acoustical Society of America*, vol. 129, no. 3, pp. 1221–1230, 2011.

[57] J. Huijssen, M. D. Verweij, and N. de Jong, “Green’s function method for modeling nonlinear three-dimensional pulsed acoustic fields in diagnostic ultrasound including tissue-like attenuation”, in *Ultrasonics Symposium (IUS), 2008 IEEE International*, 2008, pp. 375–378.

[58] T. L. Szabo, “Causal theories and data for acoustic attenuation obeying a frequency power law”, *The Journal of the Acoustical Society of America*, vol. 97, no. 1, pp. 14–24, 1995.

[59] E. J. Alles and K. W. A. van Dongen, “Perfectly matched layers for frequency-domain integral equation acoustic scattering problems”, *IEEE Transactions on Ultrasonics, Ferroelectrics, and Frequency Control*, vol. 58, no. 5, pp. 1077–1086, 2011.

[60] K. W. A. van Dongen, C. Brennan, and W. M. Wright, “Reduced forward operator for electromagnetic wave scattering problems”, *IET Science, Measurement & Technology*, vol. 1, no. 1, pp. 57–62, 2007.

[61] R. Fletcher, “Conjugate gradient methods for indefinite systems”, in *Numerical analysis*, Springer, 1976, pp. 73–89.

[62] P. Zwamborn and P. M. van den Berg, “The three-dimensional weak form of the conjugate gradient FFT method for solving scattering problems”, *IEEE Transactions on Microwave Theory and Techniques*, vol. 40, no. 9, pp. 1757–1766, 1992.

[63] F. Dagrau, M. Rénier, R. Marchiano, and F. Coulouvrat, “Acoustic shock wave propagation in a heterogeneous medium: A numerical simulation beyond the parabolic approximation”, *The Journal of the Acoustical Society of America*, vol. 130, no. 1, pp. 20–32, 2011.

[64] P. Stoffa, J. T. Fokkema, R. de Luna Freire, and W. Kessinger, “Split-step fourier migration”, *Geophysics*, vol. 55, no. 4, pp. 410–421, 1990.

[65] I. Lecomte, P. L. Lavadera, I. Anell, S. J. Buckley, D. W. Schmid, and M. Heeremans, “Ray-based seismic modeling of geologic models: Understanding and analyzing seismic images efficiently”, *Interpretation*, vol. 3, no. 4, SAC71–SAC89, 2015.

[66] E. Skudrzyk, *The foundations of acoustics: basic mathematics and basic acoustics*. Springer Science & Business Media, 2012.

[67] T. L. Szabo, *Diagnostic ultrasound imaging: inside out*. Academic Press, 2004.

[68] S. Goss, R. Johnston, and F Dunn, “Compilation of empirical ultrasonic properties of mammalian tissues. ii”, *The Journal of the Acoustical Society of America*, vol. 68, no. 1, pp. 93–108, 1980.

[69] F. d'Astous and F. Foster, "Frequency dependence of ultrasound attenuation and backscatter in breast tissue", *Ultrasound in Medicine & Biology*, vol. 12, no. 10, pp. 795–808, 1986.

[70] F. A. Duck, *Physical properties of tissues: a comprehensive reference book*. Academic press, 2013.

[71] B. Sohrab, G. Farzan, B. Ashkan, and J. Amin, "Ultrasound thermotherapy of breast: Theoretical design of transducer and numerical simulation of procedure", *Japanese Journal of Applied Physics*, vol. 45, no. 3R, p. 1856, 2006.

[72] N. Duric, P. Littrup, S. Schmidt, C. Li, O. Roy, L. Bey-Knight, R. Janer, D. Kunz, X. Chen, J. Goll, *et al.*, "Breast imaging with the softvue imaging system: First results", in *Medical Imaging 2013: Ultrasonic Imaging, Tomography, and Therapy*, International Society for Optics and Photonics, vol. 8675, 2013, 86750K.

[73] P. M. van den Berg and A. Abubakar, "Contrast source inversion method: State of art", *Progress in Electromagnetic Research*, vol. 34, pp. 189–218, 2001.

[74] A. B. Ramirez and K. W. A. van Dongen, "Can sources and receivers be interchanged for imaging?", in *2016 IEEE International Ultrasonics Symposium (IUS)*, IEEE, 2016, pp. 1–4.

[75] U. Taskin, N. Ozmen, H. Gemmeke, and K. W. A. van Dongen, "Modeling breast ultrasound; on the applicability of commonly made approximations", *Archives of Acoustics*, vol. 43, 2018.

[76] A. B. Ramirez and K. W. A. van Dongen, "Sparsity constrained contrast source inversion", *The Journal of the Acoustical Society of America*, vol. 140, no. 3, pp. 1749–1757, 2016.

[77] P. B. Gordon and S. L. Goldenberg, "Malignant breast masses detected only by ultrasound. a retrospective review", *Cancer*, vol. 76, no. 4, pp. 626–630, 1995.

[78] M. Pérez-Liva, J. Herraiz, J. Udías, E. Miller, B. Cox, and B. Treeby, "Time domain reconstruction of sound speed and attenuation in ultrasound computed tomography using full wave inversion", *The Journal of the Acoustical Society of America*, vol. 141, no. 3, pp. 1595–1604, 2017.

[79] K. Wang, T. Matthews, F. Anis, C. Li, N. Duric, and M. A. Anastasio, "Waveform inversion with source encoding for breast sound speed reconstruction in ultrasound computed tomography", *IEEE Transactions on Ultrasonics, Ferroelectrics, and Frequency Control*, vol. 62, no. 3, pp. 475–493, 2015.

[80] P. Mojabi and J. LoVetri, "Ultrasound tomography for simultaneous reconstruction of acoustic density, attenuation, and compressibility profiles", *The Journal of the Acoustical Society of America*, vol. 137, no. 4, pp. 1813–1825, 2015.

[81] J. R. Berryhill, "Wave-equation datuming before stack", *Geophysics*, vol. 49, no. 11, pp. 2064–2066, 1984.

[82] S. Tegtmeier-Last, A. Gisolf, and D. Verschuur, "A data-mapping approach to 3-d wavefield redatuming", *Geophysical Journal International*, vol. 172, no. 2, pp. 759–769, 2008.

[83] G. Schuster and M. Zhou, “A theoretical overview of model-based and correlation-based redatuming methods: Geophysics, 71”, *SI103–SI110*, 2006.

[84] P. Haffinger, A. Gisolf, and P. M. Van Den Berg, “Towards high resolution quantitative subsurface models by full waveform inversion”, *Geophysical Journal International*, vol. 193, no. 2, pp. 788–797, 2013.

[85] Ö. Ozdemir and H. Haddar, “Preprocessing the reciprocity gap sampling method in buried-object imaging experiments”, *IEEE Geoscience and Remote Sensing Letters*, vol. 7, no. 4, pp. 756–760, 2010.

[86] S. A. Johnson, Y. Zhou, M. Tracy, M. J. Berggren, and F. Stenger, “Inverse scattering solutions by a sinc basis, multiple source, moment method—part iii: Fast algorithms”, *Ultrasonic Imaging*, vol. 6, no. 1, pp. 103–116, 1984.

[87] A. C. Ramírez and A. B. Weglein, “Green’s theorem as a comprehensive framework for data reconstruction, regularization, wavefield separation, seismic interferometry, and wavelet estimation: A tutorial”, *Geophysics*, vol. 74, no. 6, W35–W62, 2009.

[88] F. B. Jensen, W. A. Kuperman, M. B. Porter, and H. Schmidt, *Computational Ocean Acoustics*. Springer Science & Business Media, 2011.

[89] F. Simonetti, L. Huang, and N. Duric, “On the spatial sampling of wave fields with circular ring apertures”, *Journal of Applied Physiscs*, vol. 101, no. 8, pp. 083 103–083103–6, 2007.

[90] U. Taskin, N. Ozmen, H. Gemmeke, and K. W. A. van Dongen, “Modeling breast ultrasound; on the applicability of commonly made approximations”, *Archives of Acoustics*, vol. 43, no. 3, 2018, ISSN: 2300-262X.

[91] M. D. Verweij, B. E. Treeby, K. W. A. Dongen, and L. Demi, “Simulation of ultrasound fields”, in *Comprehensive Biomedical Physics*, A. Brahme, Ed., Oxford: Elsevier Science B.V., 2014, ch. 2.19, pp. 465–500.

[92] J. van der Neut and F. J. Herrmann, “Interferometric redatuming by sparse inversion”, *Geophysical Journal International*, vol. 192, no. 2, pp. 666–670, 2012.

[93] L. Heijnsdijk, E. Jansen, U. Taskin, H. den Bok, E. Bergsma, E. Noothout, N. de Jong, and K. W. A. van Dongen, “First steps towards the delft breast ultrasound scanning system (dbus)”, *Int. Workshop on Medical Ultrasound Tomography*, pp. 131–136, 2017.

[94] V. Schmitz, S. Chakhlov, and W. Müller, “Experiences with synthetic aperture focusing technique in the field”, *Ultrasonics*, vol. 38, no. 1-8, pp. 731–738, 2000.

[95] S.-Y. Huang, J. M. Boone, K. Yang, N. J. Packard, S. E. McKenney, N. D. Prionas, K. K. Lindfors, and M. J. Yaffe, “The characterization of breast anatomical metrics using dedicated breast ct”, *Medical Physics*, vol. 38, no. 4, pp. 2180–2191, 2011.

[96] N. K. Martiartu, C. Boehm, and A. Fichtner, “3-d wave-equation-based finite-frequency tomography for ultrasound computed tomography”, *IEEE Transactions on Ultrasonics, Ferroelectrics, and Frequency Control*, vol. 67, no. 7, pp. 1332–1343, 2020.

[97] R. J. Lavarello and M. L. Oelze, “Tomographic reconstruction of three-dimensional volumes using the distorted born iterative method”, *IEEE Transactions on Medical Imaging*, vol. 28, no. 10, pp. 1643–1653, 2009.

[98] X. Song, M. Li, F. Yang, S. Xu, and A. Abubakar, “Feasibility study of acoustic imaging for human thorax using an acoustic contrast source inversion algorithm”, *The Journal of the Acoustical Society of America*, vol. 144, no. 5, pp. 2782–2792, 2018.

[99] P. Mojabi and J. LoVetri, “Evaluation of balanced ultrasound breast imaging under three density profile assumptions”, *IEEE Transactions on Computational Imaging*, vol. 3, no. 4, pp. 864–875, 2017.

[100] K. W. A. van Dongen and W. M. D. Wright, “A full vectorial contrast source inversion scheme for three-dimensional acoustic imaging of both compressibility and density profiles”, *The Journal of the Acoustical Society of America*, vol. 121, no. 3, pp. 1538–1549, 2007.

[101] U. Taskin, J. van der Neut, H. Gemmeke, and K. W. A. van Dongen, “Redatuming of 2-d wave fields measured on an arbitrary-shaped closed aperture”, *IEEE Transactions on Ultrasonics, Ferroelectrics, and Frequency Control*, vol. 67, no. 1, pp. 173–179, 2019.

[102] A. T. de Hoop, “Handbook of radiation and scattering of waves: Acoustic waves in fluids, elastic waves in solids, electromagnetic waves: With corrections”, *Former publisher: Academic Press*, 2008.

[103] M. Abramowitz, “Abramowitz and stegun: Handbook of mathematical functions”, *US Department of Commerce*, vol. 10, 1972.

[104] K. W. A. van Dongen and W. M. D. Wright, “A forward model and conjugate gradient inversion technique for low-frequency ultrasonic imaging”, *The Journal of the Acoustical Society of America*, vol. 120, no. 4, pp. 2086–2095, 2006.

[105] A. Abubakar and P. M. Van Den Berg, “Total variation as a multiplicative constraint for solving inverse problems”, *IEEE Transactions on Image Processing*, vol. 10, no. 9, pp. 1384–1392, 2001.

[106] U. Taskin and K. W. A. van Dongen, “3-d redatuming for breast ultrasound”, in *Medical Imaging 2020: Physics of Medical Imaging*, International Society for Optics and Photonics, vol. 11312, 2020, 113125H.

[107] T. Hopp, M. Zapf, E. Kretzek, J. Henrich, A. Tukalo, H. Gemmeke, C. Kaiser, J. Knaudt, and N. V. Ruiter, “3d ultrasound computer tomography: Update from a clinical study”, in *Medical Imaging 2016: Ultrasonic Imaging and Tomography*, International Society for Optics and Photonics, vol. 9790, 2016, 97900A.

[108] C. Li, N. Duric, and L. Huang, “Clinical breast imaging using sound-speed reconstructions of ultrasound tomography data”, in *Medical Imaging 2008: Ultrasonic Imaging and Signal Processing*, International Society for Optics and Photonics, vol. 6920, 2008, p. 692 009.

[109] C. A. Balanis, *Advanced engineering electromagnetics*. John Wiley & Sons, 1999.

[110] R. L. Siegel, K. D. Miller, and A. Jemal, “Cancer statistics, 2019”, *CA: a cancer journal for clinicians*, vol. 69, no. 1, pp. 7–34, 2019.

[111] L. Sirgue and R. G. Pratt, "Efficient waveform inversion and imaging: A strategy for selecting temporal frequencies", *Geophysics*, vol. 69, no. 1, pp. 231–248, 2004.

[112] W. Mulder and R.-E. Plessix, "How to choose a subset of frequencies in frequency-domain finite-difference migration", *Geophysical Journal International*, vol. 158, no. 3, pp. 801–812, 2004.

[113] W. C. Chew and J. Lin, "A frequency-hopping approach for microwave imaging of large inhomogeneous bodies", *IEEE Microwave and Guided Wave Letters*, vol. 5, no. 12, pp. 439–441, 1995.

[114] A. Abubakar, P. M. van den Berg, and S. Y. Semenov, "A robust iterative method for born inversion", *IEEE Trans. Geosci. Remote Sens.*, vol. 42, no. 2, pp. 342–354, 2004.

[115] A. B. Ramirez and K. W. A. van Dongen, "Sparsity constrained born inversion for breast cancer detection", in *Ultrasonics Symposium (IUS), 2015 IEEE International*, IEEE, 2015, pp. 1–4.

[116] R. M. Souza, T. Q. Santos, D. P. Oliveira, R. M. Souza, A. V. Alvarenga, and R. P.B. d. Costa-Félix, "Standard operating procedure to prepare agar phantoms", in *J. Phys. Conf. Ser.*, vol. 733, 2016, p. 012 044.

[117] J. van der Neut, J. T. Fokkema, P. M. van den Berg, M. Zapf, N. V. Ruiter, U. Taskin, and K. W. van Dongen, "Ultrasonic synthetic-aperture interface imaging", *IEEE transactions on ultrasonics, ferroelectrics, and frequency control*, vol. 66, no. 5, pp. 888–897, 2019.

[118] J. van der Neut, P. M. van den Berg, J. T. Fokkema, and K. W. van Dongen, "Acoustic interface contrast imaging", *Inverse Problems*, vol. 34, no. 11, p. 115 006, 2018.

Acknowledgement

In this short life, PhD is a big journey. I had to use the word journey, it is classic but true. And this journey now ends with this thesis. These last pages are reserved for those who made this journey bearable and enjoyable. Since I am not good with words and long sentences, I will mention the names with a sentence but remember them with many memories.

- Nico, thanks for your out-of-the-box questions that helped me look at things from many different perspectives.
- Eric, thanks for your billions of useful ideas that let me improve my work.
- Koen, thanks for your excellent supervision, time, support, and many other things, but most importantly for making even the most challenging situations easier for me.
- Neslihan, thanks for your great thesis that was a great help at the beginning of my PhD to grasp the fundamentals quickly.
- Joost, thanks for the ideas and discussions that helped me shape part of this thesis and other discussions we had both scientific and non-scientific.
- People from KIT, Nicole, Hartmut, Michael, Torsten, thank you all for the discussions and time spent together during the conferences.
- Lars, Ernest, Robin, Thomas, thank you all for both hard-work that had some place in this thesis and kind friendship that made me adapt to Dutch culture easier.
- Angela, thanks for many many things, your great help in solving all kinds of silly problems from beginning to end, to your hospitality and friendship.
- Edo, thanks for solving all my software and server related problems quickly and also some nerd chats about IT.
- Henry, thanks for being there always and fixing all kinds of IT related problems and also chats about all kinds of trips.
- Ronald, thanks for your support for IT related problems and most importantly your infinite positive energy.
- Kees, thank you for the small chats during the mentorship hours that made me feel confident and relaxed.
- My officemates Apostolos, Aparajita, Dong, Fabian, Moein, Kefei, thanks to you all for the discussions about research and chatting almost about everything.

- My colleagues in the medical imaging group, Meysam, Elango, Albe, Jack, Boudewine, Verya, Agis, Djalma, Martijn, Chiara, Rick, thank you all for all the activities, chats, discussions, lunches, trips, accompany during conferences, and friendship.
- Sergio, thanks for your friendship at the very beginning of my PhD that made my life more fun.
- People in seismic, Aayush, Mikhail, Junhai, Lele, Leo, Ali, Hussain, thanks for the discussions about seismic and the ideas, and friendship.
- People in computational imaging, Boling, Sabri, Yan, Gyllion, Wenxiu, Qingru, thanks for all the good time spent together.
- Kerim, thank you for the friendship, reducing my homesickness with your gifts, chats, dinners, and many other things.
- İsmail, Münir, Erdinç, Cihan, Cem, thanks for the friendship and help that let me adapt to life here.
- Tahir, Resmigül, Güven and their families, thank you for your hospitality.
- The rest of the Chinese mafia, Tiexing, Xinmin, Qian, Hong, Bin, Jiao, Fei, Jin, Yun, Liyuan, thank you all for your friendship, discussions, and most importantly delicious food.
- People from Delft football group, Recep, Andreas, Rober Jan, Hysni, thank you all for the weekly football games and chats.
- Yaşam and Didem, thanks for the lifelong friendship.
- Seyhan, Berkin, Yusuf, Emre, Aptullah, thanks for your true friendship.
- Kemal, Önder, thanks for the feeling that we are always all together, everywhere.
- My family, father, mother, sister, you are the heroes of my life. Thanks for everything.
- Shan, the leader of the Chinese mafia, the conqueror of my heart, thank you for all the support, love, and many other things.

Ulas Taskin
Delft, the Netherlands
March, 2021

Curriculum Vitæ

Ulas Taskin

13-Sep-1989	Born in Elazig, Turkey.

Education

2017–2021	PhD candidate in Applied Physics Delft University of Technology, Delft, the Netherlands
2014–2016	MSc in Telecommunication Engineering Istanbul Technical University, Istanbul, Turkey
2007–2012	BSc in Telecommunication Engineering Istanbul Technical University, Istanbul, Turkey

Research experience

2017–2021	PhD candidate Delft University of Technology, Delft, The Netherlands Research on Full-waveform Inversion for Medical Ultrasound
2014–2016	Research assistant Istanbul Technical University, Istanbul, Turkey Research on Microwave Imaging

List of Publications

Journal Papers

1. **U. Taskin** and K. W. A. van Dongen, *Multi-parameter inversion with the aid of velocity field reconstruction*, The Journal of the Acoustic Society of America **147** (2020), pp. 4032–4040.

2. **U. Taskin**, J. van der Neut, H. Gemmeke, and K. W. A. van Dongen, *Redatuming of 2-D wavefields measured on an arbitrary-shaped closed aperture*, IEEE Transactions on Ultrasonics, Ferroelectrics and Frequency Control **67** (2020), pp. 173–179.

3. J. van der Neut, J. Fokkema, P. van den Berg, M. Zapf, N. Ruiter, **U. Taskin**, and K. W. A. van Dongen, *Ultrasonic synthetic-aperture interface imaging*, IEEE Transactions on Ultrasonics, Ferroelectrics, and Frequency Control **66** (2019), pp. 888-897.

4. **U. Taskin**, N. Ozmen, H. Gemmeke, and K. W. A. van Dongen, *Modeling breast ultrasound; on the applicability of commonly made approximations*, Archives of Acoustics **43** (2018), pp. 425–435.

5. **U. Taskin** and O. Ozdemir, *Sparsity regularized nonlinear inversion for microwave imaging*, IEEE Geoscience and Remote Sensing Letters **14** (2017), pp. 2220-2224.

Conference Papers

1. **U. Taskin** and K.W.A. van Dongen, *A Frequency-hopping technique for solving the cycle-skipping problem encountered with acoustic full-waveform inversion*, in International Ultrasonics Symposium (IUS) (IEEE, 2020).

2. **U. Taskin** K. Eikrem, G. Nævdal, M. Jakobsen, D. Vershuur, and K.W.A. van Dongen, *Ultrasound imaging of the brain using full waveform inversion*, in International Ultrasonics Symposium (IUS) (IEEE, 2020).

3. **U. Taskin** and K.W.A. van Dongen, *3-D redatuming for breast ultrasound*, in Medical Imaging 2020: Physics of Medical Imaging, 113125H (Proc. SPIE., 2020).

4. T. G. J. Bouchan **U. Taskin** and K.W.A. van Dongen, *Wavelet regularized Born inversion*, in International Ultrasonics Symposium (IUS) (IEEE, 2019).

5. E. Janssen **U. Taskin** and K.W.A. van Dongen, *Random frequency picking for waveform inversion*, in Proceedings of Meetings on Acoustics ICU (Acoustical Society of America, 2019).

6. **U. Taskin**, J. van der Neut and K.W.A. van Dongen, *Redatuming for breast ultrasound*, in International Ultrasonics Symposium (IUS) (IEEE, 2018).

7. **U. Taskin**, L. Heijnsdijk, L. Hoogerbrugge and K.W.A. van Dongen, *Using a 2-D approximation of the 3-D incident field for Born inversion*, in Proceedings of the International Workshop on Medical Ultrasound Tomography (KIT Scientific Publishing, 2017).

8. L. Heijnsdijk, E. Jansen, **U. Taskin**, H. den Bok, E. Bergsma, E. Noothout, N. de Jong and K.W.A. van Dongen, *First steps towards the Delft Breast Ultrasound Scanning System (DBUS)*, in Proceedings of the International Workshop on Medical Ultrasound Tomography (KIT Scientific Publishing, 2017).

9. E. Yalcin, O. Ozdemir and **U. Taskin**, *Sparsity based regularization for microwave imaging with NESTA algorithm*, in Conference on Antenna Measurements & Applications (CAMA) (IEEE, 2017).

10. **U. Taskin** and O. Ozdemir, *A sparsity based technique in wavelet domain for inverse source problem*, in Conference on Antenna Measurements & Applications (CAMA) (IEEE, 2016).

11. **U. Taskin**, E. Yalcin and O. Ozdemir, *Hard thresholding based compressed sensing approach for thermoacoustic tomography*, in URSI International Symposium on Electromagnetic Theory (EMTS) (IEEE, 2016).